Photoreception in ipRGCs and Their Developmental Roles in Neural Circuit Formation and Refinement

by
Kylie Shannon Chew

A dissertation submitted to Johns Hopkins University in conformity with the requirements for the degree of Doctor of Philosophy

Baltimore, Maryland
June, 2014

ABSTRACT

During development, neurons must form a precise network in order to generate a variety of complex behaviors. It is critical for many neurons to accurately achieve both local and long-distance connections. Retinal ganglion cells (RGCs) must both be integrated into the network of retinal neurons and form precise long-distance connections with a variety of different brain nuclei. Thus, these cells provide an excellent system to investigate the mechanisms underlying key processes of neural development.

My thesis work has focused on intrinsically photosensitive retinal ganglion cells (ipRGCs) because these cells are one of the few RGC subtypes that has highly specific molecular marker, which allows for the production of many genetic tools. Additionally, ipRGCs have defined projections that are distinct from other RGC subtypes, and ipRGCs have a well-established role in several testable behaviors, which provide a reliable output of their function. While ipRGC have a well-established role in mediating non-image light responses such as circadian photoentrainment, these cells are functional at early postnatal stages. Using genetic tools, labeling methods, and a variety of light cycles and conditions, I investigated how ipRGCs become integrated into retinal circuitry and whether they can influence the development of non-image or image forming visual systems. I found that ipRGCs undergo proximity-dependent Bax-mediated apoptosis to become evenly distributed across the retina and that disrupting this retinal mosaic impairs integration of ipRGCs into retinal circuitry. Additionally, I found ipRGCs are necessary during development to set the period of the circadian clock, a process that I further showed to be light-dependent. ipRGCs also have a light-independent developmental role in regulating the spatiotemporal properties of spontaneous activity in the retina, and without this

regulation, retinotopic circuitry in the brain abnormal, which in turn results in reduced visual acuity. Lastly, since ipRGCs have a critical light-dependent role in circadian regulation, I investigated the phototransduction cascade of ipRGCs, and revealed that it is more complicated than previously appreciated. My graduate work has extended our understanding of how ipRGCs develop and revealed their critical role in the development of both the circadian and image forming visual systems.

PREFACE

My graduate career has been an intense, exciting and often overwhelming experience. I never would have succeeded without the wonderful guidance and support of my teachers, friends, and family. I'd like to take the opportunity to thank them here.

I'll start at the beginning. I arrived at Mary Baldwin College with, of course, no idea what I wanted to do with my life. Drs. Lundy Pentz, Eric Jones, Paul Deeble, and Paul Callo were the entire biology faculty at Mary Baldwin, and if it weren't for them I never would have started exploring the field of biology. Dr. Lundy Pentz deserves an extra special thanks because his Developmental Biology is, to this day, the best class I've ever taken. It inspired me to make studying Development Biology my career. Furthermore, Dr. Pentz is an alum of the CMDB program at Johns Hopkins and his stories not only inspired to go to graduate school but to indeed pick the same program he did, a choice that I'm so lucky to have made. He is still, one of the smartest people, I've meet.

The CMDB faculty is just a fantastic group of people. They love what they do and the feeling is contagious. As a member of the JHU mouse-tri lab, I have benefited from having three PIs, each with their own remarkable set of traits. First, my direct PI: Dr. Samer Hattar: He has motivated me to become an independent, critically thinking scientist. His excitement and perseverance are infectious and especially helpful when you feel like you've hit a brick wall in your project. I feel our debates have made me, and maybe him ;), grow as scientist and a person. Dr. Rejji Kuruvilla's guidance and advice has always been welcome and sound. She has also served as thesis committee member,

iv

and I really appreciate her taking the time to do so. She has been a fantastic asset on my committee and she is an incredible scientist. I've never walked into Dr. Haiqing Zhao's office with a question and had him not have an answer. He is truly brilliant, his rigor as a scientist is inspiring, and he is a great mentor even when he doesn't need to be. He has been very involved with writing my main paper, and he deserves credit for teaching me anything I know about writing scientific papers.

Dr. Chen-Ming Fan has served on my thesis committee and I highly value all the advice he's given me on being a scientist. He is an incredible scientist and has a very thoughtful perspective on academia. His encouragement has benefited me immensely. Dr. Seth Blackshaw has also been on my thesis committee and his technical expertise has improved all the work I've done in grad school.

I also need to thank my fantastic lab-mates. The tri-lab is a great place work because the people in it. I want to thank both past and current members for all the technical support; they all have taught me so much. I especially want to thank my fellow Hattar lab member: David McNeill was my rotation mentor and my surrogate PI for the first 2 ½ years I was in the lab. He was great soundboard the all of my wacky ideas, and the imaging and figure making skills he taught me have been invaluable. Cara Altimus was a great lab mate, and an amazing friend; I will always treasure our conversations. Alan Rupp, Tiffany Schmidt, and Bill Keenan have been the best bay-mates, anyone could ask for. They are the reason I wanted to come to lab everyday. I will greatly miss brainstorming on new experiments and sharing the excitement of new data with them. I

truly would not have made it through graduate school with their technical and emotional support. They're the best.

I was incredibly lucky to have joined the CMDB program along with an awesome crew. My classmates bonded on our first day of grad school and they have become my fastest friends. I could always count on celebrating and commiserating every step of graduate school-life and real life with Kevin Lebo, his soon-to-be wife Diane Vig, and Vuong Tran. Stephanie Ketcham has been my best friend for the last six years; she has kept me sane. Our escapades have made my time in grad school some of the most fun I've ever had. Regardless of stresses from lab or real life, Steph has been there to help me through it all. I doubt she'll ever really appreciate how much she's done for me and how much I've relied on her. I've made many friends in grad school and I could write another thesis on why they are all so great. For the sake of space, I'll leave it at: you know who you are, and you are awesome!

David Martinelli is my wonderful boyfriend of 5 years. He is the love of my life, and I don't know what I would do without him; he is my rock and my partner-in-crime. He is such a thoughtful, caring, and dedicated person, and he always up for anything. Our adventures and travels are amazing, and I can't wait to see where our life together takes us next.

Rusty Warren, my God-mom (a.k.a. GoMo), has been a truly wonderful source of support for many years now. She has been my comrade for many adventures and I look forward

to more. I've never meet anyone else like GoMo; she is exactly who she wants to be and I greatly admire that. She is amazingly selfless and caring and her reminders of what is truly important in life have been critical in all of the major decisions I've made.

My Grandma has also been there for me throughout my life. She is <u>the</u> coolest grandma, I could imagine. She is my jet-setting, three-time national archery champion winning, belly-dancing grandma who for many years drove a bright yellow car with a racing stripe! It doesn't get any better than Grandma La Bamba ☺. She is an inspiration and I only hope I have as many awesome stories to tell my grandkids as she has told me.

I want to thank my parents for everything they've done for me. My Dad is my go-to person for advice. He has spent a great deal of his life observing people and current events as well as reading many history books, and his perspective on life is unique and refreshing. The knowledge he has accumulated is inspiring, and I love that he always makes me question my assumptions. My Mom is an amazing artist and as one, she can always give me a new take on a problem. I am always impressed by her creativity and I can't wait to see what fabulous art she'll make next. She was diagnosed with stage 4 breast cancer 2 ½ years ago, and she has handled the chemo, the radiation, and the surgeries like a warrior. Her drive is incredible and inspiring. My Dad has been a pillar of strength through out it all, and I still don't know how he does it, but I try to be like him. I'm in awe of them every day, and I want to dedicate this thesis and my graduate work to them.

TABLE OF CONTENTS

LIST OF TABLES

LIST OF FIGURES

CHAPTER 1: INTRODUCTION

INTRODUCTION

All multi-cellular organisms must accomplish the incredible feat of developing from a single cell into a being consisting of thousands, millions, or even billions of cells. Each of these cells has a specific identity and function allowing them to interact with other cells to accomplish complex behaviors such as intact of nutrients, movement, vision, and learning. The mechanisms that regulate and drive this intricate process have fascinated scientists for over a century. Neurons are particularly remarkable in what they must accomplish in order to precisely and effectively perform their adult function. Neurons, like other cells, must reach their correct location and establish interactions with nearby cells, but unlike other cells, they must also project processes, termed axons and dendrites, sometimes over great distances to establish connections with others cells even in other tissues. Subsequently these connections are then refined in both number and strength to produce the precise neural circuits necessary to drive complex behaviors.

The visual system is a classical model used to investigate this two-step developmental process of establishing gross neural connections and then refining those connections into precise circuits. In the visual system, the first step is a preset genetic program that involves gradients of attractive and repulsive axon guidance cues that direct axons to their final targets and establishes a coarse level of organization. In the visual system, these axons and their connections are pruned specifically in activity-dependent manner into the precise network necessary to maintain an accurate representation of the visual world. It is this process of refinement that has lead to concept that "neurons that fire together, wire together."

THE VISUAL SYSTEM AND LIGHT RECEPTION

The visual system can be divided into two broad categories of behavior: image and non-image forming functions. Image forming functions are those processes that contribute to what we think of as classic conscious vision, and includes color and contrast detection as well as depth perception and the tracking of moving objects. Non-image forming functions are subconscious behaviors that include the pupillary light reflex, the change in pupil diameter in response to changes in light intensity, and alignment of our daily rhythms of biochemical, physiological, and behavioral processes to our environmental light dark cycle, termed circadian photoentrainment. These two broad categories of behaviors are largely, and previously thought to be exclusively, distinct. They are mediated by distinct brain regions. Image forming functions are regulated by brain regions that include the dorsal lateral geneticulate nucleus (dLGN), the superior colliculus (SC), and the visual cortex. Non-image forming functions are regulated by brain regions that include the suprachiasmatic nucleus (SCN), which houses the master circadian pacemaker, and the olivary pretectal nucleus (OPN), which is important for the pupillary light reflex. More recent evidence has indicated that different photoreceptors detect light for image and non-image forming functions.

In mammals the only light sensing organ is the retina (Hattar et al., 2003), which is a multilayer organ in the back of the eye, and it is responsible for detecting light from our environment and relaying that information to the brain. The retina contains three major cell layers: the outer nuclear layer, inner nuclear layer, and ganglion cells layer (Wässle, 2004). The outer nuclear layer contains the cell bodies of the classic vertebrate photoreceptors, rods and cones, which are responsible for the detection of photons at low and high light intensities. In addition, cones are required for color vision. The inner nuclear layer contains horizontal, bipolar, and amacrine cells, which relay the light information that originated in rod and cones and begin

to process this information to allow for the detection of contrast and directional movement. The ganglion cell layer contains retinal ganglion cells (RGCs), which are the only output neurons of the retina, and these cells are responsible for receiving the relayed and, in some cases, processed light information from bipolar and amacrine cells and transmitting that information onto brain regions such as the dLGN and SC (Wässle, 2004). This pathway has been established to be the route that light information takes to initiate the construction of a conscious visual image of our environment.

INTRINSICALLY PHOTOSENSITIVE RETINAL GANGLION CELLS

Until recently, rods and cones were considered the only photoreceptive cells in the retina. However, studies found that animals lacking rods and cones due to retinal degeneration retained the ability to align their biological rhythms to a light/dark cycle (Foster et al., 1991; Freedman et al., 1999). In contrast, mice in which the eyes had been removed were unable to do this (Foster and Hankins, 2002). Additionally some blind humans who were unable to consciously perceive light and images remained capable of detecting light, subconsciously for circadian photoentrainment (Czeisler et al., 1995; Klerman et al., 2002; Zaidi et al., 2007). Together, these studies pointed to the existence of a non-rod/non-cone photoreceptor important for mediating non-image responses to light. Ignacio Provencio and colleagues provided the first evidence as the identity of this elusive photoreceptor when they detected expression of the photopigment melanopsin in 2-3% of the RGCs (Provencio et al., 1998; Provencio et al., 2000). Soon after, it was determined that the presence of melanopsin expression in these RGCs renders them capable of detecting light directly, thus making them intrinsically photosensitive retinal ganglion cells (ipRGCs) (Berson et al., 2002; Hattar et al., 2002; Lucas et al., 2003; Panda et al., 2002). Thus

this population of RGCs can act both as a photoreceptor, responding to light to directly, and as a conventional ganglion cell, relaying light information originating in rods and cones. Interestingly, when ipRGC cell bodies and axons were specifically labeled by knocking tau-LacZ into the melanopsin locus ($Opn4^{tau-LacZ/+}$), it was determined that ipRGCs project specifically to regions of the brain involved with non-image forming functions such as the SCN and the OPN (Hattar et al., 2006; Hattar et al., 2002)

Removal of the melanopsin protein from these cells ($Opn4^{tau-LacZ/tau-LacZ}$) resulted in the loss of intrinsic photosensitivity. This resulted in several specific; although minor, deficits in the pupillary light reflex and some aspects of circadian behaviors and there was no affect on image forming functions (Lucas et al., 2003; Mrosovsky and Hattar, 2003; Panda et al., 2002). Surprisingly, the molecular cascade responsible for converting photon detection by melanopsin into to transmittable electrical signal (the phototransduction cascade) has not been fully investigated, and no other tested mutant line phenocopies the melanopsin knockout line.

Removal of rod and cone signaling, leaving ipRGCs as the only functional photoreceptor, revealed that these cells are sufficient to signal light to drive non-image forming functions (Ecker et al., 2010; Freedman et al., 1999; Hattar et al., 2003). Next, ipRGCs were genetically ablated in mice though the expression of diphtheria toxin (aDTA) from the melanopsin locus ($Opn4^{aDTA/aDTA}$ mice;(Güler et al., 2008)). In the $Opn4^{aDTA/aDTA}$ mice, conventional RGCs were not affected, and image-forming vision was unaffected in these animals. However, retinal projections to non-image forming centers were abolished and $Opn4^{aDTA/aDTA}$ mice, while able to maintain circadian rhythmicity, were not capable of circadian photoentrainment (Güler et al., 2008). It is important to note that due the use of an attenuated toxin and the relatively weak melanopsin promoter, in $Opn4^{aDTA/aDTA}$ mice, ipRGC ablation is progressive throughout

adulthood and only results in a loss of photoentrainment at about 6 months of age. Nonetheless, these data indicated that ipRGCs are the sole conduit for light information, whether it is detected in rods and cones or in ipRGCs themselves, to non-image forming centers in the brain.

Intriguingly, mice with ipRGCs as the only functional photoreceptor were not only fully capable of non-image forming functions but they also exhibited rudimentary image forming vision implicating a role for ipRGCs in image formation providing the first evidence for crosstalk between the image and non-image forming aspects of the visual system (Ecker et al., 2010). More recently ipRGCs have even been implicated in regulating contrast sensitivity (Schmidt et al. Submitted). Thus far, ipRGCs had been implicated in all aspects of circadian based light-dependent behaviors, the pupillary light reflex, and even some aspects of image forming vision (Ecker et al., 2010; Güler et al., 2008; Schmidt et al., 2011). Interestingly, several research groups had noticed that careful labeling of ipRGCs with a sensitive melanopsin antibody revealed that the $Opn4^{tauLacZ}$ reporter allele did not label all ipRGCs (Baver et al., 2008). Unlike the tauLacZ labeled ipRGCs, whose dendrites arborize in the OFF sublamina of the inner plexiform layer of the retina, this newly discovered type of ipRGCs had dendrites which arborized in the ON sublamina of the inner plexiform layer. These two different subtypes quickly became known as M1 and M2, with the M1 being the familiar OFF arborizing tauLacZ labeled ipRGCs and the M2 being the newly discovered ON arborizing ipRGCs. Retrograde labeling from the OPN revealed that the core of the OPN is primarily innervated by the M2 ipRGCs (Baver et al., 2008), while previous data from the $Opn4^{tauLacZ}$ mice had already shown that the M1 ipRGCs innervated a shell around the edge of the OPN (Hattar et al., 2006). Thus, it was interesting to propose that this different ipRGC subtypes could contribute to different behaviors.

However, thus far ipRGCs had only been shown to almost exclusively project to non-

image forming regions of the brain. How then, could animals with ipRGCs as the only functional photoreceptor still have residual pattern vision? Since, the signal strength of the $Opn4^{tauLacZ}$ reporter is directly tied to the expression level of the melanopsin gene. The cre-loxP system provided a relatively simple method to determine where there were any additional ipRGC subtypes. Specifically, the melanopsin coding sequence was replaced with the coding sequence for the cre recombinase to generate an $Opn4^{Cre}$ mouse line (Ecker et al., 2010). Cre expression, specifically in ipRGCs, could then be used to turn on expression of a reporter driven by a strong promoter, such as the Z/AP reporter, which labels the cell membrane, including axons and dendrites with alkaline phosphatase (Lobe et al., 1999). This method revealed that 5 distinct morphological subtypes of ipRGCs exist and that the five subtypes project to different brain regions(Ecker et al., 2010; Schmidt et al., 2011; Schmidt and Kofuji, 2009). M1 ipRGCs project to the SCN and the shell of the OPN, M2 ipRGCs project to the core of the OPN (and a little to the dLGN), and M4-M5 ipRGCs project to both the dLGN and SC (M3 ipRGCs remain relatively uncharacterized). These data lead to the hypothesis that the M4 and M5 (and maybe M2s) contribute to image-forming vision, while the M1 population specifically drives non-image forming behaviors.

Further investigation into ipRGC subtypes determined that the M1 subtype could be further subdivided based on whether or not the transcription factor Brn3b (Pou4f2) is expressed (Chen et al., 2011; Jain et al., 2012). Among M1 ipRGCs, about 200 cells do not express Brn3b. These Brn3b-negative M1 ipRGCs project only to circadian centers (predominantly to the SCN) and are sufficient for circadian photoentrainment (Chen et al., 2011). The other M1 ipRGCs as well as all non-M1 ipRGCs express Brn3b and can be selectively ablated by crossing $Opn4^{Cre/+}$ mice with $Brn3b^{Z-DTA/+}$ mice, in which a floxed stop cassette followed by DTA has been inserted

into the *Brn3b* locus (Mu et al., 2005). In *Opn4$^{Cre/+}$;Brn3b$^{Z-DTA/+}$* offspring, DTA is expressed only in cells in which both the *Brn3b* and *Opn4* promoters are active; thus, Brn3b-positive ipRGCs are killed, while Brn3b-negative ipRGCs and all conventional RGCs are spared (Chen et al., 2011). *Opn4$^{Cre/+}$;Brn3b$^{Z-DTA/+}$* mice can photoentrain normally, but have severe deficits in the pupillary light reflex. Indicating that that Brn3b negative M1 ipRGCs are sufficient for circadian photoentrainment, while Brn3b positive M1 ipRGCs (and possibly M2 ipRGCs) are required for the pupillary light reflex.

DEVELOPMENT OF THE VISUAL SYSTEM

The visual system has been a classic model to examine neural development for decades. For the visual system to be effective, the brain must be able to create an accurate image of our environment. RGCs that are next to each other in the retina will receive light information originating from adjacent portions of the visual field. Thus, in order to form a comprehensive image of the visual world, light information and the relative locations of the RGCs that carry that light information, must conveyed to the brain. To accomplish this, the projection pattern of RGC axons echoes the relative position of their cell bodies in the retina creating a retinotopic map. Retinotopic map formation was used by Roger Sperry to confirm the chemoaffinity hypothesis (Sperry, 1943), which predicted that neurons make connections with their targets based on interactions with specific molecules and, therefore, the neural circuits of an organism are determined by its genotype. Since Sperry's work, the molecules that globally direct RGCs to their targets in the brain, Ephrins, have been identified (Cheng et al., 1995; Drescher et al., 1995; Triplett and Feldheim, 2012). Later work from Shatz and colleagues determined that retinotopic map formation is not exclusively dependent on an intrinsic genetic program, and that

spontaneously derived activity, termed a retinal wave, propagates across the retina is responsible for postnatal refinement of RGCs circuitry in the brain (Ackman et al., 2012; Chandrasekaran et al., 2005; Feller, 2002, 2009; Firth et al., 2005; McLaughlin et al., 2003b; Mrsic-Flogel et al., 2005; Muir-Robinson et al., 2002; Shah and Crair, 2008; Stellwagen and Shatz, 2002; Wong, 1999; Zhang et al., 2011). It has further been shown that spatiotemporal properties of these retinal waves are particularly important to instruct map formation (Xu et al., 2011). It has yet to be determined how retinal waves are initiated and how the dynamics of retinal waves are regulated. Additionally, the molecular mechanisms underlying how activity instructs nearby RGCs to wire with nearby neurons in the brain remain unknown.

There are many distinct subtypes of RGCs, which have precise functions. For example, some RGCs detect changes in contrast and others detect directional movement (Coombs et al., 2006). This system provides a model to examine how a diverse population of cells is specified and organized during development to produce to a cohesive system in the adult animal. Many questions still remain in this field, such as, how are these ganglion cell subtypes specified from common precursor cells? how are these diverse cell population distributed equally across the retina? And how do individual RGC subtypes form the correct connections with their targets in the brain to effectively contribute specific properties of the visual scene, such as contrast, to the comprehensive image of our environment? ipRGCs provide an excellent model to investigate these questions because they are one of the few RGC subtypes that has specific molecular marker (melanopsin), which allows for the production of many genetic tools. ipRGCs have defined projections that are distinct from other RGCs, and ipRGCs are know to be required for several testable behaviors, which provide a reliable output of their function.

My graduate thesis work has focused on addressing the following questions:

How do M1 ipRGCs establish their location in retina during development and what is the function of a retinal mosaic in cell population that does not require a retinotopic map for its function? This work resulted in the following major conclusions:

1- ipRGCs undergo proximity-dependent Bax-mediated apoptosis to produce a retinal mosaic

2- Disrupting the retinal mosaic of ipRGCs does not affect melanopsin-based circadian photoentrainment, but impairs retinal circuitry required for light information from rod/cones to reach ipRGCs and drive photoentrainment

Do ipRGCs, which are the first functional photoreceptors, have a developmental role in the visual system? This portion of my thesis work resulted in the following major conclusions:

1- Light is necessary for the proper development of the circadian clock in mammals and can set the circadian period even during adulthood. However, exposure to light irreversibly sets the intrinsic circadian period.

2- ipRGCs are necessary for the setting of the circadian period by light.

3- Animals that lack ipRGCs during early postnatal stages display altered retinal waves, disrupted eye-specific axonal segregation in the lateral geniculate nucleus, and reduced visual acuity.

4- 200 M1 ipRGCs are sufficient to both set the period of circadian clock and promote proper formation of visual circuitry and function.

What is the molecular pathway for photoreception in ipRGCs? This portion of my thesis work resulted in the following major conclusion:

1- None of the four Gq proteins in mice are necessary, alone or in combination, for melanopsin-based phototransduction, and suggest that ipRGCs may be able to utilize a $G_{q/11}$-independent phototransduction cascade *in vivo*.

CHAPTER 2: APOPTOSIS REGULATES IPRGC SPACING NECESSARY FOR RODS AND CONES TO DRIVE CIRCADIAN PHOTOENTRAINMENT

Chen S.K.*, Chew K.S.*, McNeill D.S.*, Keeley P.W., Ecker J.L., Mao B.Q., Pahlberg J., Kim B., Lee S.C., Fox M.A., Guido W., Wong K.Y., Sampath A.P., Reese B.E., Kuruvilla R., Hattar S.
* denotes equal contribution

INTRODUCTION

The retina detects and processes light information such as intensity, contrast, color, and motion before conveying it to the brain. To precisely convey the spatial mapping of these visual qualities, many different types of neurons form regularly spaced arrays across the surface of the retina (Cook and Chalupa, 2000). Yet how each type of neuron forms such an ordered distribution, which occurs during development, is an area of emerging interest (Reese, 2008). In the vertebrate retina, it has been shown that mosaics form through different developmental processes including periodic fate assignment, tangential dispersion, or apoptosis (Galli-Resta, 2002). Similar to other neuronal populations, more than half of the retinal ganglion cells (RGCs) are eliminated during development by apoptosis (Farah and Easter, 2005; Mosinger Ogilvie et al., 1998; Perry et al., 1983). Deletion of Bax, a pro-apoptotic factor, prevents this loss of RGCs (Mosinger Ogilvie et al., 1998). Although apoptosis mediated through Bcl-2 family members including Bax contributes to the spatial distribution of some retinal cell types (Keeley et al., 2012; Raven et al., 2003), there has been no direct demonstration of any functional consequences associated with such disrupted cell spacing, specifically, upon retinal circuitry and behavior.

Similar to other retinal cell types, the subtypes of intrinsically photosensitive RGCs (ipRGCs) form independent mosaics across the retina (Ecker et al., 2010).We have previously developed several genetically modified mouse models that allow us to specifically label ipRGCs as well as quantitative behavioral assays that permit an assessment of their functional output (Ecker et al., 2010; Güler et al., 2008; Hattar et al., 2002). Using a variety of spatial statistics to ascertain the regularity and intercellular spacing of such mosaics, in conjunction with the above

anatomical and functional tools, we have examined the role of apoptosis in generating a cell type specific mosaic and its behavioral significance.

ipRGCs are the sole conduit for light information to influence several distinct behavioral outputs. Their axons target the suprachiasmatic nucleus (SCN) for photoentrainment of circadian rhythms and the olivary pretectal nucleus (OPN) for pupillary light responses (PLR) (Güler et al., 2008; Hattar et al., 2006; Hattar et al., 2002). Unlike other types of RGCs, the ipRGCs combine their intrinsic melanopsin-based photosensitivity with extrinsic input from rods and cones (Mrosovsky and Hattar, 2003). Either the extrinsic rod-cone signal or the intrinsic melanopsin-based signal is sufficient to drive both photoentrainment and PLR (Freedman et al., 1999; Hattar et al., 2003; Lucas et al., 2001; Lucas et al., 2003; Panda et al., 2002; Ruby et al., 2002). Thus, in melanopsin knockout animals, the rod-cone input to ipRGCs can be assessed at the behavioral level independent of the intrinsic light response. Here, we determined the role of apoptosis in generating the spatial distribution, connectivity and functional output of ipRGCs using *Bax* mutant mice. We show that Bax-mediated apoptosis, in both germline and ipRGC-specific *Bax* mutant mice, is required to establish a spaced mosaic of ipRGCs during development. Disruption of the spaced distribution of ipRGCs does not impair functional responses driven by the intrinsic photosensitivity of ipRGCs in *Bax* mutant mice. However, rod/cone signaling through ipRGCs to drive circadian photoentrainment is severely attenuated, consistent with anatomical and physiological evidence for disrupted rod-cone activation of ipRGCs. Thus, for irradiance detection, developmental apoptosis is necessary for the spacing and connectivity of ipRGCs that underlie their functioning as a component of a neural network without affecting their role as intrinsic light sensors.

RESULTS

Bax-dependent apoptosis mediates formation of the ipRGC mosaic

Melanopsin immunofluorescence on wholemount retinas from adult wild type and *Bax* knockout (*Bax*$^{-/-}$) mice reveals that ipRGCs in *Bax*$^{-/-}$ mice form clumps with highly fasciculated dendrites (Figure 1A and B; Table 1), similar to the clustering recently described in the Dscam-mutant retina (Fuerst et al., 2009; Keeley et al., 2012). The clustering observed in the *Bax*$^{-/-}$ mice is not informative about single type of retinal neuron, since recent evidence demonstrates that ipRGCs comprise multiple subtypes (Baver et al., 2008; Ecker et al., 2010; Provencio et al., 2002; Schmidt and Kofuji, 2009; Viney et al., 2007), of which, several form individual mosaics (Berson et al., 2010). To better study ipRGC mosaic formation, we analyzed one single subtype, the M1 ipRGCs, which are labeled by X-gal staining in the *Opn4*^{tauLacZ} reporter mice (Figure 1C; Table 1) (Baver et al., 2008; Hattar et al., 2002). In *Bax*$^{-/-}$ mice, we found a 3.7-fold higher average density of ipRGCs than in the controls (Figure 1D). No changes in total retinal area were observed between *Bax*$^{-/-}$ and wild type animals (data not shown). This increase in ipRGC density indicates that similar to other RGCs, ipRGCs also undergo Bax-mediated apoptosis during development (Mosinger Ogilvie et al., 1998; White et al., 1998). To determine the developmental stage at which ipRGCs undergo apoptosis, we used the *Opn4*$^{Cre/+}$ animals in conjunction with the *Z/AP* reporter allele (Ecker et al., 2010; Lobe et al., 1999), to permanently label all ipRGC subtypes with alkaline phosphatase (AP) (Table 1). In the *Opn4*$^{Cre/+}$; *Z/AP* animals, any decrease in the numbers of AP labeled cells during development should be due to apoptosis. We found a significant depletion of ipRGCs between P3 and P9 (Figure 2), which is in agreement with both

Table 1: Mouse lines used in Chapter 2

Mouse Lines	ipRGC Phenotype	Circadian photoentrainment
$Opn4^{tau-LacZ/+}$	Only M1 ipRGCs labeled; normal ipRGC development and target innervation	Normal circadian photoentrainment
$Opn4^{tau-LacZ/tau-LacZ}$, also $Opn4^{-/-}$ (MKO)	Only M1 ipRGCs labeled; normal ipRGC development and target innervation; Melanopsin knockout	Normal circadian photoentrainment; phase shifts and period lengthening deficits
$Opn4^{Cre/+}$	Expresses Cre recombinase under the melanopsin promoter	Normal circadian photoentrainment
$Opn4^{Cre/+}$; Z/AP and $Opn4^{Cre/+}$; Z/EG animals	All ipRGCs labeled with alkaline phosphatase or green fluorescent protein, respectively.	Normal circadian photoentrainment
$Bax^{-/-}$ (Bax KO)	Disrupted cell spacing; excess number of ipRGCs; fasciculated dendrites	Wild-type-like circadian photoentrainment
$Bax^{-/-}$; $Opn4^{tau-LacZ/+}$	Disrupted cell spacing; excess number of ipRGCs; fasciculated dendrites; only M1 labeled	Wild-type-like circadian photoentrainment
$Bax^{-/-}$; $Opn4^{Cre/tau-LacZ}$, also $Bax^{-/-}$; $Opn4^{-/-}$ (DKO)	See above (*Bax* KO)	Major deficits in photoentrainment
$Opn4^{Cre/+}$; $Bax^{fl/fl}$ or $Opn4^{Cre/+}$; $Bax^{fl/-}$ (*Bax* cKO)	Disrupted cell spacing; normal cell numbers; no fasciculated dendrites.	Wild-type-like circadian photoentrainment
$Opn4^{Cre/tau-LacZ}$; $Bax^{fl/fl}$ or $Opn4^{Cre/tau-LacZ}$; $Bax^{fl/-}$ (cDKO)	See above (cKO); only M1 ipRGCs labeled	Major deficits in photoentrainment in most animals
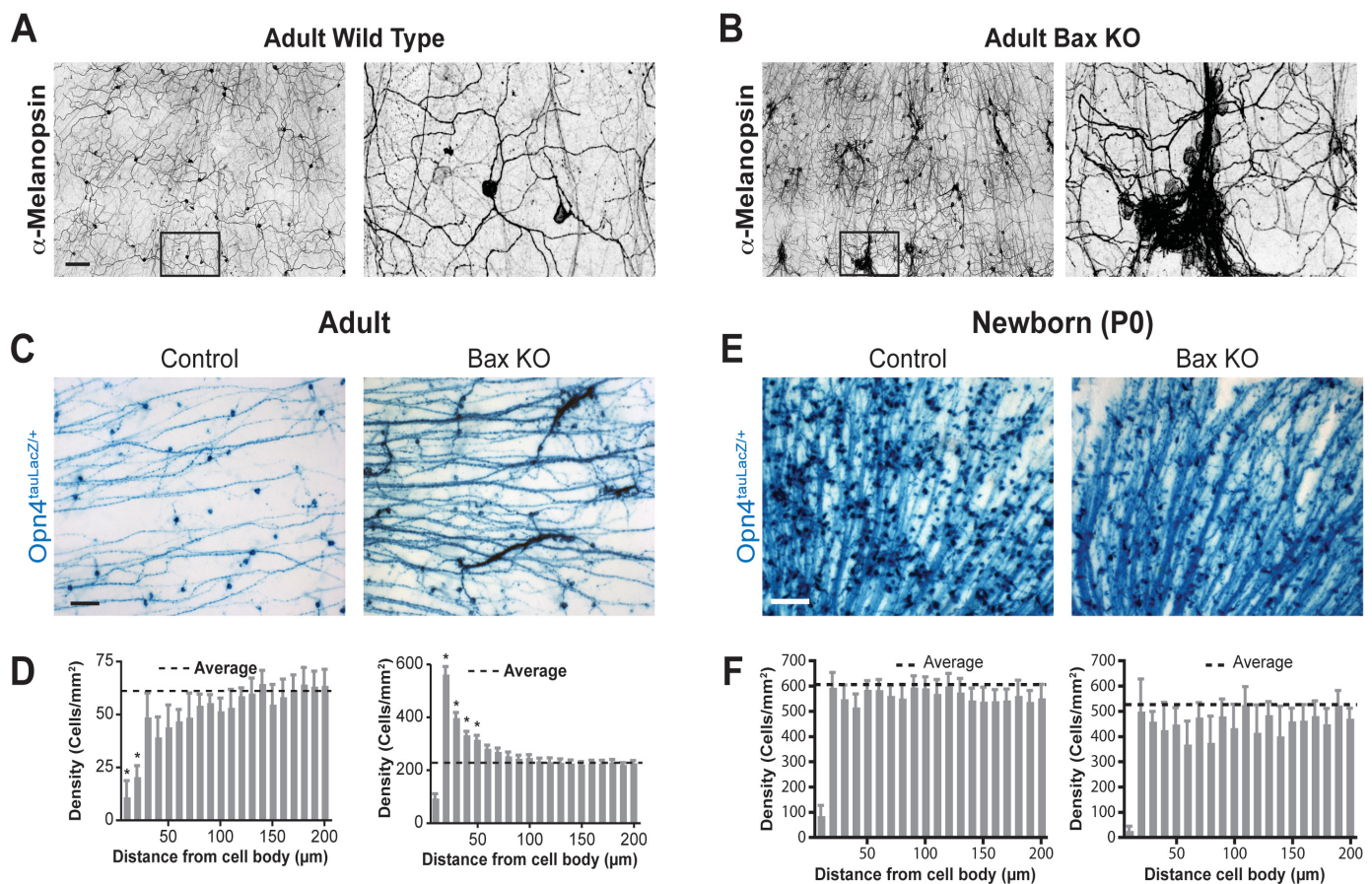
Figure 1. Bax is required for correct spacing of ipRGCs

Melanopsin immunofluorescence on wholemount retinas from adult mice (A and B). In control wild type mice (A), the ipRGC dendrites form a receptive net across the retina. The Bax knockout (Bax KO) contains clusters of ipRGCs (B) with fasciculated dendrites. (C) X-gal staining of M1 ipRGCs, which preferentially labels somata and axons, in whole-mount retinas from control and Bax KO adult mice. (D) Density recovery profiles derived from the autocorrelation from images such as those in (C) show that ipRGCs form a spaced distribution in the control (lower than average density in bins closer to the origin) and a clustered distribution in the Bax KO (higher than average density in bins closer to the origin)(n=6 retinas for each group). Note that the closest bin is always lower than average since the cell body size prevents most cells from being closer than 10 μm to each other. (E) X-gal staining of M1 ipRGCs in whole-mount retinas from control (Bax+/-) and Bax KO littermate mice at P0. (F) Density recovery profiles for ipRGCs from control and Bax KO mice at P0 shows a random distribution of ipRGCs at this time for both groups (average density in all bins except the closest) (n=5 retinas for each group). Data are mean±SEM; scale bars are 100μm; * indicates significance from the average density by one-way ANOVA with Tukey post hoc, p<0.05, mean±SEM.
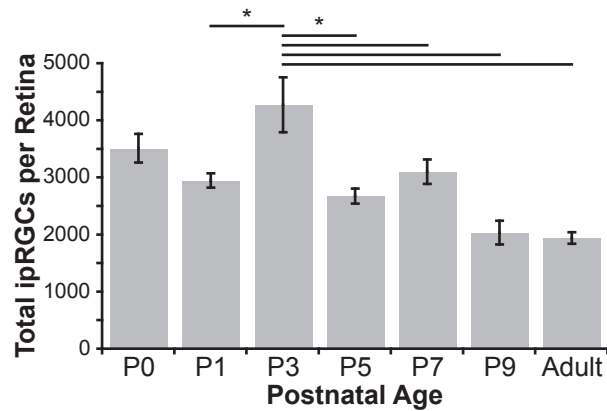
Figure 2. Time course for cell death in ipRGCs during postnatal development
The Opn4Cre/+; Z/AP mice allow us to permanently label ipRGCs and therefore any decline in the number of ipRGCs is attributed to cell death. Total ipRGC numbers in the retina of Opn4Cre/+; Z/AP mice during postnatal development were counted. The peak increase in ipRGC numbers is observed at P3 and ipRGC numbers drop to adult levels by P9 (* indicates $p < 0.05$ with a one-way ANOVA with Tukey post hoc, n=5 retinas per time point, Mean±SEM).

the timing and the magnitude of developmental apoptosis for the conventional RGCs (Dreher et al., 1983; Perry et al., 1983).

To objectively demonstrate the clumping phenotype observed in M1 ipRGCs of *Bax* mutants (Figure 1C), we performed autocorrelation analysis in control mice and showed that M1 ipRGCs form a spaced distribution across the retina by forming an average exclusion zone of ~ 40mm around each ipRGC soma (Figure 1D, left panel), a defining trait of retinal mosaics (Cook and Noden, 1998). In contrast, in *Bax* mutant mice, we noted that M1 ipRGC somata failed to exhibit normal exclusion zones and instead showed a clustering of ipRGC cell bodies, confirming the disruption in cell spacing for a single class of ipRGC (Figure 1D, right panel). Consistent with a role for cell death in the spacing of ipRGCs, at P0, a time point preceding cell death, control and *Bax*$^{-/-}$ mice have similar average densities of M1 ipRGCs and both show a random distribution of them (i.e. one that is neither spaced nor clustered) (Figure 1E and F). These results indicate that ipRGCs are first generated in a random distribution, and then progress to either a spaced distribution in the wild type or a clumped distribution in *Bax*$^{-/-}$ mice.

These results suggest a model by which proximity between neighboring cells promotes apoptosis (Figure 3A), and loss of Bax abrogates this proximity-based effect. To test this model, we determined the spatial relationship between dying cells and their immediate neighbors. Since apoptotic cells are believed to be present for only ~ 1 hour (Cellerino et al., 2000), we combined three different labels for apoptotic cells (TUNEL and two antibodies specific for activated caspase-3 and activated Bax) to increase our chances of finding ipRGCs that were undergoing apoptosis. The latter were detected by using the *Z/EG* reporter line (Novak et al., 2000) to fluorescently label ipRGCs (Table 1). ipRGCs comprise 2% of RGCs, and we found only 77 ipRGCs undergoing apoptosis in eight retinas (Figure 3B). For each of those cells, we performed
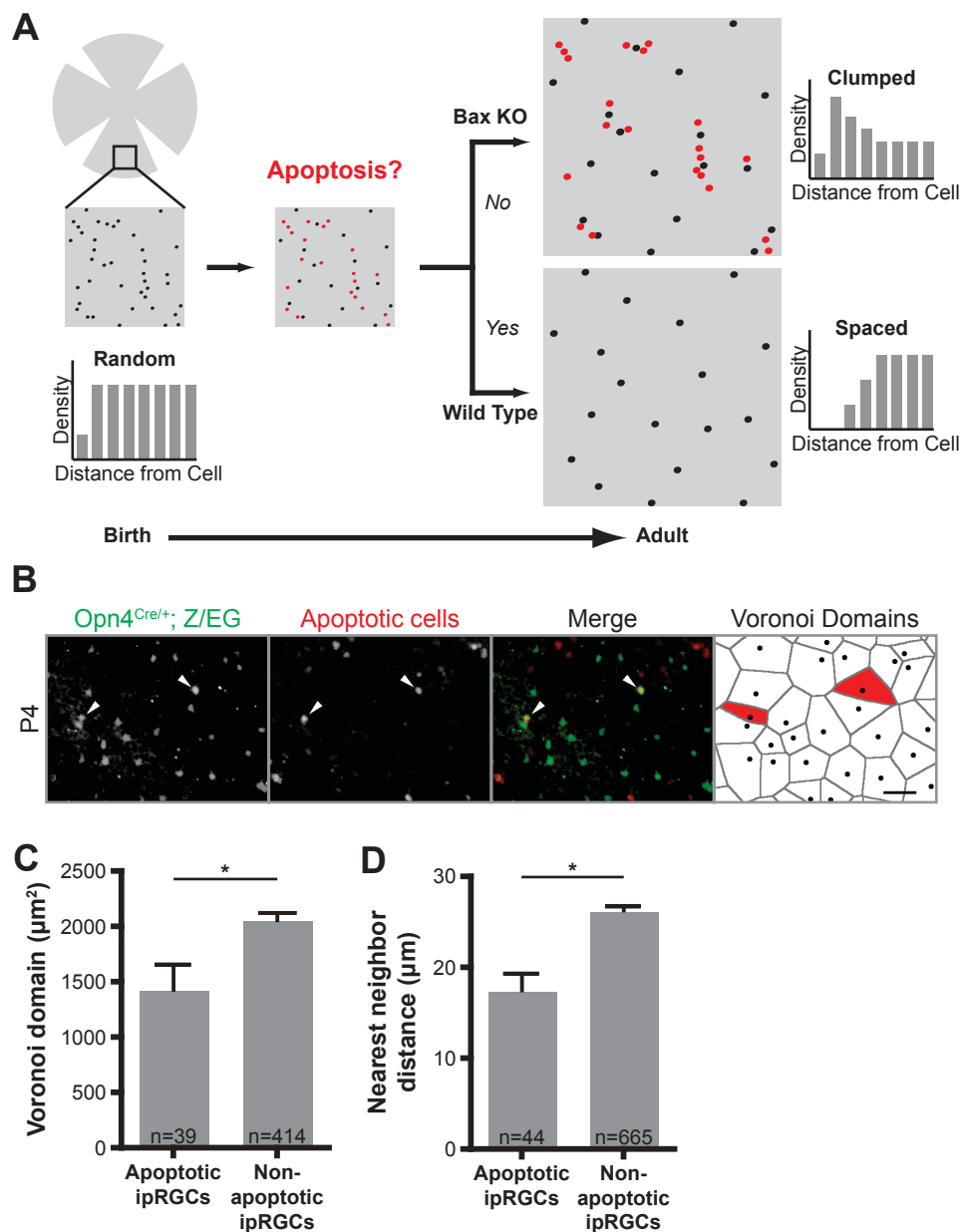
Figure 3. Proximity-based apoptosis leads to proper ipRGC spacing

(A) Model showing how proximity-based apoptosis may generate a mosaic for a specific cell type. Only cell positioning, not fasciculation, is shown, for clarity. Cells in close proximity to each other (shown in red) are eliminated by Bax-mediated apoptosis to form a more spaced distribution in the adult. In Bax KO mice, cells in close proximity to each other survive. (B) Total ipRGCs were labeled in green at P4 with an anti-GFP antibody in Opn4Cre/+; Z/EG mice. Cells undergoing apoptosis were stained red by TUNEL and two antibodies specific for activated caspase-3 and activated Bax. Apoptotic ipRGCs (positive for any of these three indicators of cell death) are indicated with arrowheads (scale bar 50µm). The last panel shows Voronoi domains (VD) for each ipRGC in the field, with the VD for the dying ipRGCs labeled in red. (C) The subset of ipRGCs undergoing apoptosis at P4 have significantly smaller Voronoi domains than non-apoptotic ipRGCs ($1429 \pm 230.5 \mu m2$, n=39 for apoptotic; 2059 ± 66.95, n=414 for non-apoptotic, from eight retinas; p=0.0062 by Student t-test, mean±SEM). (D) The apoptotic ipRGCs had a significantly smaller nearest neighbor distance to adjacent ipRGCs than non-apoptotic ones ($17.49 \pm 1.848 \mu m$, n=44 for apoptotic; $26.28 \pm 0.4741 \mu m$, n=665 for non-apoptotic, from eight retinas; p<0.0001 by Student t-test, mean±SEM).

Voronoi domain (VD) analysis (Figure 3B right panel) followed by nearest neighbor measurements. The Voronoi domain of a cell defines the area surrounding the cell containing all points closer to that cell than to any other cell. The closest of those Voronoi neighbors is the nearest neighbor. We found that apoptotic ipRGCs had significantly smaller Voronoi domains and shorter nearest neighbor distances than viable ipRGCs (Figure 3C and D). These results suggest that ipRGCs that are in close proximity preferentially undergo apoptosis. Proximity-based apoptosis may thereby generate exclusion zones that transform the distribution of ipRGCs from random into spaced (Figure 3A).

Bax is crucial for ipRGC connection to upstream retinal circuitry

We next sought to determine if the clumped ipRGC distribution in the *Bax* mutants affect the ability of ipRGCs to mediate non-image forming functions (Figure 4A). We first wanted to ensure whether ipRGC axons exhibit normal innervation of their brain targets in the *Bax* mutants. To assess M1 ipRGC axonal targeting, we used X-gal staining in coronal brain sections from *Bax*$^{-/-}$ mice also harboring the *Opn4*$^{tau-LacZ}$ reporter allele (*Opn4*$^{tau-LacZ/+}$*; Bax*$^{-/-}$; Table 1) (Hattar et al., 2002). *Opn4*$^{tau-LacZ/+}$ animals were used as controls. Despite altered M1 ipRGC spacing and fasciculated dendritic morphology in *Bax* mutant animals, we observed normal axonal targeting in the major retinorecipient brain regions of M1 ipRGCs, such as the suprachiasmatic nucleus (SCN) and intergeniculate leaflet (IGL), responsible for circadian rhythms, and the shell of the olivary pretectal nucleus, a relay center for the pupillary light reflex (Figure 4B). Although we observed denser innervation in *Bax* mutant animals, likely due to increased ipRGC numbers, we did not observe any navigational errors or ectopic ipRGC innervation in central brain targets (Figure 4B and Figure 5).
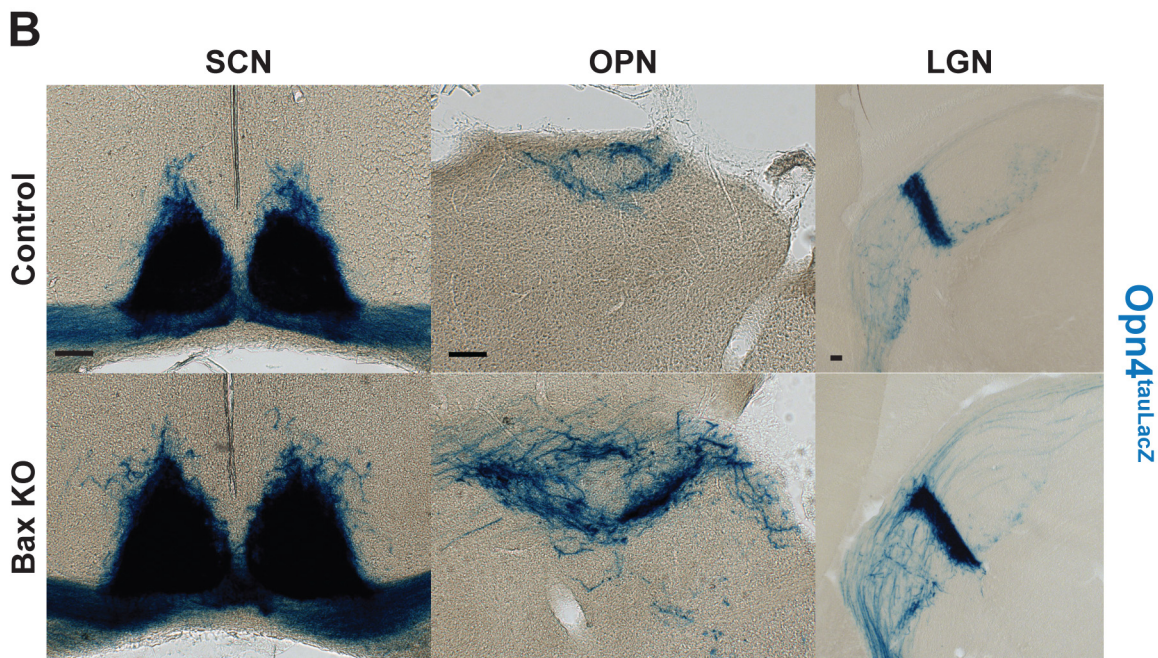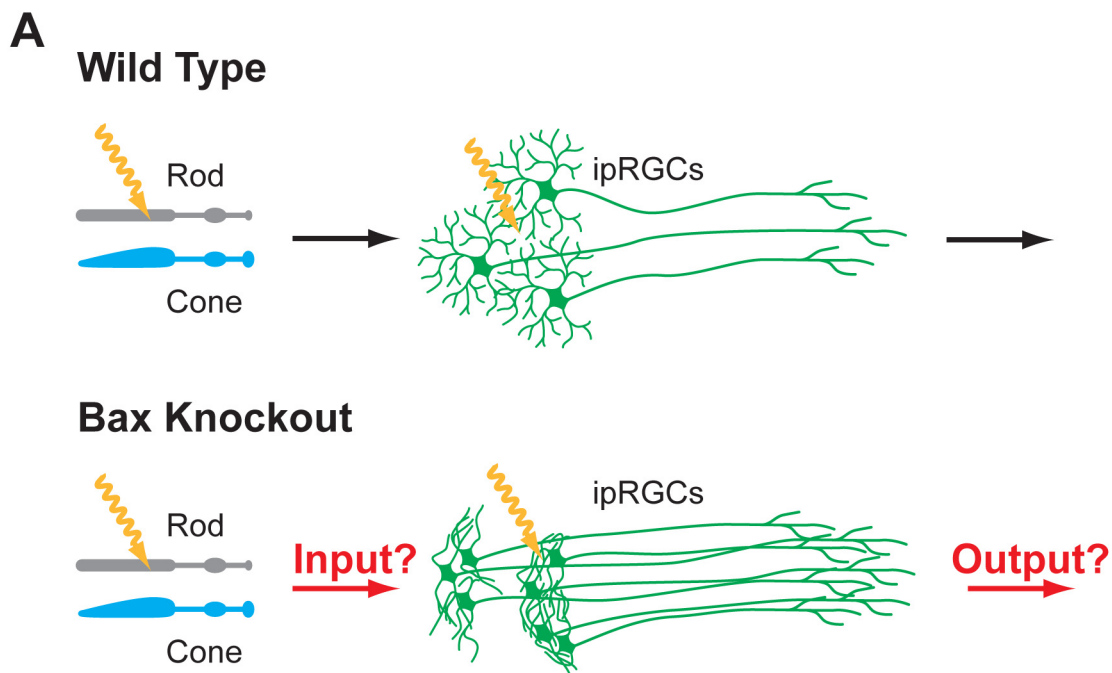
Figure 4. Axonal targeting remains in Bax knockout
(A) Model describing how lack of apoptosis in ipRGCs might affect reception of light information from rods and cones, and/or transmission of light information to downstream nuclei in the brain. (B) Axons from ipRGCs were labeled by X-gal staining with the Opn4tau-LacZ reporter allele in coronal sections of the SCN (left panel), OPN (middle panel), and IGL (right panel). ipRGC axons still confine to the SCN, OPN, and IGL in the Bax KO similar to the control. (Scale bar 100μm)
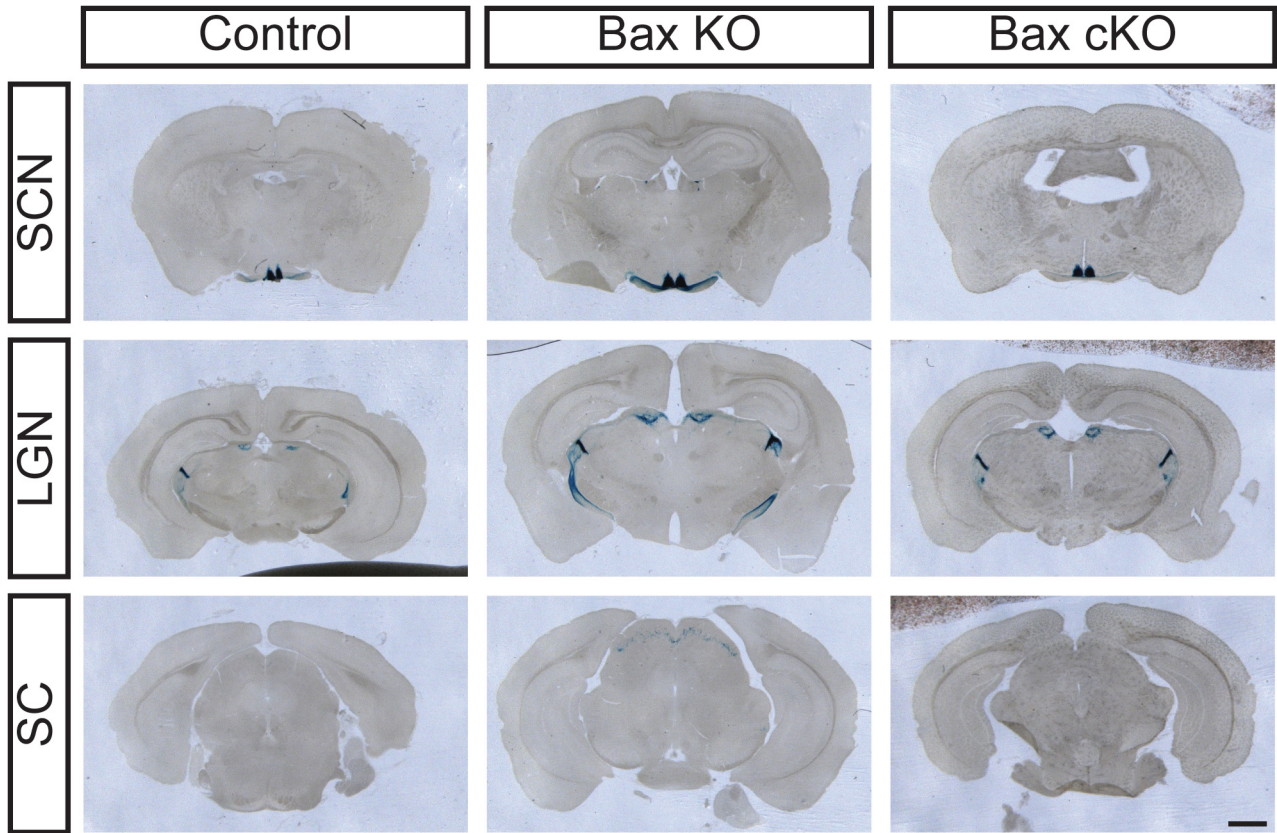
Figure 5. Normal ipRGC targeting in Bax mutant mice
Low magnification images of X-gal staining on coronal brain sections showing ipRGC innervation of the SCN, LGN, OPN, and SC in Opn4LacZ/+ (control), Opn4LacZ/+; Bax -/- (Bax KO), and Opn4LacZ/+; Baxfl/fl (Bax cKO) mice. These images clearly show that ipRGC projections in Bax KO and Bax cKO mice properly reach non-imaging forming targets and do not form ectopic innervations. (Scale bar 1mm)

A long-standing view in the circadian field is that the radiating dendritic arbors of spaced ipRGCs are necessary to form an evenly distributed receptive net in order to increase the area for photon capture to allow photoentrainment (Provencio et al., 2002). Given the disrupted features of the ipRGC mosaic in *Bax* mutants, we tested circadian photoentrainment using wheel-running activity. Surprisingly, *Bax* mutant animals are able to photoentrain to a 12hr:12hr light dark cycle similar to controls (Figure 7A and B; Wild type and *Bax* KO). The mutants had similar circadian period length to wild type animals (Figure 7A and C), and presenting a single pulse of light of 15-minute duration caused similar phase shifts in the *Bax* mutant and control mice (Figure 7A, and D). In addition, exposing the animals to constant light (LL), wild type and *Bax* mutants show similar lengthened circadian periods compared to constant darkness (Figure 7A and C). Finally, the wild type and *Bax* mutant mice can fully re-entrain to a 24-hour light-dark cycle and mask under a 3-hour light pulse or under a 7-hour (ultradian) light-dark cycle (Figure 7A). Together, these behavioral studies indicate that *Bax* mutants were able to respond to various circadian light paradigms indistinguishably from wild type mice (Figure 7A left two panels and 4B-D). This indicates that the loss of apoptosis, the disrupted cellular spacing and the altered dendritic morphologies in *Bax* mutants do not impair the output of light signals from ipRGCs to the brain as revealed by several light-dependent circadian functions (Figure 4).

We next sought to determine if the disrupted mosaic features in the *Bax*$^{-/-}$ mice would affect the ability of ipRGCs to receive light input originating from rods and cones. We show that electroretinograms (ERGs) from the *Bax*$^{-/-}$ animals are indistinguishable from wild type animals (Figure 6A), indicating that the *Bax* deletion does not alter outer retinal signaling between the classical photoreceptor rods and cones and their immediate synaptic partners. In addition, *Bax* mutants are able to visually locate a platform in the Morris water maze similar to wild type
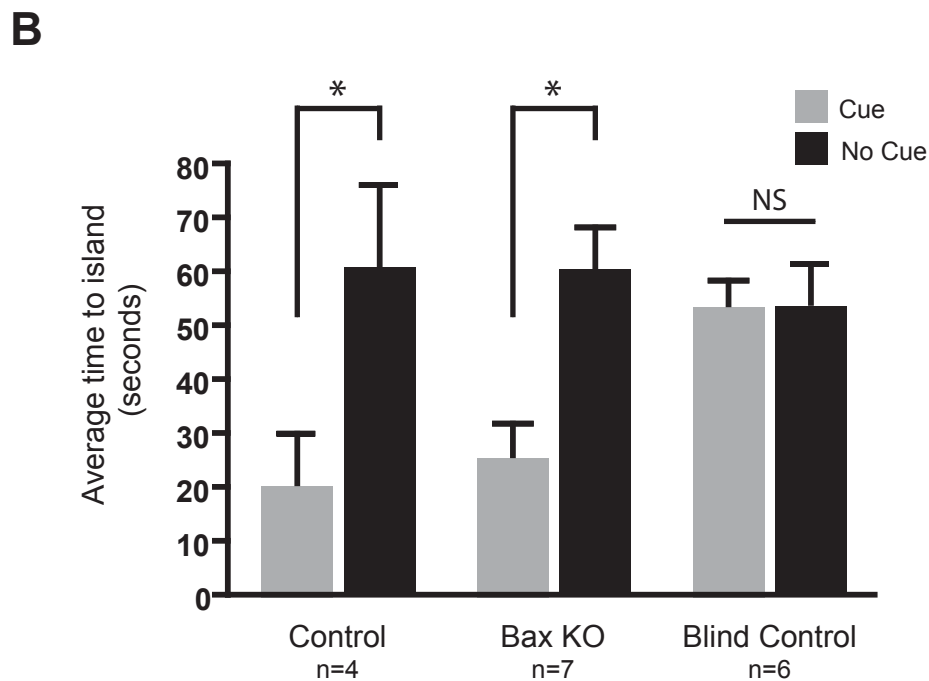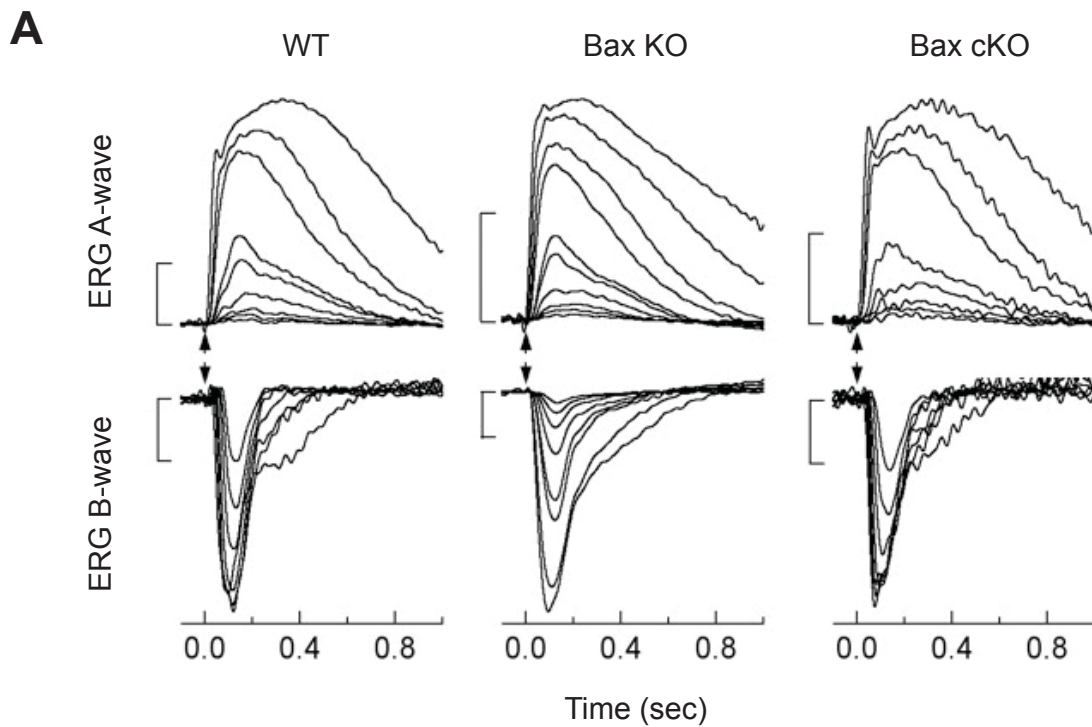
Figure 6. The functional circuitry of the outer retina in Bax mutants is intact
(A) Isolated electroretinogram (ERG) A-waves and B-waves were measured in WT, Bax knockout, and conditional Bax knockout retinas. Flash strengths for A-waves were 0.70, 1.7, 3.7, 9.9, 29, 45, 260, 960, and 5000 photons/mm2, and flash strengths for B-waves were 0.70, 1.7, 3.7, 9.9, 29, 45, and 260 photons/mm2, with Bax knockouts also including a flash at 960 photons/mm2. Scale bars for A-waves are 0.2 mV, scale bars for B-waves are 0.1 mV. (B) Performance of control, Bax KO and enucleated (blind) mice using visually marked platform in the Morris water maze paradigm. Gray bars indicate the time required for mice to find a hidden platform with a visual cue after 5 days of training. Black bars indicate the time required for mice to find a hidden platform without a visual cue. Bax KO and wild type mice but not blind mice find the platform much faster when a cue is present. n= 7 for Bax KO and 5 for both control and enucleated groups. * indicate p<0.05 with paired t-test, Mean±SEM.
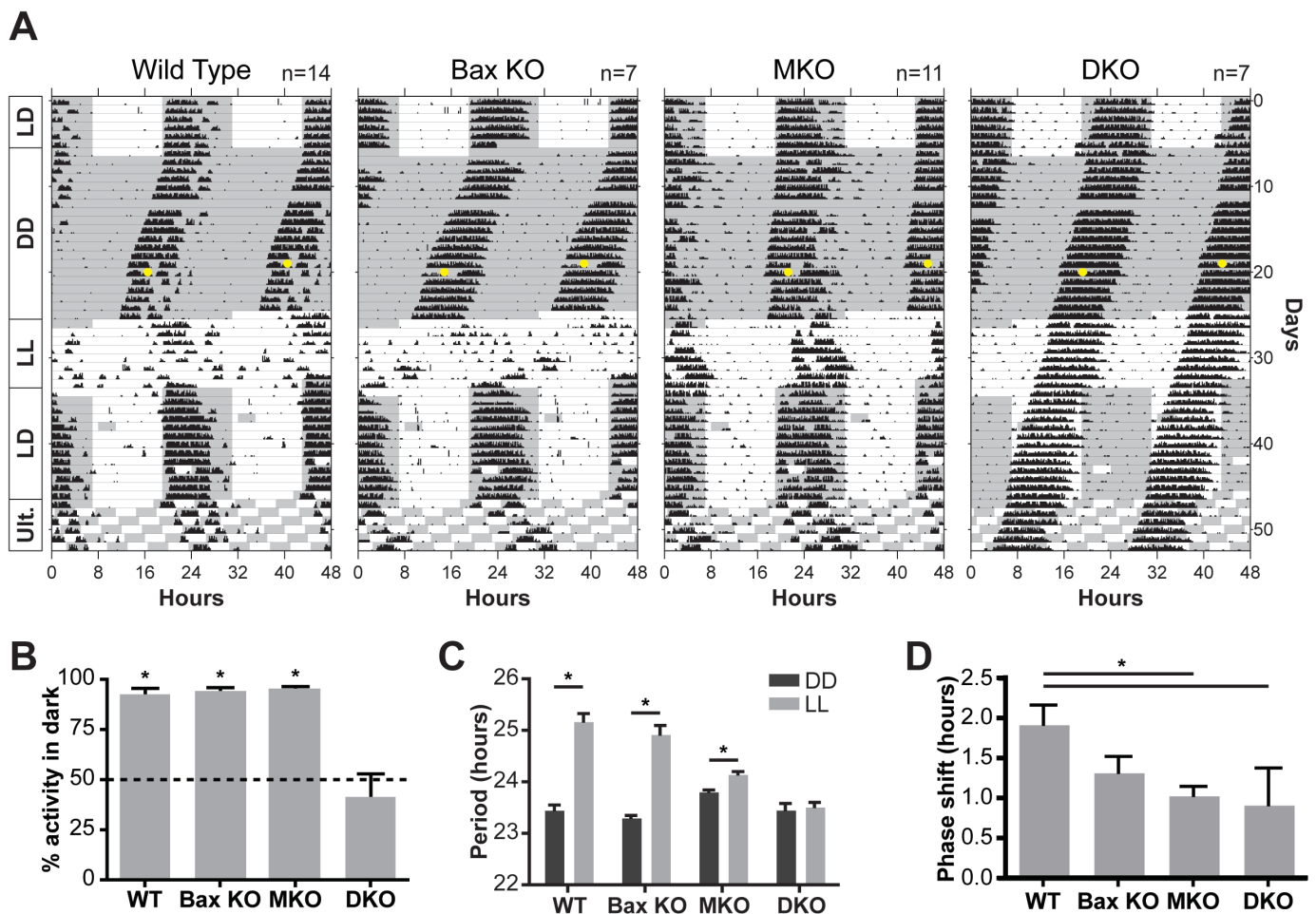
Figure 7. Rod/cone input to ipRGCs is highly attenuated in Bax knockout mice
(A) Wheel-running actograms from wild type (WT), Bax KO, Opn4 KO (MKO), and Bax/Opn4 double KO (DKO) mice. Only DKO mice were unable to entrain their activity to different light cycles: 12:12 hour light:dark (LD), constant darkness (DD), constant light (LL), and ultradian cycle (3.5:3.5 hour light:dark). The gray background denotes when lights were off. (B) DKO mice were unable to confine their activity to the dark portion of the 12:12 LD cycle in (A), as indicated by no significant difference from 50% (t-test, * indicates $p<0.05$). (C) DKO mice did not lengthen their period under constant light (paired t-test, * indicates $p<0.05$). (D) A 15-minute light pulse at CT16 (circles in b) generated a similar phase shift in all groups of mice (no significant difference by one-way ANOVA with Tukey post hoc). For all graphs mean±SEM.
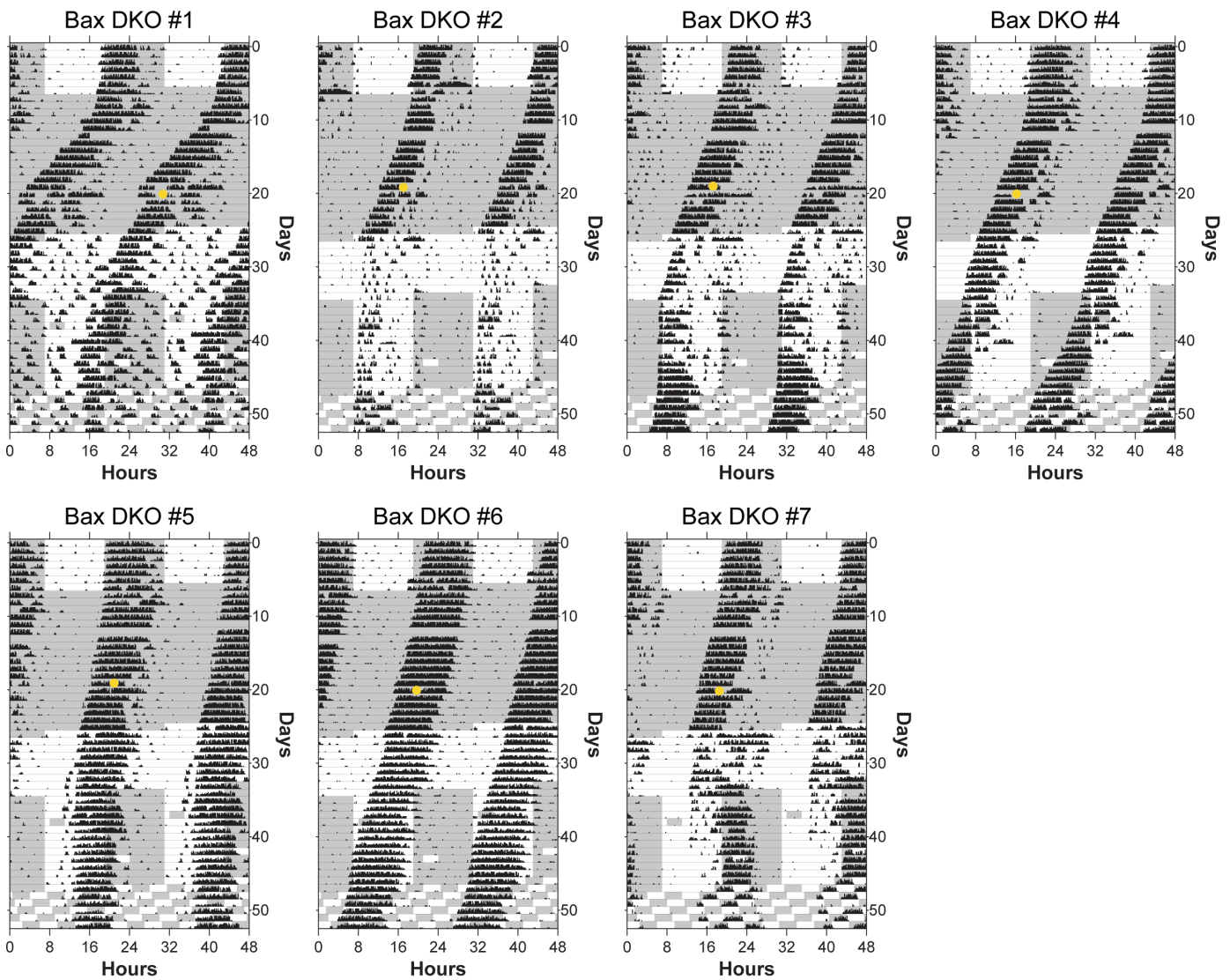
Figure 8. Actograms for all Bax and Opn4 double knockout mice
Individual actograms for all Bax-/-; Opn4-/- double knockout animals we used in this study. 2/7 completely free ran during the light dark cycle similar to triple knockout animals (#4 and #6). Animal #5 seems to free run, but the length of the circadian period is close to 24 hours precluding us from confidently assigning this animal as a free runner. However, this mouse at best has a highly advanced phase relation to the light dark cycle. Animal #1 shows an unstable phase relation to the light dark cycle. The remaining three animals although show association with the light dark cycle, only # 7 (day 42) seems to eventually entrain to the light dark cycle. (Control groups and Bax-/- animals are not shown, but all of them showed circadian photoentrainment with a stable phase angle to the light dark cycle).

animals (Figure 6B). To test the extrinsic rod-cone input to ipRGCs in the context of the *Bax* deletion, we eliminated the intrinsic melanopsin-based photoreception ($Opn4^{tau-LacZ/tau-LacZ}$, referred to here as $Opn4^{-/-}$, Table 1) in $Bax^{-/-}$ mice and subjected the double knockout animals ($Bax^{-/-}$; $Opn4^{-/-}$) to the same circadian light paradigms as above (Figure 7A, Table 1; DKO). As a control, we used the $Opn4^{-/-}$ mice (MKO). As previously demonstrated, the $Opn4^{-/-}$ mice are able to photoentrain, but show attenuated period lengthening in LL and a decrease in phase shifting magnitude in response to light (Figure 7A and D, MKO)(Panda et al., 2002; Ruby et al., 2002). The ability of the $Opn4^{-/-}$ mice to photoentrain indicates that ipRGCs rely on the extrinsic input from rods and cones to convey light information for photoentrainment in the absence of the melanopsin protein. In contrast to the $Opn4^{-/-}$ mice, photoentrainment was severely impaired in all $Bax^{-/-}$; $Opn4^{-/-}$ (DKO) mice (Figure 7A right panel). The majority of $Bax^{-/-}$; $Opn4^{-/-}$ mice free-ran regardless of the light-dark cycle (Figure 8), showing equal amounts of activity (~50%) in the light and dark portions of the cycle (Figure 7B). This behavior is comparable to the free-running response seen in mice lacking rod, cone and ipRGC phototransduction pathways ($Gnat1^{-/-}$; $Cnga3^{-/-}$; $Opn4^{-/-}$, referred to here as triple KO animals) (Hattar et al., 2003). Similar to the triple KO animals, $Bax^{-/-}$; $Opn4^{-/-}$ mice were also unable to lengthen their period in constant light (Figure 7C). Thus, loss of Bax disrupts the ability of ipRGCs to receive extrinsic input from rods and cones. However, in contrast to the triple KO mice, the $Bax^{-/-}$; $Opn4^{-/-}$ mice retain a limited capacity to respond to rod-cone input; the $Bax^{-/-}$; $Opn4^{-/-}$ mice still show a similar phase-shift as $Opn4^{-/-}$ mice in response to a 15-minute light pulse (Figure 7D). These results show that the loss of Bax perturbs the rod/cone input to circadian photoentrainment.

Since the *Bax* deletion in the conventional knockouts may affect all retinal cell types in addition to ipRGCs (White et al., 1998), we employed a conditional approach to test the cell

autonomous role of Bax in ipRGCs. We conditionally deleted *Bax* in ipRGCs by mating *Opn4^{Cre}*

mice with animals harboring a floxed *Bax* allele (*Bax$^{fl/fl}$; Opn4$^{Cre/+}$;* Table 1) (Ecker et al., 2010;

Takeuchi et al., 2005) and show normal axonal targeting of ipRGCs to the brain (Figure 9A).

Autocorrelation analysis in the *Bax$^{fl/fl}$; Opn4$^{Cre/tau-LacZ}$* (Table 1) mice show deficits in ipRGC

spacing similar to those seen in the conventional *Bax$^{-/-}$* retina (Figure 9B and C; compare with

Figure 1C and D, right panels). In contrast to *Bax$^{-/-}$* animals, however, ipRGC dendrites from the

Bax$^{fl/fl}$; Opn4$^{Cre/tau-LacZ}$ animals were not fasciculated (Figure 9B) and ipRGC cell density was

similar to wild type animals (Figure 9B and C; compare with Figure 1C and D, left panels).

These milder phenotypes are likely due to the inefficient deletion of *Bax* by the melanopsin-

driven Cre recombinase. Consistent with this hypothesis, Bax antibody staining in conditional

Bax mutants shows residual Bax immunoreactivity in some melanopsin cells compared to the

conventional *Bax* mutants where no Bax staining is seen (Figure 10A). In addition, using

Math5$^{Cre/+}$, where Cre driven deletion of *Bax* occurs at an earlier developmental point than in the

Bax$^{fl/fl}$; Opn4$^{Cre/+}$ mice (McNeill et al., 2011; Yang et al., 2003), we show the increase in cell

numbers and the fasciculated dendritic morphologies observed in the conventional *Bax* mutants

(Figure 10B). However, even without increased cell number and fasciculated dendrites, the

conditional *Bax$^{-/-}$* mice show deficits in cell spacing evidenced by autocorrelation analysis

(Figure 9C). We further determined that in *Bax$^{fl/fl}$; Opn4$^{Cre/+}$* mice, loss of the minimal spacing

between neighboring cells manifests itself as a less regular mosaic, evidenced by both the

Voronoi domain and nearest neighbor regularity indexes (Figure 9D, E and F). The conditional

mice show less of an effect upon their Voronoi domain regularity indexes compared to *Bax$^{-/-}$*

mice (Figure 9D and E), since their lower density rarely yields many close neighbors to generate
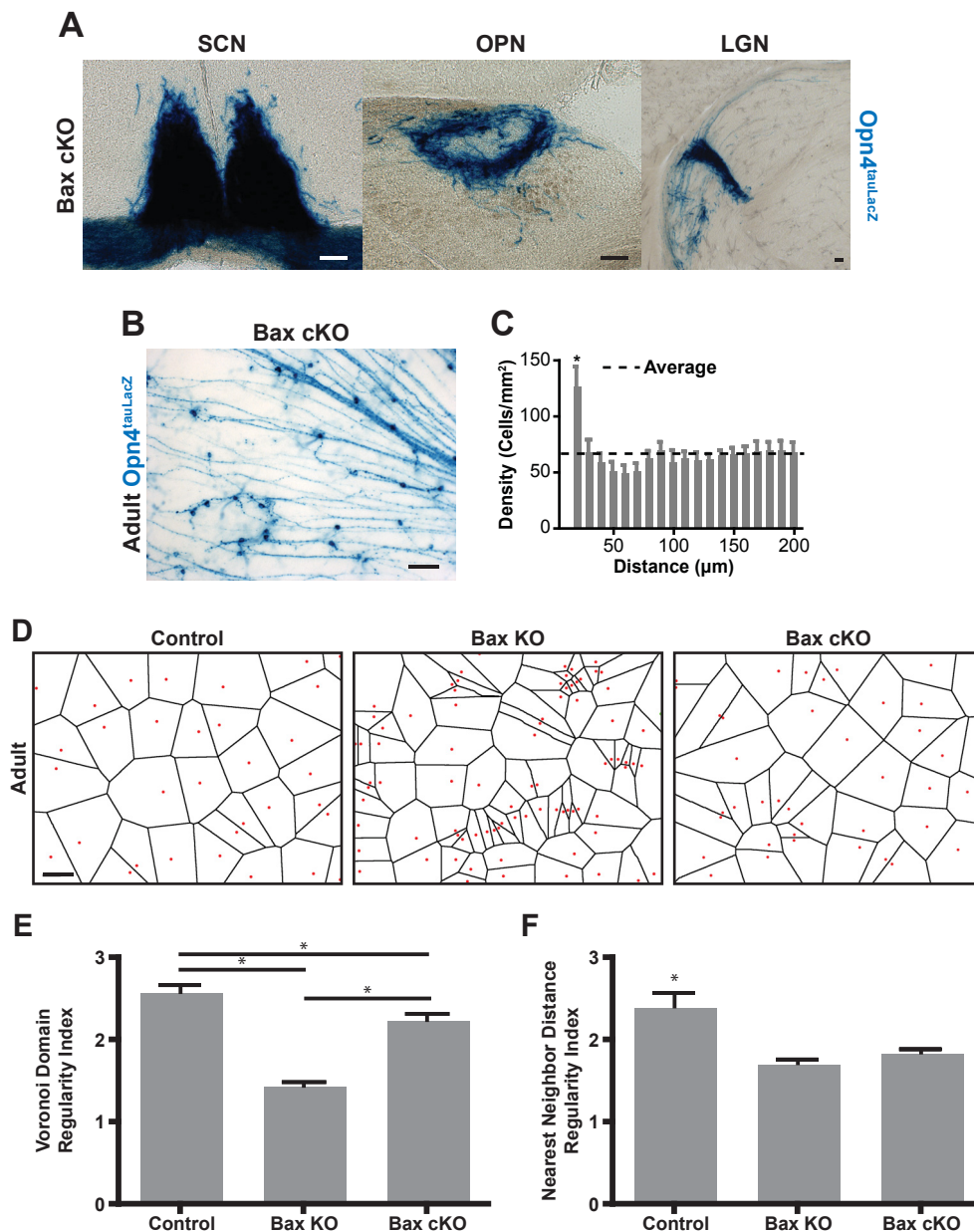
Figure 9. Conditional Bax knockout in ipRGCs disrupts spacing

(A) X-gal staining of ipRGC axons in the conditional Bax KO with the Opn4tauLacZ reporter allele reveals that they still confine to the SCN, OPN, and IGL similar to the control. (Scale bar 100μm) (B) X-gal staining of ipRGCs in a whole-mount retina from a Bax conditional KO adult (Bax cKO), scale bar 100μm. (C) Density recovery profile for the Bax cKO shows that ipRGCs form a similarly clumped distribution to the germline Bax KO (figure 1D, right panel), even though the Bax cKO does not have a higher density of ipRGCs than the control (figure 1D, left panel). (D) comparison of Voronoi tessellations for ipRGCs from Control, Bax KO, and Bax cKO mice. Red dots indicate the position of ipRGC cell bodies as determined by X-gal staining. Note that these diagrams correspond to the images shown in Figure 1C and 5B. (E) Voronoi Domain Regularity Index shows a significant reduction in regularity in the Bax KO due to the presence of clumping, while the Bax cKO shows an intermediate phenotype. (F) The Nearest Neighbor Regularity Index shows a comparable reduction for the mosaics in both Bax KO and Bax cKO retinas (one-way ANOVA with Tukey post hoc, n=6 retinas per group, * indicates $p<0.05$, mean±SEM).
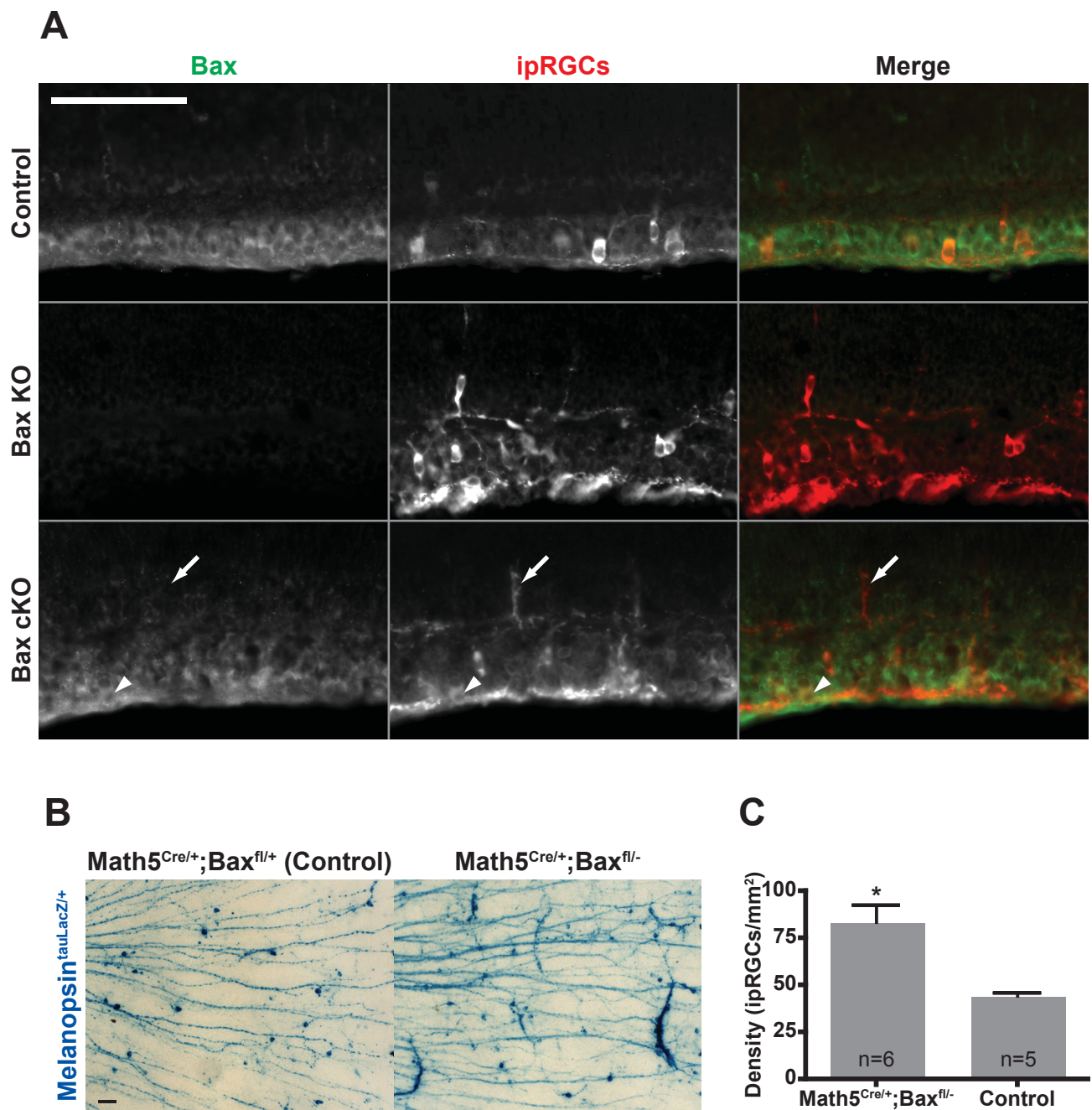
Figure 10. Conditional Bax-KO mice have only partial deletion of Bax in ipRGCs.
(A) Double labeling of ipRGCs (middle panel) using an anti b-gal antibody in retinal cross-sections at P3 and an antibody against all forms of Bax (active and inactive, left panel) in control, Bax KO, and conditional Bax KO (Bax cKO). Some ipRGCs are still positive for the Bax protein in the Bax cKO (arrowhead), and some are not (arrow). (B) Opn4tau-LacZ labeling of whole mount retinas from control and Math5Cre/+;Baxfl/-; Opn4tau-LacZ/+ mice. (C) Quantification shows that the Math5Cre/+;Baxfl/- have higher cell density than the control and Opn4Cre/+; Baxfl/- mice shown in Figure 5B and C (n=5-6 retinas in each group, * indicates $p<0.05$ by t-test, Mean±SEM, scale bar 100μm for A and B).

very small domains. They do, however, show nearest neighbor regularity indexes similar to those in the $Bax^{-/-}$ retina.

We subsequently tested photoentrainment in the wild type and conditional Bax mutants. As predicted from the conventional $Bax^{-/-}$ mice, the conditional $Bax^{-/-}$ shows normal circadian photoentrainment in the presence of melanopsin phototransduction pathway. Similar to $Bax^{-/-}$; $Opn4^{-/-}$ animals, the majority of mice lacking the melanopsin protein and Bax selectively in the ipRGCs ($Bax^{fl/fl}$; $Opn4^{Cre/tau-LacZ}$, cDKO) exhibited significant photoentrainment deficits with a subset showing a mild photoentrainment deficits (Figure 11 and Figure 12). As expected, ERG recordings from the conditional Bax mutants showed no deficits in outer retinal circuitry (Figure 6A). These results show that even partial developmental deletion of Bax in $Bax^{fl/fl}$; $Opn4^{Cre/tau-LacZ}$ mice is sufficient to disrupt the organization of M1 ipRGCs and cause circadian photoentrainment deficits.

Bax-mutant mice show ectopic retinal lamination, an increase in ectopic synapses within the inner nuclear layer, and impairments in rod-cone mediated activation of ipRGCs

To assess the anatomical and physiological underpinnings of this disruption in rod-cone input to ipRGCs, we focused on *Bax*-mutant mice because of the greater effects upon the organization of the ipRGC mosaic and the greater consistency in the behavioral deficits across *Bax*-mutant mice. We first examined the dendritic architecture of ipRGCs in retinal sections. ipRGC dendritic arbors were frequently misplaced to ectopic locations within the middle of the inner nuclear layer (INL) (arrowheads in Figure 13A, bottom panels labeled green) spanning the whole retina (Figure 14). Coincident with such misplaced dendrites, an ectopic cell-sparse synaptic layer was observed to form within the INL (Figure 13A, labeled red) that receives ON
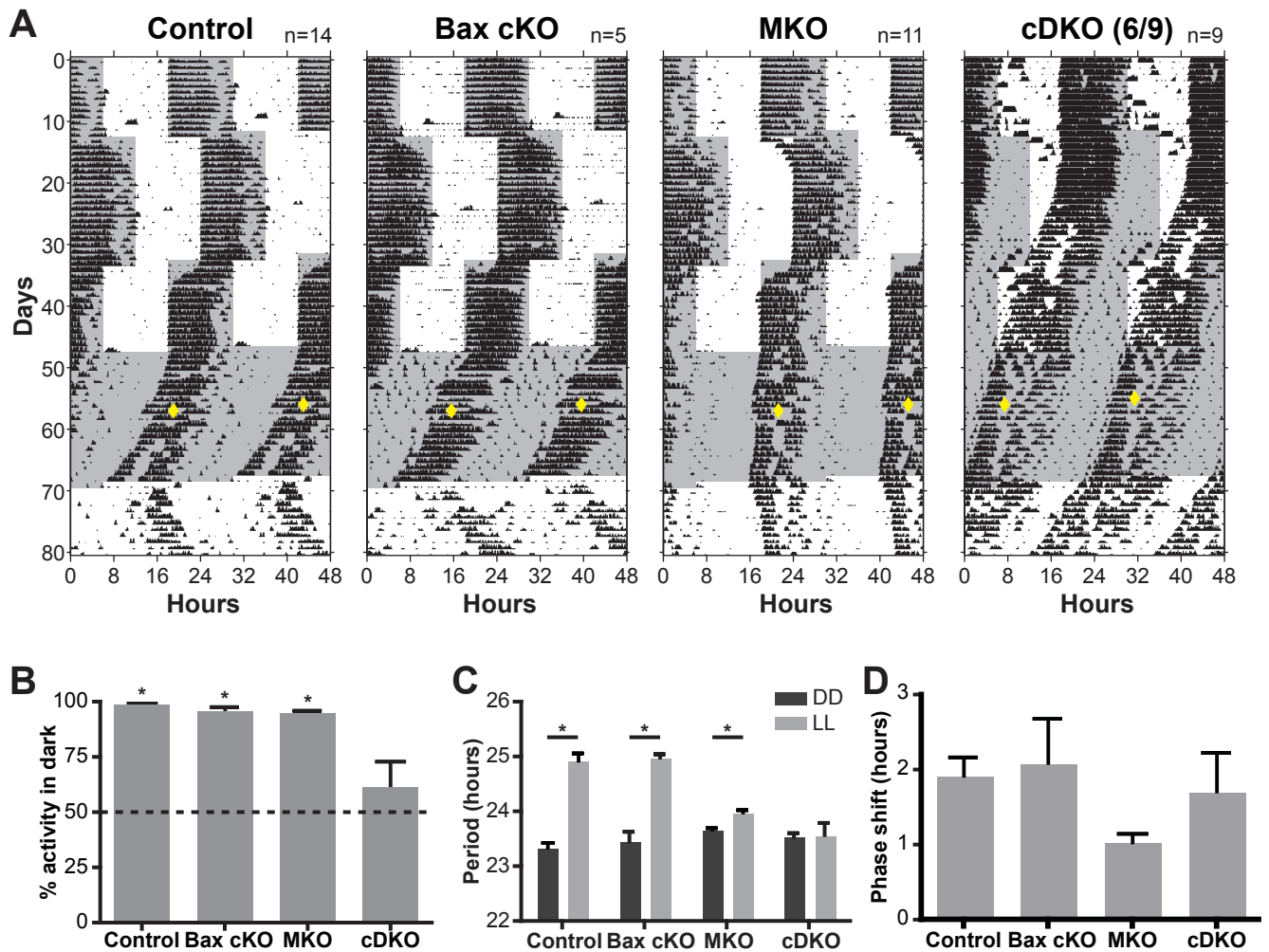
Figure 11. Conditional Bax knockout in ipRGCs attenuates rod/cone input
(A) Wheel-running actograms from control, Bax conditional knockout (Bax cKO), Opn4 KO
(MKO), and Bax conditional /Opn4 double KO mice (cDKO). The majority of cDKO mice (6 out
of 9) show significant deficits in their responses to different light cycles: 12:12 hour light:dark
(LD) with 6-hour phase delay and advance, constant darkness (DD), and constant light (LL). The
gray background denotes when lights were off. (B) cDKO mice were unable to confine their
activity to the dark portion of the 12:12 LD cycle in (A), as indicated by no significant difference
from 50%. (C) cDKO mice did not lengthen their period under constant light. (D) a 15-minute
light pulse at CT16 phase shift (diamonds in A) generated a similar phase shift in all groups of
mice.* indicates $p < 0.05$ with a one-way ANOVA with Tukey post hoc, Mean±SEM)

Mild

cDKO #1

cDKO #2

cDKO #5

Severe

cDKO #3

cDKO #4

cDKO #6

cDKO #7

cDKO #8

cDKO #9
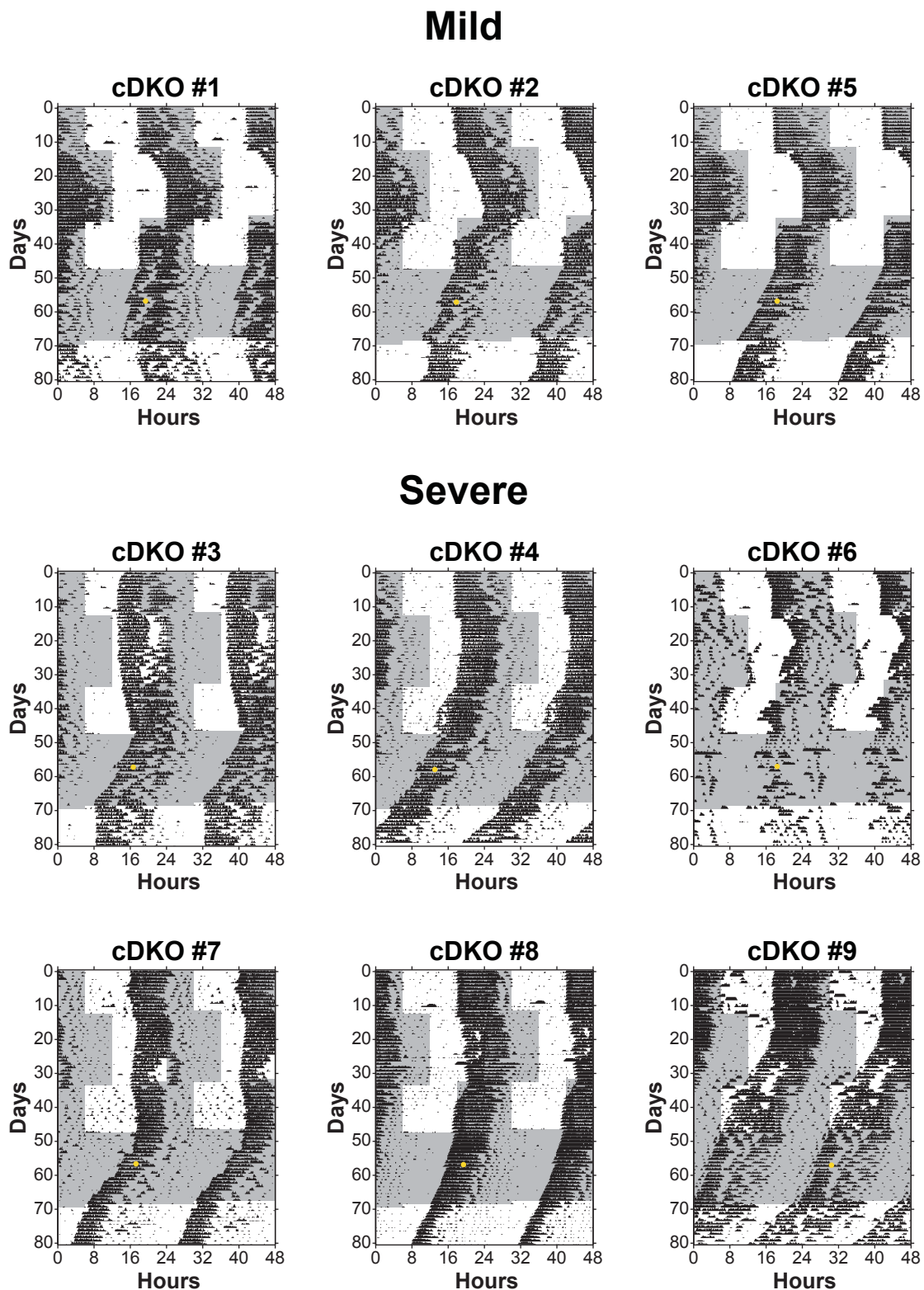
Figure 12. Actograms for all conditional Bax; Opn4 double knockout (cDKO) mice
cDKO mice show two separate groups for circadian photoentrainment; mild and severe.
Three out of the nine cDKO mice were able to photoentrain to the jet-lag paradigm,
whereas six out of the nine did not show photoentrainment. However, nearly all (8 out
of the 9 animals) show a severe phenotype by their inability to lengthen their periods in
constant light compared to constant dark.

synaptic input from bipolar cells (Figure 13B). Specifically, there is an increase in the number of

ectopic ON synapses within the INL in $Bax^{-/-}$ animals compared to controls, whereas,

surprisingly, the number of en passant ON synapses, normally observed between ON-bipolar

cells and ipRGCs in S1 of the inner plexiform layer (IPL) (Dumitrescu et al., 2009), remains

exactly the same (Figure 13C). We further investigated the colocalization of a synaptic partner of

ipRGCs, the dopaminergic amacrine cell, which normally co-stratifies with ipRGCs in the

outermost stratum S1 of the IPL (Matsuoka et al., 2012; Zhang et al., 2008a) (Figure 13A,

bottom panels, labeled blue). In the $Bax^{-/-}$ retina, such dopaminergic processes are also

mislocalized to the ectopic synaptic layer embedded within the INL (Figure 13A, bottom panels).

ipRGCs, therefore, are not only disrupted in their spacing, but also show abnormalities in the

distribution of their dendrites across the depth of the retina and in the location of their synaptic

contacts with ON bipolar and dopaminergic amacrine cells. These morphological and behavioral

data from *Bax* mutant animals strongly indicate that the *Bax* mutation causes disruptions in

normal ipRGC circuitry within the retina.

To directly determine whether rod-cone signaling to ipRGCs in the retina was altered in

$Bax^{-/-}$ animals, we assessed light dependent retinal activation of ipRGCs by performing cFos

immuno-staining in $Bax^{-/-}$ animals that also lack the melanopsin protein. Specifically, we

colabeled cFos and ipRGCs using double immunofluorescence with beta-galactosidase as a

marker for ipRGCs in whole mount retinas from $Opn4^{tau\text{-}LacZ/tau\text{-}LacZ}$ mice and $Bax^{-/-}; Opn4^{tau\text{-}LacZ/tau\text{-}LacZ}$ mice. In $Opn4^{tau\text{-}LacZ/tau\text{-}LacZ}$ mice, 20% of ipRGCs showed detectable cFos staining

after 30 minutes of light exposure. In contrast, in $Bax^{-/-}; Opn4^{tau\text{-}LacZ/tau\text{-}LacZ}$ double mutant mice,

only 10% of ipRGCs showed cFos staining under the same light conditions (Figure 15A and B).
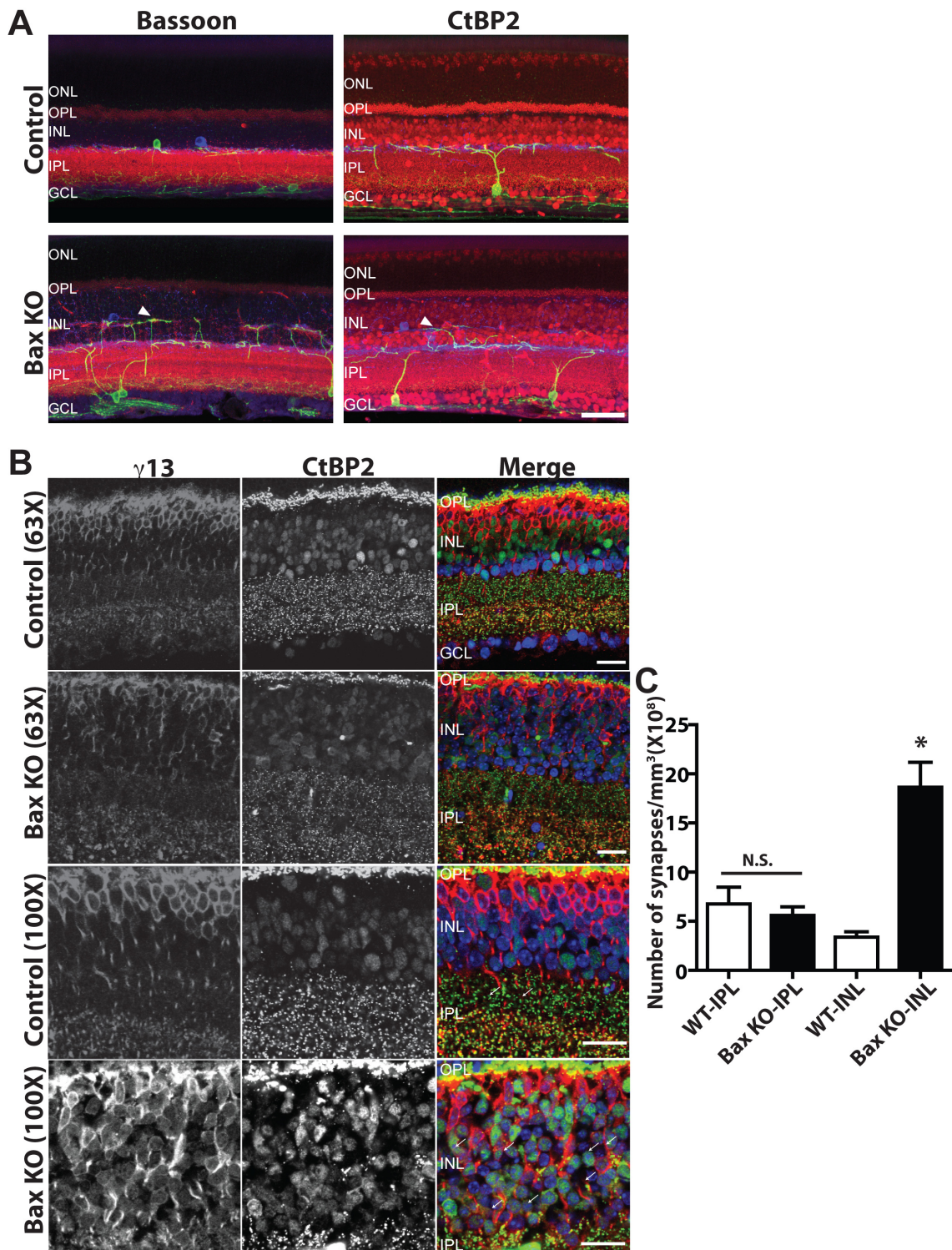
Figure 13. Altered dendrite morphology and increased in ectopic synaptic input
(A) Immunofluorescence of retinal sections for melanopsin (green), tyrosine hydroxylase (blue) and synaptic markers (red; Bassoon for left panel and CtBP2 for right panel) in both control (upper panel) and Bax mutant mice (lower panel). In Bax-/- mice, an ectopic synaptic stratum from ipRGCs and TH-amacrine cells was observed within the INL (arrowheads). (ONL: outer nucleus layer, OPL: outer plexiform layer, INL: inner nucleus layer, IPL: inner plexiform layer, GCL: ganglion cell layer). Scale bars 50 µm. (B) Double-staining of ON bipolar cells (γ13) and ribbon synapses (CtBP2) shows conspicuous ON bipolar associated synapses within this ectopic synaptic region (examples are indicated by white arrows; scale bar = 20 µm). (C) Quantification of these double-labeled synaptic profiles shows a 6-fold increase in the number of synapses in the INL in Bax-/- animals while the number of en passant ON synapses in S1 of the IPL, which often occur between ipRGCs and ON bipolar cells, remains the same as in controls (* indicates p<0.001 by t-test, mean±SEM).

A

WT

Bax KO

WT   Bax KO
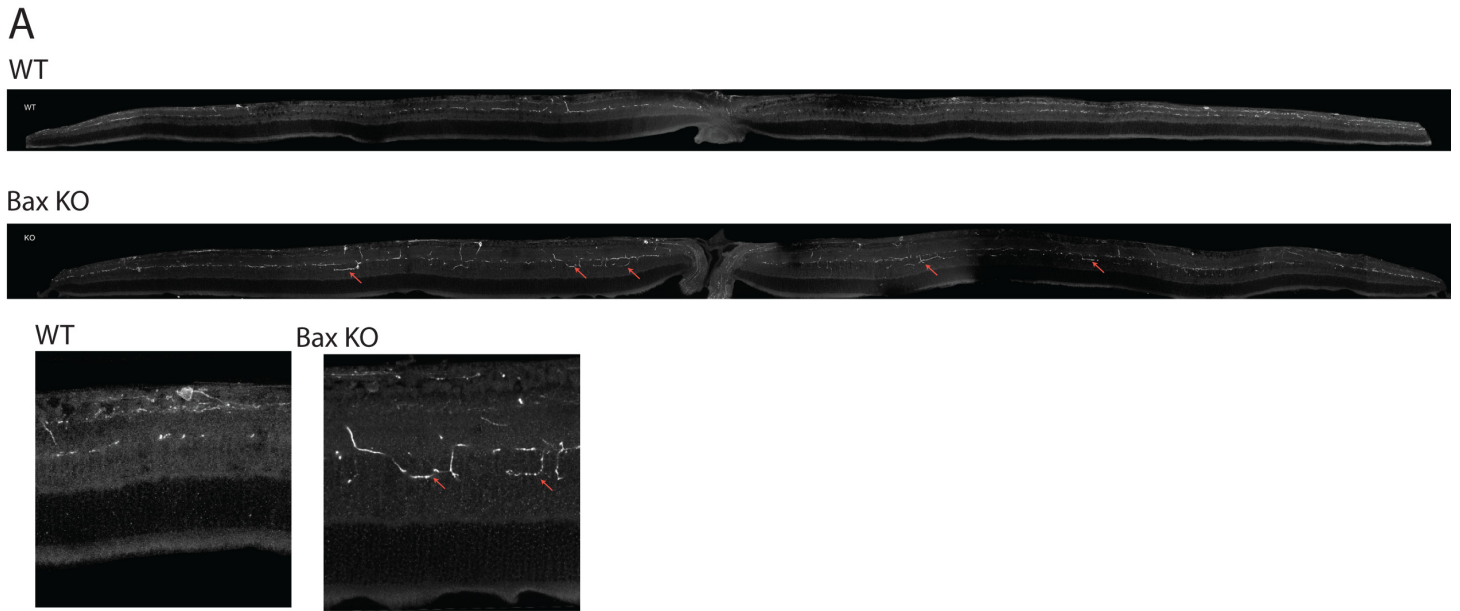
Figure 14. In Bax-KO mice, dendrites of ipRGCs are ectopically present across the INL
Montage of melanopsin staining in control and Bax-/- animals showing that the ectopic layer of ipRGC dendrites in the INL spans the retina (examples are indicated by red arrows).
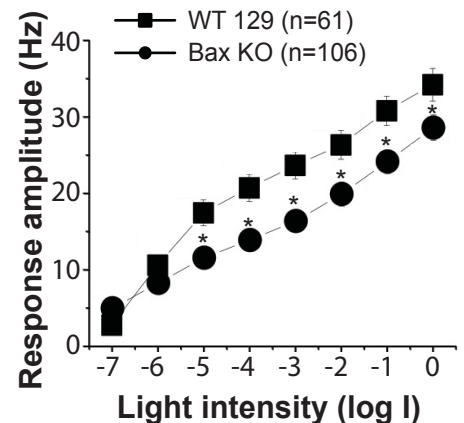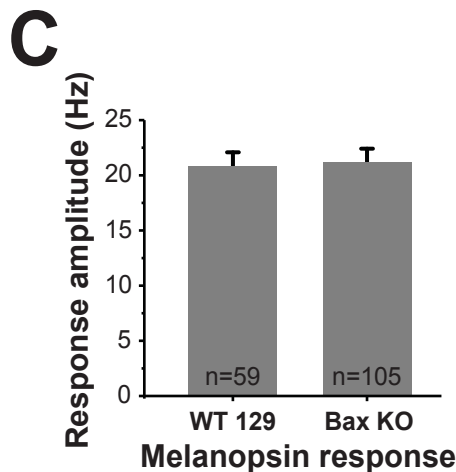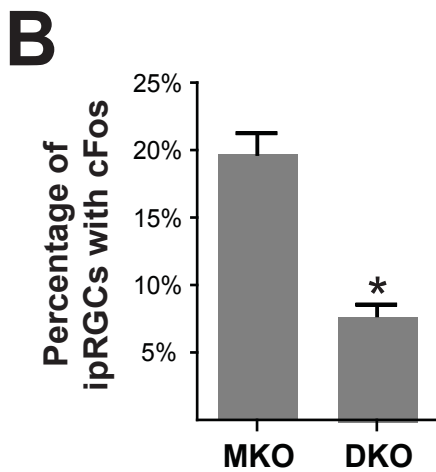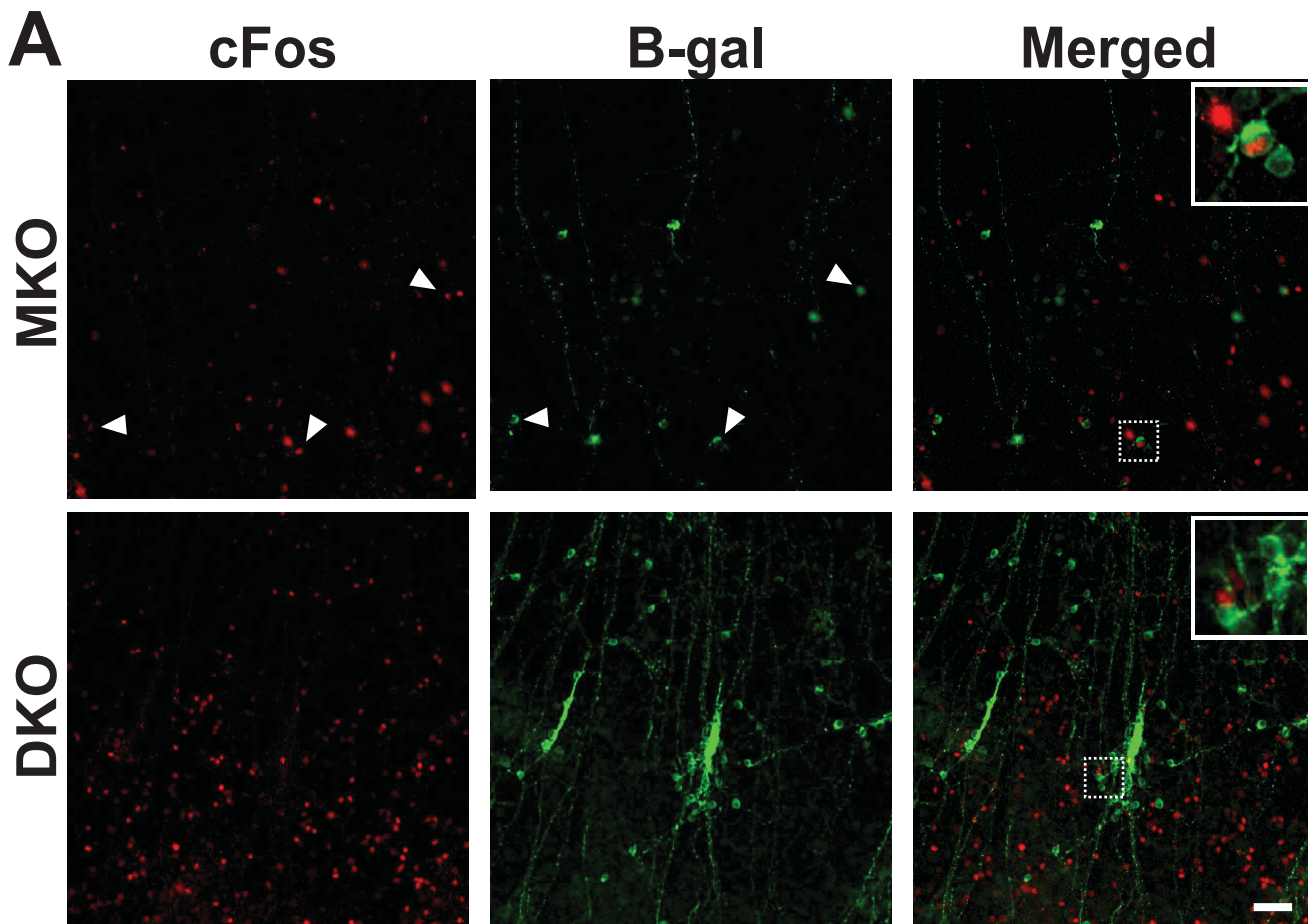
Figure 15: Disrupted light signal from outer retina to ipRGCs
(A) Immunoflorescence of whole mount retina for cFos (red) and LacZ (green) in MKO (Opn4tau-LacZ/tau-LacZ) and DKO (Opn4tau-LacZ/tau-LacZ; Bax-/-) mice after 30 min of light exposure. No cFos activation was observed within clumped ipRGCs in DKO mice. Scale bars 50 μm. (B) Quantification of cFos positive ipRGCs after 30 min of light exposure. DKO mice show a significantly lower percentage of cFos positive ipRGCs than MKO mice. (C) Electrophysiological recording of melanopsin response from ipRGCs under the synaptic blocker cocktail from both control and Bax mutant mice. (D) Electrophysiological recording of ipRGCs spike frequency under various light intensities using multi-electrode array. Light response from ipRGCs in Bax-/- mice is significantly weaker across different light intensities. ipRGCs were identified after application of the synaptic blocker cocktail. (* indicates p<0.05 by t-test, mean±SEM)

No cFos staining was detected in clumped ipRGCs (inset in Figure 15A bottom right panel). These results indicate that outer retinal signaling to ipRGCs is diminished in the *Bax*^{-/-} mice.

To quantitatively analyze the deficits in rod-cone input to ipRGCs, we also performed electrophysiological recordings from ipRGCs in the *Bax*^{-/-} mice using multi-electrode array (MEA) recordings. Since we had to identify ipRGCs in the MEA recordings based on their intrinsic photosensitivity, these analyses could not be carried in *Bax*^{-/-}*; Opn4*^{-/-} animals. We did not detect any significant differences in the intrinsic response recorded from ipRGCs from *Bax*^{-/-} and control animals (Figure 15C), in agreement with our behavioral data that *Bax*^{-/-} mice show normal melanopsin-dependent circadian light responses. To reveal rod-cone input, we conducted an intensity response curve starting with light intensities that are within the threshold for rod and cone responses, but are known to be sub-threshold for the melanopsin intrinsic light response. We found that the ipRGCs in *Bax*^{-/-} mice showed significantly weaker light responses compared to control animals, across several light intensities (Figure 15D). This decrement in rod-cone light input to ipRGCs is in agreement with our behavioral studies showing deficits in circadian light functions only in the absence of the melanopsin protein. Together, our morphological and functional analyses in the retina confirm that ipRGCs in the *Bax*^{-/-} mice have deficits in relaying the rod-cone input but preserve their ability to signal light information with melanopsin photopigment.

<u>DISCUSSION</u>

Over the past few decades, research has shown that neurons are initially overproduced during development, only to be reduced to adult levels by programmed cell death (apoptosis).

Surprisingly, in the nervous system, the elimination of Bax-mediated apoptosis results in overproduction of neurons but causes very few and only subtle functional deficits (Autret and Martin, 2009; Jiao and Li, 2011; Jonas et al., 2005). In this study, we show that apoptosis plays a critical role in generating the proper spacing and functional circuitry of ipRGCs that mediate a form of visual behavior.

The mammalian retina performs two major tasks, vision and irradiance detection (Provencio et al., 2002; Wässle, 2004). For visual functions, the orderly arrays of retinal mosaics are critical for the detection and transmission of spatial detail to central visual targets. In contrast, irradiance detection is only concerned with detecting ambient light intensity with no need for spatial resolution. The M1 ipRGCs, which predominantly contribute to irradiance detection for circadian photoentrainment and the pupillary light reflex (Chen et al., 2011), show a spaced mosaic across the retina and their dendrites form an extensive receptive net (Figure 16). Since M1 ipRGCs mediate irradiance detection, it has been assumed that their spaced distribution and uniform net of dendrites are important for enhanced photon capture (Provencio et al., 2002). In *Bax* mutant mice, however, lacking the regular cellular spacing and evenly distributed network of M1 ipRGCs that typify the wild-type retina, circadian light responses were indistinguishable from wild-type mice in the presence of the melanopsin protein. In contrast, *Bax* mutant mice were impaired in their circadian photoentrainment when only the rod-cone pathway was driving the ipRGCs. This indicates that the normal mosaic properties of M1 ipRGCs are dispensable for their intrinsic photoresponses, but suggests cell spacing is required for rod-cone input.

Previous studies suggest that the dendritic arbors of M1 ipRGCs are cell-intrinsically determined, rather than being sensitive to homotypic neighbors (Lin et al., 2004). Consistent with this data, we show that the number of en passant synapses is the same in the *Bax* mutant
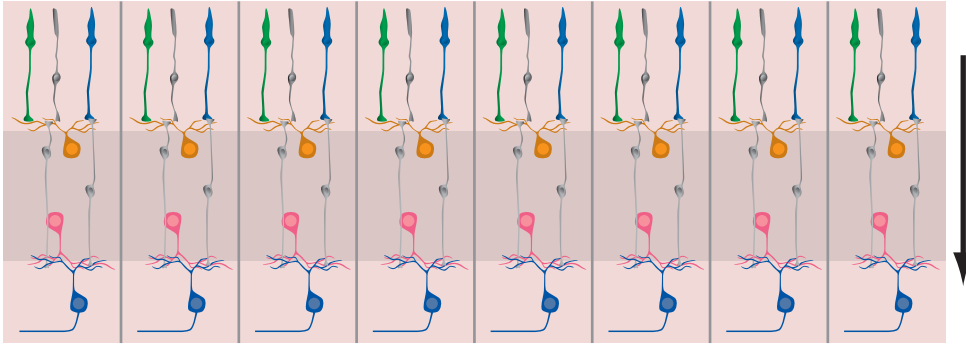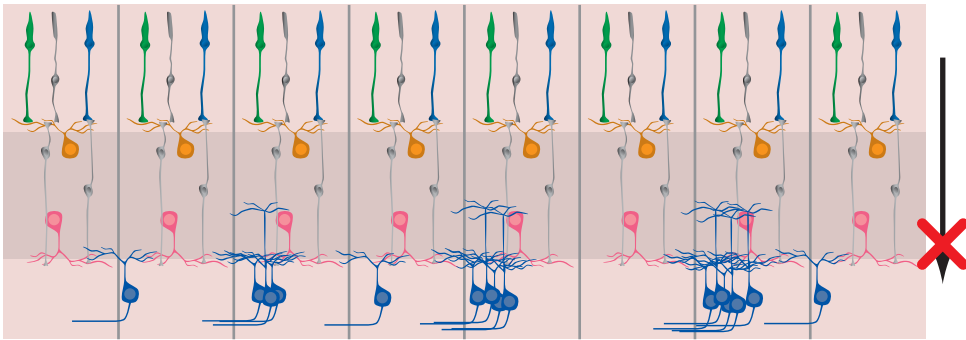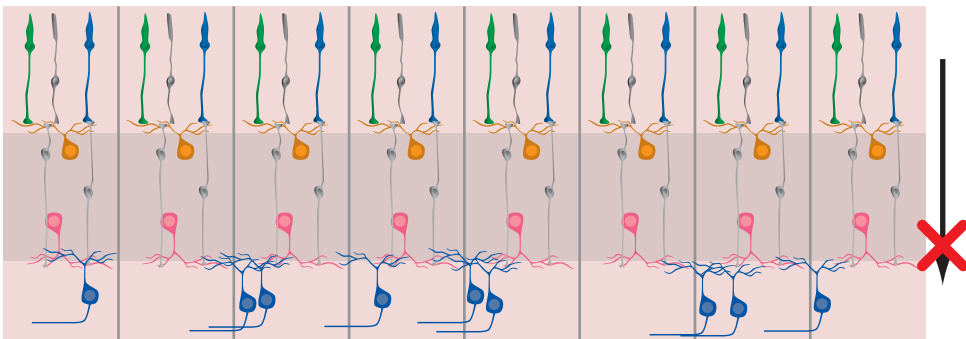
Figure 16. Model suggesting why disrupted mosaic patterning affects circadian light functions
The spacing of cells in retinal mosaics ensures a uniform processing across the visual field. Abnormal somal positioning in the Bax KO (which also have dendritic fasciculation) and conditional Bax KO retinas is proposed to disrupt rod-cone input to ipRGCs that mediate circadian photoentrainment. Both Bax and conditional Bax mutants that contain the melanopsin protein exhibit normal signaling from ipRGCs to the brain for photoentrainment of the circadian clock. In addition, the circadian oscillator is unaffected in both genotypes. Therefore, the photoentrainment deficits in both Bax and conditional Bax mutants that also lack the melanopsin protein are due to defects in synaptic signaling between the inner nuclear layer and the M1 ipRGCs (see Figure 13 and 15).

mice where the number of ipRGCs is significantly increased (Figure 13C). As a consequence, disrupting ipRGC normal spacing may disrupt the uniformity of their coverage, potentially leaving regions devoid of M1 processes altogether, especially in light of the constant number of en passant synapses.

Bax mutant retinas also show abnormal fasciculation of their processes that should further exacerbate this tendency. Additionally, *Bax* mutant retinas show conspicuous alterations in the radial organization of the retinal synaptic architecture associated with the positioning of M1 ipRGC dendrites. These dendrites receive both increased ectopic ON input within the INL and co-fasiculate with dopaminergic amacrine cells, which are also GABAergic (Contini and Raviola, 2003; Hirasawa et al., 2009). These increased ectopic synapses within the INL may lead to more inhibition of ipRGCs due to GABA release from light-activated dopaminergic amacrine cells, reducing the strength of rod/cone input to ipRGCs, which is consistent with the deficits we observed in rod-cone signaling to ipRGCs as measured by cFos activation and electrophysiological recordings (Figure 13 and 15).

It is important to note that the number of ipRGCs does not increase in the conditional *Bax* mutants. This is likely due to the late developmental expression of melanopsin protein (and thus also Cre recombinase in *Opn4^{Cre}* animals) in ipRGCs, in relation to the timing of peak apoptosis (P2-P4) in RGCs. Melanopsin expression is first observed at E15 and only peaks by P3. Thus, the overlap between melanopsin-driven Cre expression and the timing of normal RGC apoptosis could result in inefficient deletion of *Bax* at the critical developmental period. Two testable predictions follow this hypothesis. First, in the conditional *Bax* mutants (*Opn4$^{Cre/+}$; Bax$^{fl/fl}$*), residual Bax expression in ipRGCs should still be observed at early postnatal stages. Indeed Bax antibody staining revealed residual expression in some ipRGCs (Figure 10A), in support of the

first prediction. Second, using a transgenic line where Cre is expressed earlier in ipRGCs for *Bax* deletion in relation to apoptosis, we show better recapitulation of the *Bax$^{-/-}$* phenotype. Using *Math5*, which is expressed in RGCs from E11-E14 (Yang et al., 2003), to drive Cre in conjunction with the floxed *Bax* allele (*Math5$^{Cre/+}$; Bax$^{fl/fl}$*), we found higher ipRGC numbers with fasciculated dendrites similar to the phenotypes seen in the conventional *Bax* mutants (Figure 10B). Together, these results provide strong evidence that the lack of increased cell numbers in *Opn4$^{Cre/+}$; Bax$^{fl/fl}$* animals stems from the inefficiency of recombination at the *Bax* locus during the appropriate developmental stages. A key question that arises from our findings is why ipRGCs in the conditional *Bax* mutant still show disrupted spacing despite inefficient *Bax* deletion. The proximity-based model of how apoptosis contributes to the spaced distribution should account for this disruption: In wild type animals, ipRGCs in close proximity undergo apoptosis, possibly by competing for limited levels of survival factors that originate in the retina and/or brain targets. In the conventional *Bax* knockout, all cells lack Bax and hence ipRGCs survive leading to higher cell numbers in a clumped distribution. In the conditional *Bax* animals, where there is stochastic *Bax* deletion, some ipRGCs that still retain Bax expression will be in close proximity to Bax deleted ipRGCs. This scenario will give the Bax negative ipRGCs a competitive advantage over the Bax positive ipRGCs irrespective of the survival signal. This scenario will give the Bax negative ipRGCs a competitive advantage over the Bax positive ipRGCs, biasing the ipRGC survival to those that lack Bax expression including some in close proximity, thereby disrupting the regular spacing of ipRGCs in the *Opn4$^{Cre/+}$; Bax$^{fl/fl}$* animals.

The majority of studies indicate that homotypic interactions underlie the formation of regular retinal mosaics. During the peak period of cell death at early postnatal stages, it is difficult to distinguish between the ipRGC subtypes, mainly due to the incomplete establishment

of full dendritic fields. All ipRGCs express melanopsin and there are no other known markers that currently differentiate between individual subtypes. ipRGCs subtypes (M1 versus non-M1) can only be easily distinguished morphologically in adult mice by their mature dendritic fields. In our identification of apoptotic ipRGCs at P4, a caveat is that we were unable to differentiate the specific ipRGC subtypes. Thus, we cannot be certain that cells undergoing apoptosis near other ipRGCs are of the same subtype.

Interestingly, some of the phenotypes that we report here in the conventional *Bax* mutants, fasciculated ipRGC dendrites, disrupted mosaic spacing and increased ipRGC cell number have also been reported in mice lacking Dscam, a neuronal cell adhesion molecule (Fuerst et al., 2009; Fuerst et al., 2008). These results suggest the intriguing possibility that crosstalk between Bax and Dscam regulates proper ipRGC cell number, spacing and dendritic architecture (Keeley et al., 2012). It is also important to note that although we have assumed that the deficits observed in the *Bax* mutants are only apoptosis-dependent, several recent studies indicate that Bax could have roles independent of apoptosis (Autret and Martin, 2009; Jiao and Li, 2011; Jonas et al., 2005). Thus, it is feasible that some of the deficits that we observe in *Bax* mutants might also reflect a role for Bax in mitochondrial morphogenesis (Autret and Martin, 2009) or changes in synaptic activity (Jiao and Li, 2011; Jonas et al., 2005).

In summary, we show that *Bax*-mutant mice exhibit conspicuous changes in the organization of the M1 ipRGC mosaic. Remarkably, none of the morphological deficits affect the intrinsic light sensitivity and transmission from the retina to the brain to control photoentrainment. This is despite the widespread assumption that a uniformly distributed network of ipRGC processes is critical for the light-gathering properties of M1 ipRGCs

(Provencio et al., 2002). Indeed, for circadian photoentrainment, one might have expected the M1 population of ipRGCs to lack the properties of other regular retinal mosaics, including uniformity of their dendritic coverage across the retina, because they were originally thought to be only ambient light-sensors. With the demonstration that ipRGCs also receive direct input from ON bipolar cells relaying rod-cone input (Dumitrescu et al., 2009; Hoshi et al., 2009), it might be expected, therefore, that ipRGCs form regular mosaics similar to other RGC types, as recently demonstrated (Berson et al., 2010). Indeed, our study demonstrates a functional relevance for the M1 ipRGC mosaic in that it is crucial for the normal reception of rod-cone input to drive photoentrainment.

METHODS

Mice

     All mice were of a mixed background (C57BL/6;129SvJ), except those in figure 1A and B (being congenic with C57BL/6J). Animals that were used in the behavioral analyses were between 4 and 12 months. Animals were housed and treated in accordance with NIH and IACUC guidelines, and all animal care and use protocols were approved by the Johns Hopkins University Animal Care and Use Committee. The *Math5^{cre}* mice were a generous gift of Lin Gan. Because the cDKO and cKO lines were derived from a *Bax$^{fl/fl}$;Bak$^{-/-}$* line purchased from the Jackson Laboratory (originally generated by Stanley Korsmeyer's laboratory (Takeuchi et al., 2005)), 4 out of 9 cDKO, 3 out of 7 control, and 1 out of 5 cKO mice were heterozygous for *Bak* (*Bak$^{+/-}$*) in the wheel-running activity experiments. Within each group, *Ba*k$^{+/-}$ mice behaved no differently from *Bak$^{+/+}$* mice.

Immunohistochemistry

     For labeling dying cells, eyes were fixed 30 minutes in 4% paraformaldehyde, retinas were dissected then blocked for 2 hours in 5% goat serum, 2% donkey serum, and 0.3% Triton in 0.1M PBS. Retinas than incubated with mouse monoclonal anti-activated Bax (1:500, 6A7 gift from Richard Youle), rabbit polyclonal anti-cleaved caspase 3 (1:200, Cell signaling) and sheep polyclonal anti-GFP (1:500, Biogenesis) for 2 days at 4°C. Retinas were washed three time in 0.1M PBS and than incubated with 1:800 Alexa anti-rabbit-546, anti-mouse-546 and anti-sheep-488 in blocking solution for 2 hours. After secondary antibody incubation, retinas were washed three times in 0.1M PBS and incubated with TUNEL reaction mixture at 37°C for 1 hour

according to manufacturer's instructions (*in situ* cell detection kit TMR red, Roche). Retinas were washed again three times in 0.1M PBS and mounted with vectasheild.

For labeling inner retinal synapses, the retinas of adult $Bax^{-/-}$ and wildtype control mice were dissected following intracardial perfusion, and then either incubated in antibodies to melanopsin (a gift from Dr. Provencio), as described (Keeley et al., 2012), or they were sectioned on a vibratome and immunolabeled using antibodies to melanopsin, tyrosine hydroxylase (AB15542, Millipore) and either CtBP2 (612044, BD Transduction Laboratories) or Bassoon (VAM-PS003, Stressgen), as described (Keeley and Reese, 2010).

For labeling of ectopic synapses, retinas were dissected from whole eyes that had been fixed in 4% EM grade PFA for 20 minutes, cryoprotected in 30% sucrose and 12μm sections were taken using a cryostat. Sections were incubated in antibodies against γ13 (generously provided by Robert Margolskee) (1:500) and CtBP2 (612044, BD Transduction Laboratories)(1:250) overnight, washed, and incubated with Alexa-conjugated secondary antibodies (Invitrogen) for 3 hours.

For *cFos* staining, mice were house in LD 12:12 and dark adapted for 2 hours prior to exposure to light for 30 min at ZT 4. After the light treatment, mice were moved to dark conditions for 1 hour. The eyes were then removed, fixed in 4% PFA for 30 min, and dissected. Retinas were fixed for additional 2 hours, blocked in 0.1M phosphate buffer with 5% Goat serum and 0.3% Triton X-100, and then incubated with an anti-cFos antibody (Calbiochem Ab-5; 1:20,000) and an anti-beta-galactosidase antibody (Millipore; 1:2000) for 48 hours followed by incubation with Alexa-conjugated secondary antibodies (Invitrogen) for 2 hours.

Wheel-running activity

Wheel-running experiments were performed and analyzed similar to (Güler et al., 2008).

X-gal staining

Brains and retinas were prepared and stained similar to (Hattar et al., 2006).

Mosaic analysis

One image (895 X 671µm) was taken randomly from each of four quadrants per retina using a Zeiss microscope with Plan-Apochromat 10x/0.45 objective lens. Dots were manually placed over each individual cell body, the XY coordinates were extracted using imageJ, fed into WinDRP program (Masland Lab), and density recovery profile (DRP) graphs were generated with a 10µm bin size and a 10µm cell size. Data from the four fields were averaged for each retina, and each bin in the DRP shows the mean of those retinal averages (± SEM). This cell size was chosen since the cell body of an M1 ipRGC is approximately 10µm. The same XY coordinates were analyzed for their Voronoi tessellation of each field using specialty software to generate Voronoi domain regularity indexes (VDRI) and nearest neighbor regularity indexes (NNRI), as previously described [7] (Figure 9D and E). For all analyses, we averaged 4 fields per retina, and six retinas per condition, and this mean of the retinal averages (± SEM) is graphed. A similar procedure was carried out for the P0 DRP graphs and analysis of apoptosis at P4, except that we sampled a smaller area (322 X 322µm for P0 DRP graphs and 516 X 516µm for P4 staining) because at those developmental stages, the total retinal area is smaller. Additionally, for the analysis of apoptosis at P4, we took multiple images per quadrant to maximize our chances of analyzing apoptotic cells. Apoptotic cells that are on the periphery could not be included in our analysis. Thus, we found 77 apoptotic ipRGCs, but we were only able to analyze a fraction

of these cells (39 for Voronoi domain and 44 for nearest neighbor). Voronoi domain areas and nearest neighbor distances for apoptotic and non-apoptotic ipRGCs were calculated by imageJ and WinDRP, respectively.

In vitro preparation and electrophysiological recording

Mice of either sex and 8 – 12 months of age were used in these experiments. Animals were dark-adapted overnight and euthanized under dim red light with carbon dioxide. All subsequent tissue preparation procedures were performed under infrared illumination using night vision devices (NiteMate NAV-3, Litton Industries, Watertown, CT). Both eyes were harvested, hemisected, and incubated in room-temperature Ames' medium gassed with 95% O_2 5% CO_2. The retinas were isolated from the pigment epithelium and the vitreous removed from the retinas using forceps. Each retina was cut in half, and one piece was flattened on a 60-channel MEA (200/30-Ti-gr, Multi Channel Systems, Germany) with the ganglion cell side down; the other half was discarded. The retina was continuously superfused at 3 mL min-1 with Ames' medium gassed with 95% O_2 5% CO_2 and maintained at 33°C with a temperature controller (Warner Instruments, Hamden, CT), and was kept in darkness except when stimulated by light. Presentation of light stimuli started after the retina had been superfused for 40 min. All stimuli were 10-second full-field 480-nm light generated by a monochromator (Optical Building Blocks, Birmingham, NJ). The timing of stimulus presentation was controlled by an electromechanical shutter built into this monochromator. Light intensity was adjusted by a continuously variable neutral density filter (Newport Corporation, Franklin, MA). The intensity-adjusted light was delivered via a fiber optic cable to the retina from underneath the MEA chamber. Light intensities were calibrated using a radiometer (UDT Instruments, San Diego, CA) and the

unattenuated intensity (i.e. -0 log I) was 4.1×10^{15} quanta cm-2 s-1 at the retina. At the end of each experiment, a pharmacological cocktail containing 50 – 100 µM L-(+)-2-Amino-4-phosphonobutyric acid (L-AP4), 40 – 80 µM 6,7-Dinitroquinoxaline-2,3-dione (DNQX), and 25 µM D-(-)-2-Amino-5-phosphonopentanoic acid (D-AP5) was applied to block rod/cone signaling to the inner retina, and ipRGCs were identified based on their ability to generate sluggish, melanopsin-based responses to -0 log I light. This cocktail completely abolished the light responses of all conventional ganglion cells.

Ganglion cell spiking activity was amplified, filtered with cutoffs at 200 Hz and 3 kHz, and digitized at 10 kHz using MC Rack software (Multi Channel Systems). Raw recordings from all 60 channels were saved onto a computer for offline analysis. Cluster analysis of the spike data was performed using Offline Sorter software (Plexon Inc., Dallas, TX). For Fig. 5D and E, photoresponse amplitude was calculated by subtracting the mean firing rate during the 10-sec period preceding stimulus onset from that during the 10-sec light stimulus. Student t-test p-values were calculated using Origin software (OriginLab, Northampton, MA), with the significance level set at 0.05.

Electroretinograms

The sensitivity of light-evoked signals from photoreceptors and bipolar cells was assessed in electroretinogram (ERG) recordings from whole-mount retina. ERGs were used to record the rod-driven a-wave and the bipolar cell-driven b-wave from isolated retinas, similar to procedures described in (Wang et al., 2009). Briefly, a piece of dark-adapted retina was mounted photoreceptor side-up over a machined 1 mm hole in a Plexiglass recording chamber, and was gently flattened using forceps. A slice anchor was used to hold the retina flat, and the tissue was

superfused in darkness at a rate of 5 ml/min with 35-37°C Ames' media buffered with sodium bicarbonate and equilibrated with 5% CO_2/ 95% O_2 resulting in pH ~ 7.4. The trans-retinal potential change to flashes of light was measured using Ag/AgCl half-cells with a differential amplifier (Model DP-311; Warner Instruments), and was sampled at 10 kHz and low-pass filtered at 300 Hz. Further 30 Hz digital low-pass filtering was done offline in Matlab. 520 nm flashes of light (30 ms) were delivered from a traditional light bench as described previously (Miyagishima et al., 2009). Full ERGs were measured by superfusing the retina with Ames' media, and A-waves were further isolated as 12 mM APB was added. On (rod) bipolar mediated B-waves were calculated by subtracting the APB-isolated A-wave from the full ERG.

Visual Morris Water Maze

This test was carried out as described in (Ecker et al., 2010). Blind controls were enucleated mice.

Alkaline phosphatase staining and cell counting

AP staining was carried out as described in reference 9 in the main manuscript. For counting, the entire retina was imaged sequentially using a 10X objective. The resulting images were stitched together using Adobe Photoshop program. Dots were placed over individual cells and counted using imageJ.

Low magnification imaging of X-gal stained coronal brain sections

X-gal staining was performed according to the protocol described in the main text. Images were taken using a dissecting microscope with a 1X objective.

Math5$^{Cre/+}$; Bax$^{fl/-}$ density analysis

One image (895 X 671µm) was taken randomly from each of four quadrants per retina using a Zeiss microscope with Plan-Apochromat 10x/0.45 objective lens. Dots were manually placed over individual cell body and counted using imageJ. We averaged 4 fields per retina and this average is graphed.

CHAPTER 3: IPRGCS REGULATE THE DEVELOPMENT OF BOTH THE IMAGE AND NON-IMAGE FORMING VISUAL SYSTEMS

A portion of this chapter as been submitted for publication at Science

Chew K.S.*, Renna J.M.*, l D.S., Ecker J.L., Loevinsohn G.S., Van Dunk C., Weng S., Gray P., Herzog E., Zhao H., Berson D.M., Hattar S. M1 ipRGCs regulate the development of the circadian clock and vision. Science.

<u>INTRODUCTION</u>

Light detected by the mammalian eye is used for the conscious perception of images, tracking of objects, and the synchronization of circadian rhythms to the solar day. These diverse visual functions, both image- and non-image-forming, require the retina for the detection and the initial processing of light signals, which are then relayed to the brain via the output neurons of the eye, retinal ganglion cells (RGCs). The majority of RGCs project to image-forming centers in the brain, such as the dorsal lateral geniculate nucleus (dLGN) and the superior colliculus (SC). A subset of RGCs, however, is intrinsically photosensitive (Berson, 2003; Berson et al., 2002; Hattar et al., 2002; Provencio et al., 1998), in addition to receiving indirect light signals from the classical photoreceptors, rods and cones (Lucas et al., 2003; Mrosovsky and Hattar, 2003; Panda et al., 2002; Ruby et al., 2002; Schmidt et al., 2008). These intrinsically photosensitive RGCs (ipRGCs) constitute the sole conduit of light information to non-image-forming centers in the brain, such as the suprachiasmatic nucleus (SCN) (Güler et al., 2008; Hattar et al., 2003; Panda et al., 2003). ipRGCs drive non-image-forming behaviors even in the absence of rods and cones (Czeisler et al., 1995; Foster et al., 1991; Freedman et al., 1999; Lucas et al., 2001; Lucas et al., 1999). Early reports envisioned a strict separation between the image- and non-image-forming visual networks (Dreher and Robinson, 1991; Moore, 1997; Young and Lund, 1994), but this view has begun to be challenged by recent evidence for functional crosstalk between the two systems (Ecker et al., 2010; Estevez et al., 2012; Renna et al., 2011; Zhang et al., 2008a).

During development, all RGCs must achieve precise central connections in the brain that are necessary for the generation of visual behaviors. Precise visual circuits emerge in a multistep process: preset genetic programs establish a coarse level of organization, which

are then refined in an activity-dependent manner. The image-forming visual system has been the classic model of activity dependent refinement of neuronal circuits (Meister et al., 1991; Shatz and Stryker, 1988). Refinement of the coarse projections of the RGCs to the brain is dependent on spontaneously generated neural activity, termed retinal waves. These retinal waves, with defined properties, sweep across the retina to instruct the production of an accurate map of the visual world, known as the retinotopic map (Ackman et al., 2012; Chandrasekaran et al., 2005; Feller, 2002, 2009; Firth et al., 2005; McLaughlin et al., 2003a; Meister et al., 1991; Mrsic-Flogel et al., 2005; Muir-Robinson et al., 2002; Shatz and Stryker, 1988; Stellwagen and Shatz, 2002; Wong, 1999; Xu et al., 2011; Zhang et al., 2011). Interestingly, light detection through ipRGCs influences retinal waves (Renna et al., 2011; Sekaran et al., 2005) and ipRGCs depolarize during retinal waves similar to other conventional RGCs. However, it has not been determined whether the developmental roles of ipRGCs have permanent functional consequences for the image-forming visual system.

ipRGCs, however, are best known for their ability to synchronize the circadian clock in the suprachiasmatic nucleus (SCN) to the solar cycle (Chen et al., 2011; Güler et al., 2008), a process known as circadian photoentrainment. The circadian clock contains an intrinsic genetic program that, in the absence of environmental light input, produces molecular and physiological rhythms with periods close to, but not exactly, 24 hours (Harmer et al., 2001; Menaker et al., 1978). Due to the autonomous nature of the circadian clock, the prevailing view has been that the fundamental features of the clock in the SCN, such as period length, do not require environmental input for maturation (Davis and Menaker, 1981; Davis and Gorski, 1985; Jud and Albrecht, 2006; Pittendrigh, 1954; Richter, 1971; Vallone et al., 2007; Yamazaki et al., 2002). However, there is intriguing evidence

that animals that do not form eyes or the optic nerve due to genetic defects exhibit a lengthened circadian period (Laemle and Ottenweller, 1998; Wee et al., 2002). Since ipRGCs are the major, if not the sole, source of retinal input to the SCN (Baver et al., 2008; Berson, 2003; Hattar et al., 2006; Hattar et al., 2002), these observations implicate a possible role for ipRGCs in the maturation of the circadian clock.

ipRGCs have now been shown to also project to the image-forming visual system (Ecker et al., 2010). These projections appear to arise from subtypes of ipRGCs that are morphologically and physiologically distinct from the originally identified ipRGCs, which are now known as M1 ipRGCs (Ecker et al., 2010; Schmidt et al., 2011; Schmidt and Kofuji, 2009; Schmidt et al., 2008). M1 ipRGCs innervate non-image-forming centers and are molecularly defined based on the expression of a transcription factor, *Brn3b* (Chen et al., 2011). The non-M1 ipRGC subtypes (M2-M5) send their axons to the dLGN and SC and are capable of supporting coarse pattern vision in animals lacking functional rod and cone phototransduction pathways (Brown et al., 2010; Ecker et al., 2010). Given the diversity of ipRGCs, especially in projection patterns, the expectation is that each subtype has a distinct function.

To investigate the role of ipRGCs in the development of the image- and non-image-forming visual systems, we ablated ipRGCs at early postnatal stages in mice. In the circadian system, early postnatal ablation of ipRGCs lengthened the period of the circadian clock. Strikingly, dark rearing wild type (WT) animals from birth also lengthened the period of the circadian clock, and exposing these animals to light in adulthood restored a normal circadian period. These findings demonstrate that, contrary to the prevailing view that the circadian clock develops autonomously, intrinsic properties of the circadian clock

require light input from ipRGCs. In the image-forming visual system, we found that developmental ablation of ipRGCs also altered retinal waves, changed the axonal segregation of the dLGN from the two eyes and caused reduction in visual acuity. These results indicate that ipRGCs influence the development of both the circadian clock and the image-forming visual circuits. Given there are several subtypes of ipRGCs that differentially innervate image versus non-image centers, it was highly unexpected to find that a single small subpopulation of ipRGCs — the 200 M1 cells that only project to circadian centers (Chen et al., 2011) — are sufficient for supporting the developmental refinement of both the circadian clock and the image-forming visual system.

RESULTS

Genetic ablation of ipRGCs during early postnatal stages

To examine the contributions of ipRGCs to visual development, we ablated these cells at an early postnatal age (Figure 17, 18; Table 2). We previously found that replacing the melanopsin (*Opn4*) coding region with a sequence encoding an attenuated form of Diphtheria toxin A subunit (aDTA; a translational inhibitor; *Opn4$^{aDTA/+}$*) does not begin killing ipRGCs until adulthood (Güler et al., 2008). Therefore, we inserted the full-strength form of this toxin (DTA) into the same genomic locus as that of aDTA (Figure 18A, B). To determine the efficacy of full-strength DTA in ablating ipRGCs, we used the melanopsin-Cre line with the alkaline phosphatase (AP) reporter line (*Opn4$^{Cre/+}$*; *Z/AP*) to label all ipRGCs subtypes with AP (Ecker et al., 2010). As expected from our previous publication showing loss of ipRGCs only in adults, expressing the aDTA toxin from the melanopsin locus results in comparable numbers of ipRGCs, labeled by AP, in *Opn4$^{Cre/aDTA}$; Z/AP* (2230 ± 409 cells)

Table 2: Mouse lines used in Chapter 3

Mouse Lines	M1 ipRGCs	Non-M1 ipRGCs	Circadian behavior	Eye-specific axonal segregation and visual acuity
$Opn4^{Cre/+}$	Express Cre	Express Cre	Normal circadian photoentrainment	Normal eye-specific axonal segregation and visual acuity
$Opn4^{Cre/+};$ Z/AP	Labeled with AP	Labeled with AP	Normal circadian photoentrainment	Normal eye-specific axonal segregation and visual acuity
$Opn4^{LacZ/LacZ}$ (MKO)	Lack the melanopsin protein; labeled with x-gal	Lack the melanopsin protein	Normal circadian photoentrainment; small deficits in phase shifting	Normal eye-specific axonal segregation and visual acuity
$Opn4^{aDTA/aDTA}$	Ablated during adulthood; lack melanopsin	Persist but lack melanopsin	Do not photoentrain and free run with a normal circadian period	Normal eye-specific axonal segregation and visual acuity
$Opn4^{Cre/aDTA};$ Z/AP	Many ablated during adulthood; lack melanopsin; labeled with AP	Persist but lack melanopsin; labeled with AP		
$Opn4^{DTA/+}$	All but ~75 are ablated by P14	Many are ablated by P14	Normal circadian photoentrainment	Intermediate deficits in eye-specific axonal segregation and visual acuity
$Opn4^{DTA/LacZ}$	All but ~75 are ablated by P14; remaining cells lack melanopsin; labeled with x-gal	Many are ablated by P14; remaining cells lack melanopsin	Highly disrupted photoentrainment	
$Opn4^{Cre/DTA};$ Z/AP	All but ~75 are ablated by P14; remaining cells lack melanopsin; labeled with AP	Many are ablated by P14; remaining cells lack melanopsin; labeled with AP		
$Opn4^{DTA/DTA}$	Ablated during postnatal development	Cannot be determined for sure, but many, if not all, are ablated during postnatal development; remaining cells lack melanopsin	Do not photoentrain and free run with a lengthen circadian period	Severe deficits in eye-specific axonal segregation and visual acuity
$Opn4^{Cre/+};$ $Brn3b^{DTA/+}$	All but ~200 ablated by P7	Ablated by P7	Normal circadian photoentrainment	Normal eye-specific axonal segregation and visual acuity
$Opn4^{Cre/+};$ $Brn3b^{DTA/+};$ Z/AP	All but ~200 ablated by P7; labeled with AP	Ablated by P7; labeled with AP		
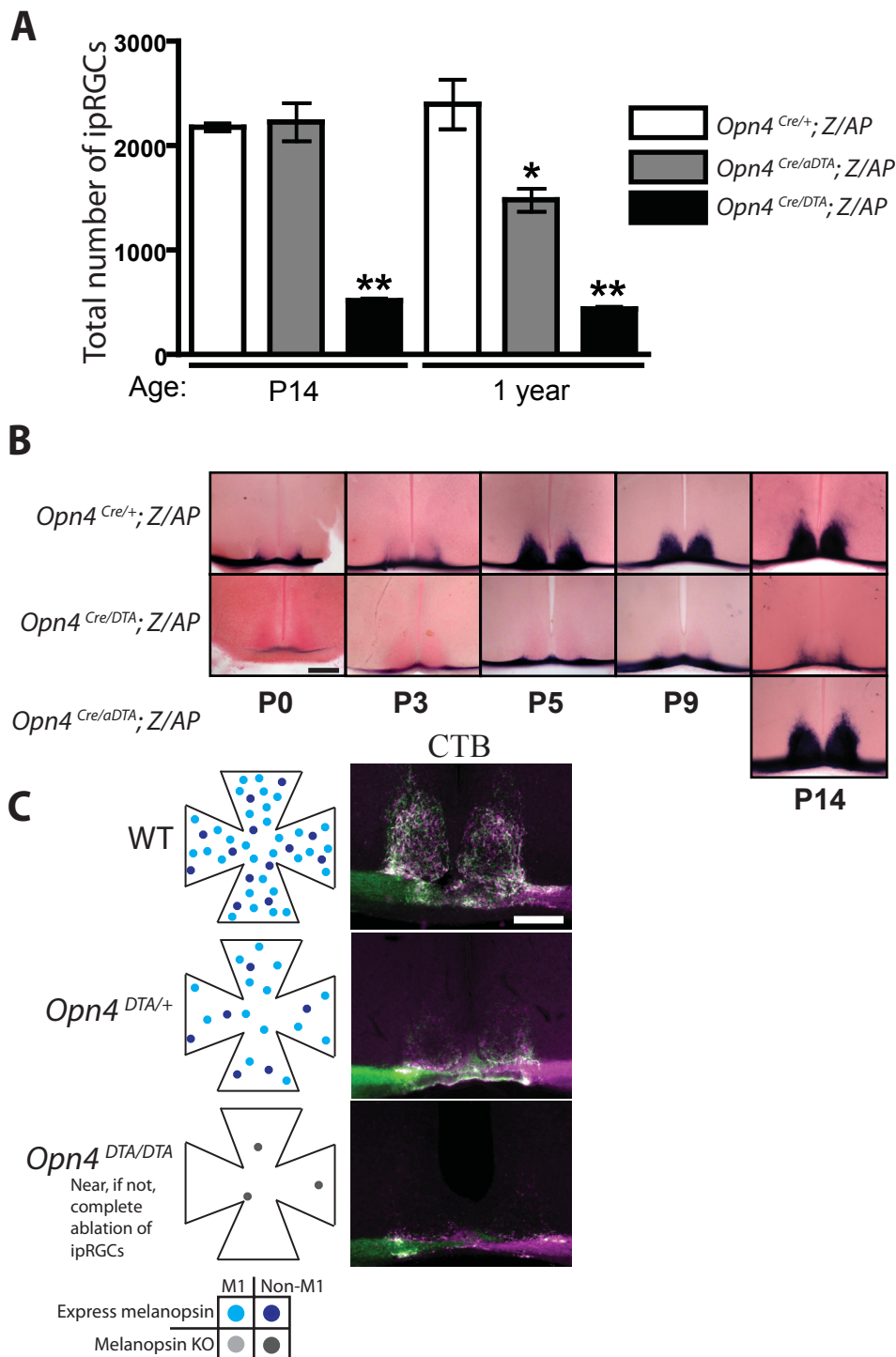
Figure 17. Developmental ablation of ipRGCs in the mouse retina

A. Cell counts of the total number of ipRGCs stained with AP at P14 and 1 year of age from three mouse lines: Opn4^Cre/+; Z/AP (control), Opn4^Cre/aDTA; Z/AP, and Opn4^Cre/DTA; Z/AP. * indicates P<0.01 and ** indicates P<0.001 by one-way ANOVA with Tukey post-hoc analysis. Error bars represent s.e.m.

B. Developmental time course of ipRGC innervation of the SCN, visualized by AP staining, in Opn4Cre/+; Z/AP and Opn4^Cre/DTA; Z/AP mouse. For comparison, SCN staining from Opn4^Cre/aDTA; Z/AP mice at P14 are also shown. Scale bar = 200 μm.

C. Total retinal innervation of the SCN, visualized by retinal injection of fluorescently conjugated cholera toxin in WT, Opn4^DTA/+, and Opn4^DTA/DTA mice. Scale bar = 200 μm.
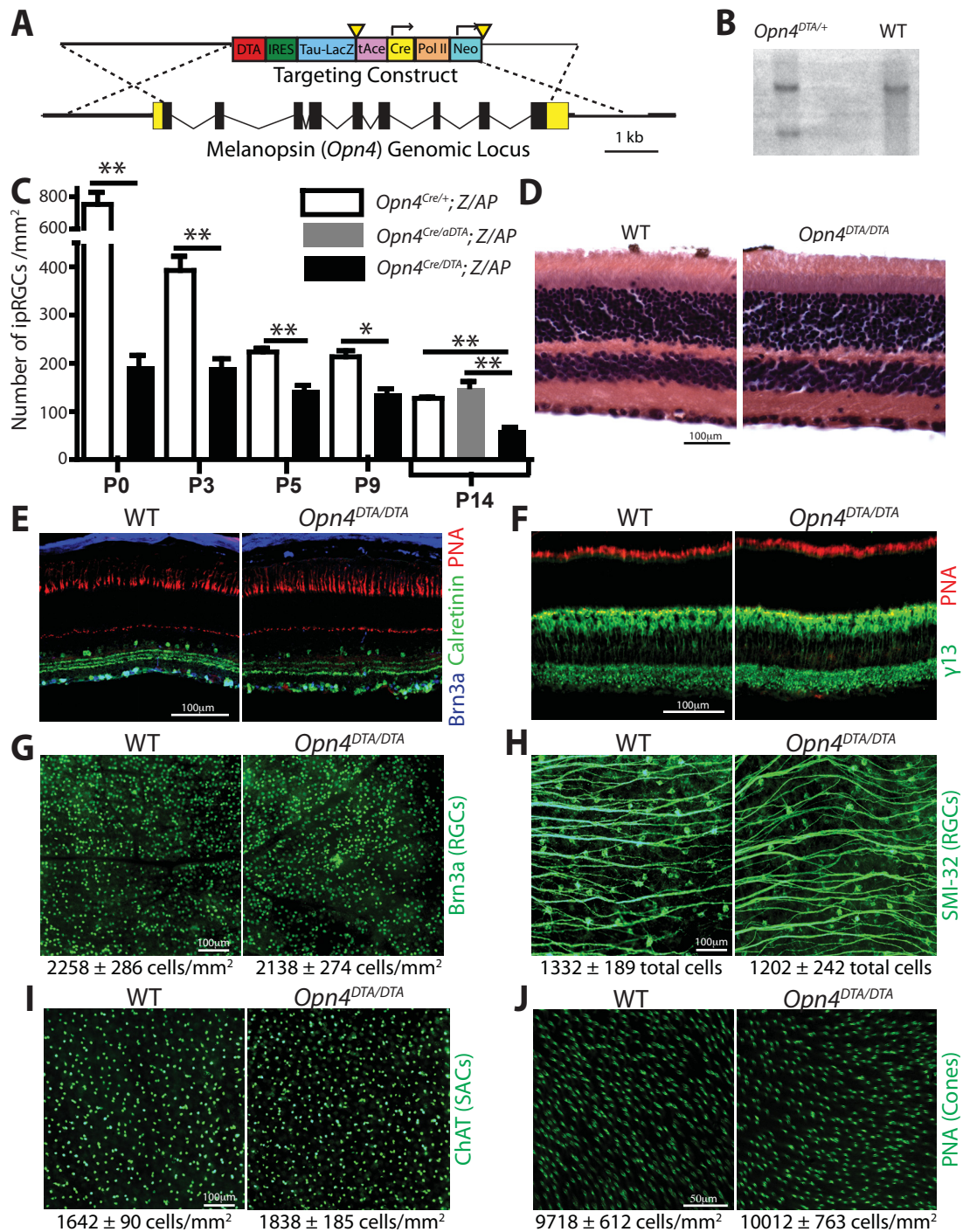
Figure 18: Generation and characterization of mice with an Opn4[DTA] allele

A. Targeting construct for inserting the coding sequence of DTA into the melanopsin (Opn4) locus.

B. Southern blot analysis confirming homologous recombination of the targeting construct at Opn4 locus in ES cells.

C. Developmental time course of ipRGC cell density in Opn4[Cre/+] Z/AP (control) and Opn4[Cre/DTA]; Z/AP mice at P0, P3, P5, P9, and P14. Cell counts from P14 retinas of Opn4[Cre/aDTA]; Z/AP mice are also shown for comparison. * indicates $P<0.01$ and ** indicates $P<0.001$ with a one-way ANOVA with Tukey post-hoc analysis. Error bars represent s.e.m. D. Hematoxylin and eosin staining on retinal sections from WT and Opn4[DTA/DTA] mice. E. Staining with fluorescently conjugated peanut agglutinin to label cones (red), and immunohistochemistry for caleretinin positive amacrine and ganglion cells (green), and Brn3a positive ganglion cells (Blue) on retinal sections from WT and Opn4[DTA/DTA] mice. Scale bar = 100μm. F. Staining with fluorescently conjugated peanut agglutinin to label cones (red) and immunohistochemistry for γ-13 to label ON-bipolar cells (green) on retinal sections from WT and Opn4[DTA/DTA] mice. Scale bar = 100μm. G. Density of Brn3a positive RGCs, identified by immunohistochemistry for Brn3a. Scale bar = 100μm. H. Total number of alpha-like RGCs, identified by immunohistochemistry for SMI-32. Scale bar = 100μm. I. Density of starburst amacrine cells, identified by immunohistochemistry for ChAT. Scale bar = 100μm. J. Density of cones, identified by staining with fluorescently conjugated peanut agglutinin. Scale bar = 50μm.

and control mice (*Opn4^{Cre/+}; Z/AP,* 2180 ± 86 cells) at P14. The number of ipRGCs however, declined to 1482 ± 189 cells at one year of age in the presence of the aDTA toxin. In contrast, ipRGC counts across postnatal development in the presence of full-strength DTA (*Opn4^{Cre/DTA}; Z/AP)* showed a significant reduction of ipRGC number by postnatal day 0 (P0) (Figure 18C). By P14, the number of ipRGCs decreased to 518 ± 67 in mice expressing the full-strength DTA, which is comparable to the number of ipRGCs observed at one year of age (*Opn4^{Cre/+}; Z/AP*, 2399 ± 474 cells vs. *Opn4^{Cre/DTA}; Z/AP*, 435 ± 41 cells; Figure 17A). We performed a number of controls to determine that expression of DTA from the melanopsin locus only results in ablation of ipRGCs and has no effects on other cells types. Specifically, we examined gross retinal morphology, the integrity of ON Bipolar cells, the banding pattern of Calretinin, the numbers of cone photoreceptors, starburst amacrine cells and both Brn3a-positive and alpha-like ganglion cells (Figure 18D-J). All these results showed no significant difference between WT and *Opn4^{DTA/DTA}* mice and we provide a complete description of these experiments in supplemental text (section 1.1). Thus, DTA efficiently and specifically ablates ipRGCs even at early postnatal ages, and this mouse model can serve as a tool to study the contributions of ipRGCs to development of the image-forming and non-image-forming visual systems.

Given the profound reduction in ipRGC number in full-strength DTA mice over the first two postnatal weeks (Figure 17A, 18C), we expected a substantial loss of retinal input to the SCN, which derives exclusively from ipRGCs (Baver et al., 2008; Güler et al., 2008; Sollars et al., 2003). To assess ipRGC target innervation during postnatal stages, we used the AP reporter line to trace ipRGC axons to the brain in control (*Opn4^{Cre/+}; Z/AP) aDTA (Opn4^{Cre/aDTA}; Z/AP*) *and DTA (Opn4^{Cre/DTA}; Z/AP)* mice (Table 2). In the presence of the DTA

(*Opn4Cre/DTA; Z/AP)* mice, a severe loss of ipRGC innervation of the SCN was apparent as early as P0 (Figure 17B). At P14, the SCN receives strong innervation from ipRGCs in control and *Opn4Cre/aDTA; Z/AP* animals, but was devoid of ipRGC input in *Opn4Cre/DTA; Z/AP* mice except for a small zone of sparse innervation at the lateral edges (Figure 17B).

The necessity of Cre recombinase to label all ipRGCs (*Opn4Cre/+; Z/AP*) for the quantification of cell loss only allowed for the presence of one copy of DTA at the melanopsin locus. To assess the extent of ipRGC ablation in mice homozygous for DTA (*Opn4DTA/DTA*), we labeled all retinal projections at P60 with a bilateral intraocular injection of cholera toxin B subunit (CTB), a fluorescent anterograde tracer, and compared the resulting labeling in the SCN of wild type (WT), heterozygous (*Opn4DTA/+*), and homozygous DTA (*Opn4DTA/DTA*) mice (Figure 17C). The SCN contained only a few fibers in *Opn4DTA/+* mice (Figure 17C), paralleling the results obtained with *Opn4Cre/DTA; Z/AP* mice (Figure 17B). Even this sparse labeling was abolished in *Opn4DTA/DTA* mice (Figure 17C), demonstrating that two alleles of DTA resulted in a more thorough ablation of ipRGCs (Table 2). Furthermore, these data also demonstrated that depriving the SCN of its normal ipRGC input early in development did not induce compensatory innervation by conventional RGC afferents.

Expression of DTA from the melanopsin locus exclusively ablates ipRGCs without non-specific effects on other retinal cell types.

Previously, we have shown that some cones are labeled using the *Opn4-Cre* line (*Opn4Cre/+; Z/AP*) animals (Ecker et al., 2010). To determine whether the Cre-independent DTA-mediated killing in *Opn4DTA/DTA* mice was specific to ipRGCs, we measured the density

of cone photoreceptors by using peanut agglutinin staining. The density of cones was not significantly different between $Opn4^{DTA/DTA}$ (10,012 ± 763 cells/mm^2) and WT (9718 ± 611 cells/mm^2, Figure 18J) mice. These results indicate that DTA driven directly by the melanopsin promoter does not kill cone photoreceptors in the retina.

We then wanted to investigate whether conventional RGCs are intact in the $Opn4^{DTA/DTA}$ mice. We used two markers that label distinct populations of conventional RGCs. Brn3a is a marker for ~80% of conventional RGCs and it does not colocalize with melanopsin (Jain et al., 2012; Quina et al., 2005) and SMI-32 which labels alpha-like RGCs (Coombs et al., 2006). Both RGC labeling methods showed no significant difference in the density (WT; 2258 ± 286 Brn3a positive cells/mm^2 and $Opn4^{DTA/DTA}$; 2138 ± 273 Brn3a positive cells/mm^2, Figure 18G) or numbers (WT; 1332 ± 189 SMI-32 positive cells and $Opn4^{DTA/DTA}$; SMI-32 positive 1202 ± 242 cells, Figure 18H) of RGCs in $Opn4^{DTA/DTA}$ and WT mice. These data show that the DTA line specifically kills the majority of ipRGCs with no effect on conventional RGCs.

We then went further to show that the gross morphology of the retina as well as the number of ChAT-positive amacrine cells, which are important for retinal waves, are intact in the $Opn4^{DTA/DTA}$ mice. We used two independent labeling methods to examine the gross morphology of the retina. First, using hematoxylin and eosin staining on retinal sections from WT and $Opn4^{DTA/DTA}$ mice, we found no apparent differences in the overall histology between the two genotypes (Figure 18D). Second, using immunohistochemistry, we show that both the inner nuclear layer, using a marker for ON Bipolar cell, and the calretinin banding pattern are normal in $Opn4^{DTA/DTA}$ mice (Figure 18E, F). These two methods reveal that the gross morphology of the retina is not affected in the $Opn4^{DTA/DTA}$ mice. Finally,

using ChAT staining, which labels Starburst amacrine cells, we show that the density of

ChAT positive amacrine cells was similar between WT (1642 ± 90 cells/mm^2) and

Opn4$^{DTA/DTA}$ mice (1838 ± 185 cells/mm^2, Figure 18I). Collectively, these data indicate that

use of a strong DTA toxin in *Opn4$^{DTA/DTA}$* animals leads to cell killing that is exclusive to

ipRGCs, with no non-specific effects on general retinal morphology or on cell types that do

not express melanopsin.

ipRGCs are necessary for setting the intrinsic period of the circadian clock

Now that we established the specificity of ipRGC ablation in *Opn4^{DTA}* line and given

the well-established role for ipRGCs in photoentrainment, we asked whether ipRGCs might

also play a role in the development of the circadian clock. Previously, when ipRGCs were

selectively ablated in adulthood (*Opn4$^{aDTA/aDTA}$*), mice exhibited normal intrinsic circadian

period but failed to photoentrain (Güler et al., 2008). In this study we use the full strength

DTA to determine the effects on the circadian period. We utilize three lines which express

the DTA allele: *Opn4$^{DTA/+}$* line, which maintains melanopsin expression in any surviving

ipRGCs, as well as *Opn4$^{DTA/LacZ}$* and *Opn4$^{DTA/DTA}$* lines, which both lack the melanopsin

protein but contain either a single or two copies of DTA. As controls, we used WT,

melanopsin knockout (*Opn4$^{LacZ/LacZ}$*)(Hattar et al., 2002; Lucas et al., 2003) and

homozygous aDTA (*Opn4$^{aDTA/aDTA}$*) animals (Güler et al., 2008) (Table 2).

We recorded wheel-running activity in 6-month old WT (n=8), *Opn4$^{LacZ/LacZ}$* (n=8),

Opn4$^{DTA/+}$ (n=8), *Opn4$^{DTA/LacZ}$* (n=7), *Opn4$^{aDTA/aDTA}$* (n=8), and *Opn4$^{DTA/DTA}$* (n=7) mice under

both 12:12 LD cycle and constant darkness (Table 2). We also administered a 15-minute

light pulse in constant darkness to determine the amplitude of the light-evoked circadian

phase shifts. As previously shown, control animals (WT and $Opn4^{LacZ/LacZ}$) photoentrained under the 12:12 LD cycle, and exhibited rhythmic activity under constant darkness with a free-running period of 23.7 ± 0.3 hours for WT and 23.7 ± 0.2 hours for $Opn4^{LacZ/LacZ}$ animals (Figure 19A, B). These animals also delayed the phase of their rhythms by 1.46 ± 0.99 hours (WT) or 0.98 ± 0.32 hours ($Opn4^{LacZ/LacZ}$) in response to a 15-minute light pulse (Figure 19A, C). Remarkably, $Opn4^{DTA/+}$ mice, which lack a large proportion of ipRGCs (~500 ipRGCs remain of which 75 ± 15 are M1 cells), photoentrained, free-ran (23.8 ± 0.2 hours), and phase shifted (1.56 ± 0.59 hours) comparable to control animals (Figure 19). Considering that the M1 ipRGCs are the major conduit for circadian photoentrainment, these data indicate that ~75 M1 ipRGCs are sufficient to convey light information for circadian photoentrainment in the presence of melanopsin (Figure 19A). In the $Opn4^{DTA/LacZ}$ mice, the remaining ~75 M1 ipRGCs lose their intrinsic photoresponse due to the loss of the melanopsin photopigment and thus can only relay rod/cone input to the brain. In these mice, circadian responses to light were highly attenuated, with inconsistent entrainment and phase-shifting (0.50 ± 0.45 hours), but still exhibited a free-running period (23.6 ± 0.2 hours) comparable to control mice (Figure 19, 20). As previously published, $Opn4^{aDTA/aDTA}$ mice were unable to photoentrain or phase shift (0.21 ± 0.28 hours) and hence free-ran under all lighting conditions (Figure 19A). Furthermore, they free-ran with a period (23.7 ± 0.3 hours) comparable to control animals (Figure 19A, B). Similar to $Opn4^{aDTA/aDTA}$ mice, $Opn4^{DTA/DTA}$ mice could not photoentrain or phase shift (0.26 ± 0.85 hours), and therefore also free-ran under all lighting conditions (Figure 19A, C; 20). Strikingly, however, $Opn4^{DTA/DTA}$ mice free-ran with a period of 24.2 ± 0.3 hours, which was significantly longer
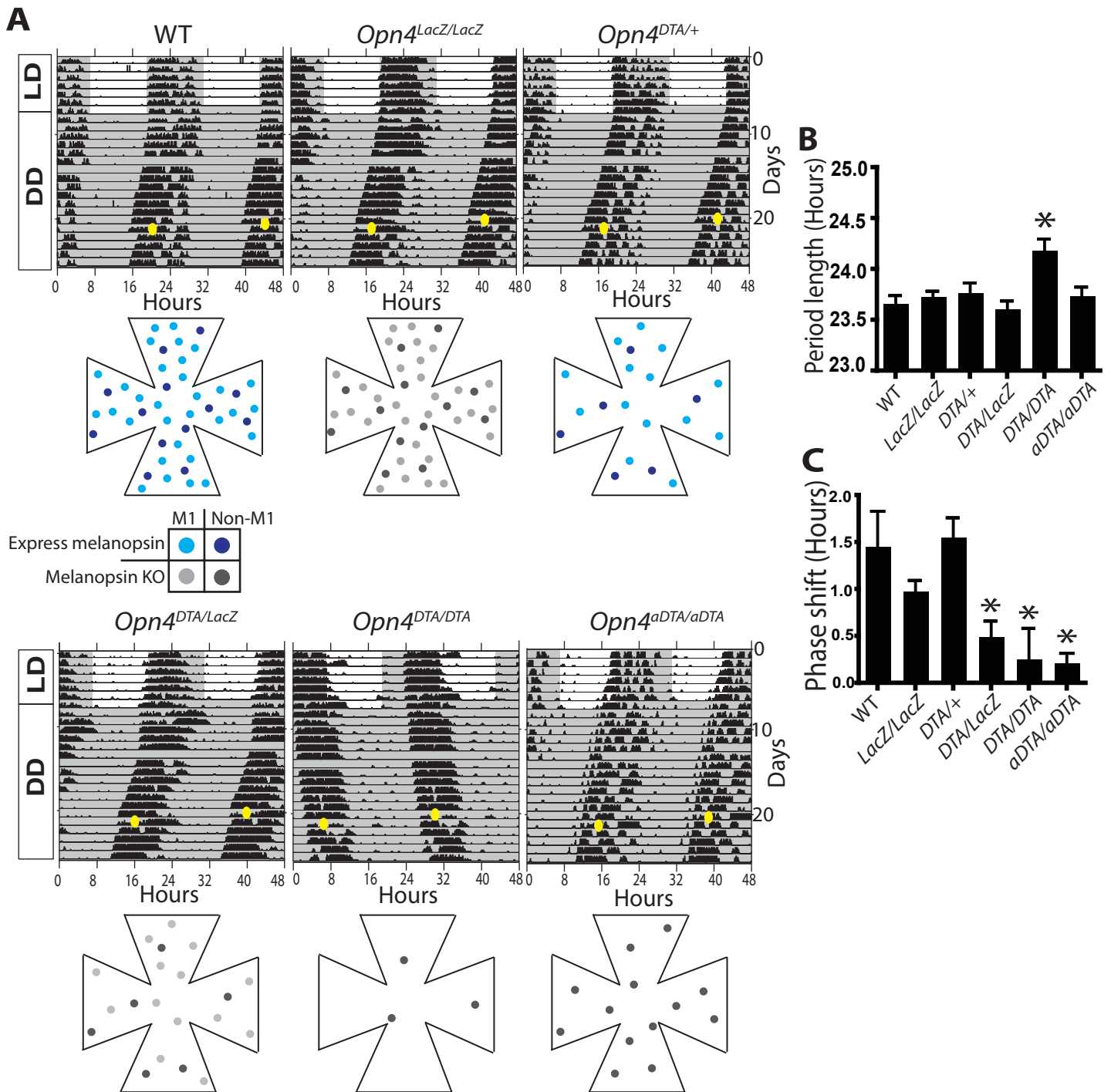
Figure 19. Opn4$^{DTA/DTA}$ mice exhibit a lengthened circadian period

A. Representative actograms of wheel running activity from WT, Opn4$^{LacZ/LacZ}$, Opn4$^{DTA/+}$, Opn4$^{DTA/LacZ}$, Opn4$^{DTA/DTA}$, and Opn4$^{aDTA/aDTA}$ mice under a 12:12 LD cycle and in constant darkness. The grey background indicates darkness, and the yellow dot indicates a 15-minute light pulse at circadian time (CT) 16. WT, Opn4$^{LacZ/LacZ}$, Opn4$^{DTA/+}$ mice photoentrained to the LD cycle while Opn4$^{DTA/DTA}$, and Opn4$^{aDTA/aDTA}$ mice mice free-ran.B. Intrinsic circadian period. Opn4$^{DTA/DTA}$ mice free-run with a significantly longer period compared to all other genotypes. All other genotypes exhibited intrinsic circadian periods indistinguishable from WT. * indicates P<0.05 by one-way ANOVA with Tukey post-hoc analysis. Error bars represent s.e.m.
C. Phase shifting. Opn4$^{LacZ/LacZ}$, and Opn4$^{LacZ/LacZ}$ mice phase shifted comparably to WT mice. Opn4$^{DTA/LacZ}$ mice exhibited severely reduced phase shifting, although the majority (5 of 7) photoentrained. Opn4$^{DTA/DTA}$ and Opn4$^{aDTA/aDTA}$ mice showed no phase shifts to light. * indicates P<0.05 by one-way ANOVA with Tukey post-hoc analysis. Error bars represent s.e.m.

A. Actograms for all *Opn4^DTA/LacZ^* mice
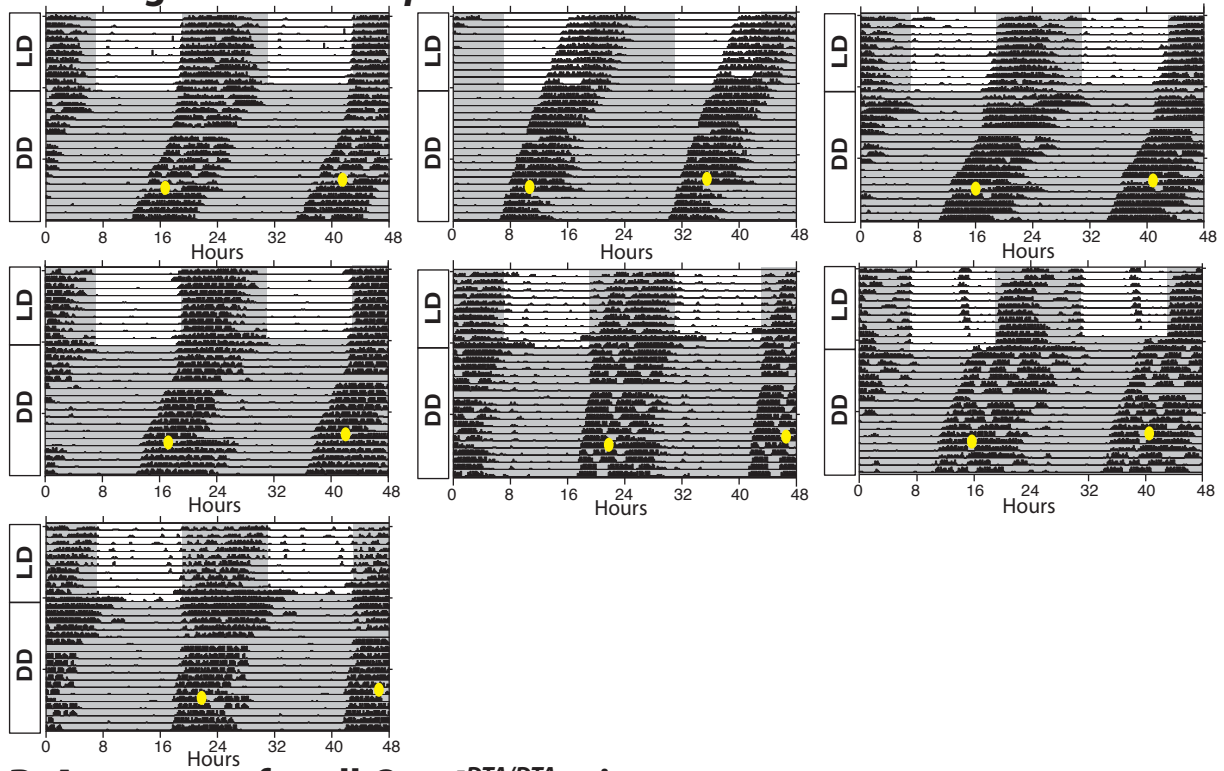
B. Actograms for all *Opn4^DTA/DTA^* mice
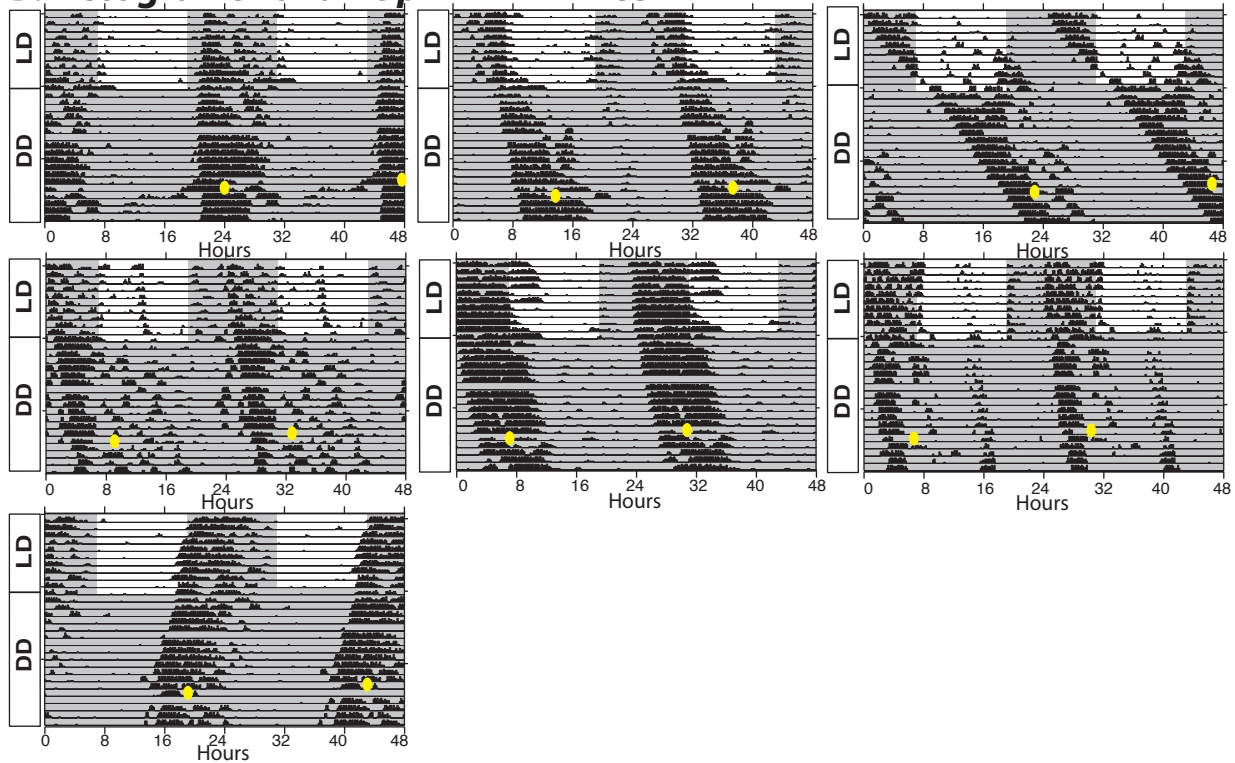
Figure 20. Actograms of all Opn4^DTA/LacZ^ and Opn4^DTA/DTA^ mice tested
A. Opn4^DTA/LacZ^ mice.
B. Opn4^DTA/DTA^ mice.

than any other line tested (Figure 19A, B; 20). Such period lengthening suggests that ipRGCs are required for setting the free running circadian period.

The difference in the intrinsic circadian period of mice expressing two copies of the full-strength DTA and those expressing the attenuated toxin could arise from either the more extensive loss of ipRGCs or the earlier loss in the $Opn4^{DTA/DTA}$ mice. In $Opn4^{DTA/DTA}$ mice, the majority of ipRGCs are lost as early as P0 (Figure 18C), whereas in $Opn4^{aDTA/aDTA}$ mice, the progressive loss of ipRGCs does not begin until adulthood and is predominantly restricted to M1 cells (Güler et al., 2008). To assess the relevance of early ablation in causing the lengthened circadian period of $Opn4^{DTA/DTA}$ mice, we bilaterally enucleated mice at P0 (8 animals) or P60 (8). Wheel-running activity was first recorded under a 12:12 LD cycle starting at P74 for 2 weeks and then under constant darkness (DD) conditions for an additional 2 weeks (Figure 22A, B). The enucleation was complete since both at P0 or at P60, mice free-ran through all lighting conditions. Importantly, the circadian period was lengthened significantly in mice enucleated at P0 (24.3 ± 0.2 hours) but not in mice enucleated at P60 (23.9 ± 0.1 hours) (Figure 22A, B). These data support the view that the lengthened circadian period exhibited by $Opn4^{DTA/DTA}$ mice is due to the early loss of ipRGCs and is consistent with the normal circadian period length in the $Opn4^{aDTA/aDTA}$ mice.

Light is necessary for setting the intrinsic period of the circadian clock

The lengthened circadian period observed after early enucleation or genetic ablation of ipRGCs could be due either to developmental changes in the denervated SCN or due to the elimination of light-driven input from ipRGCs. To test whether the lengthened circadian period exhibited by $Opn4^{DTA/DTA}$ (but not $Opn4^{DTA/+}$) mice could be attributed to

gross changes in the SCN, we examined expression of several developmentally important

transcription factors, Rora, Six3, and Lhx1 (VanDunk et al., 2011) as well as the functionally

important neuropeptide vasopressin (AVP) in control ($Opn4^{DTA/+}$) and $Opn4^{DTA/DTA}$ mice

(Figure 21). The expression patterns of these genes was similar between these two groups

of mice indicating that the lengthened circadian period exhibited by $Opn4^{DTA/DTA}$ mice is

unlikely to be attributed to gross changes in the SCN.

To then determine if light-driven input from ipRGCs is important in establishing the

circadian period, we raised WT animals from birth either under a 12:12 LD cycle (n=6) or

under constant darkness (n=17). At P60, we assessed the intrinsic circadian period of these

animals by recording their wheel running activity in constant darkness (Figure 22C, D; 23).

Dark-reared mice had significantly longer intrinsic circadian periods (24.0 ± 0.3 hours)

than mice raised in a light-dark cycle (23.6 ± 0.1 hours) (Figure 22D) and remained stable

in constant darkness for at least 3 months (Figure 22C and D; 23). The lengthened period in

these dark reared animals was similar to mice with early loss of retinohypothalamic input

either through ennucleation at P0 or through genetic ablation of ipRGCs ($Opn4^{DTA/DTA}$).

After characterizing their intrinsic circadian period, we exposed the dark-reared

mice to a 12:12 LD cycle for 2 weeks, followed by a six-hour advance of the LD cycle for an

additional two weeks. Consistent with previous literature (Kampf-Lassin et al., 2011;

Prichard et al., 2004), dark-reared mice, like those raised in an LD cycle, were able to

photoentrain normally (Figure 22C, D; 23). Surprisingly, when dark-reared mice were then

returned to constant darkness, their intrinsic circadian periods became less than 24 hours

(23.7 ± 0.2 hours) and were statistically indistinguishable from mice reared in a standard

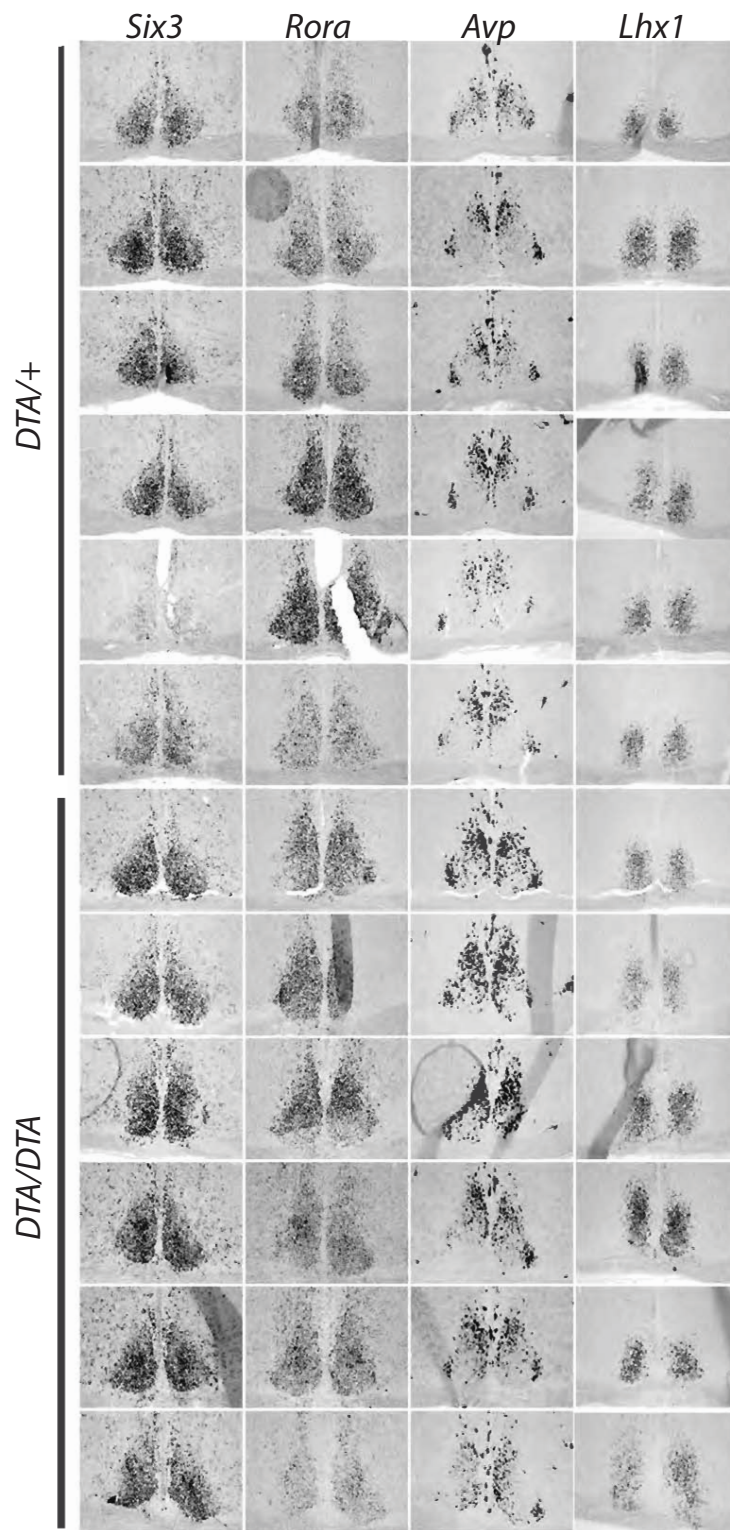LD cycle (Figure 22C, D; 23). Thus, light exposure (LD cycles) dramatically altered the

Figure 21: Expression pattern of transcription factors critical for SCN development
Images of in situ hybridization for several developmentally important transcription factors, Rora, Six3, and Lhx1 as well as the functionally important neuropeptide vasopressin (AVP) in control (Opn4[DTA/+]) and Opn4[DTA/DTA] mice. Each row represents one animal.
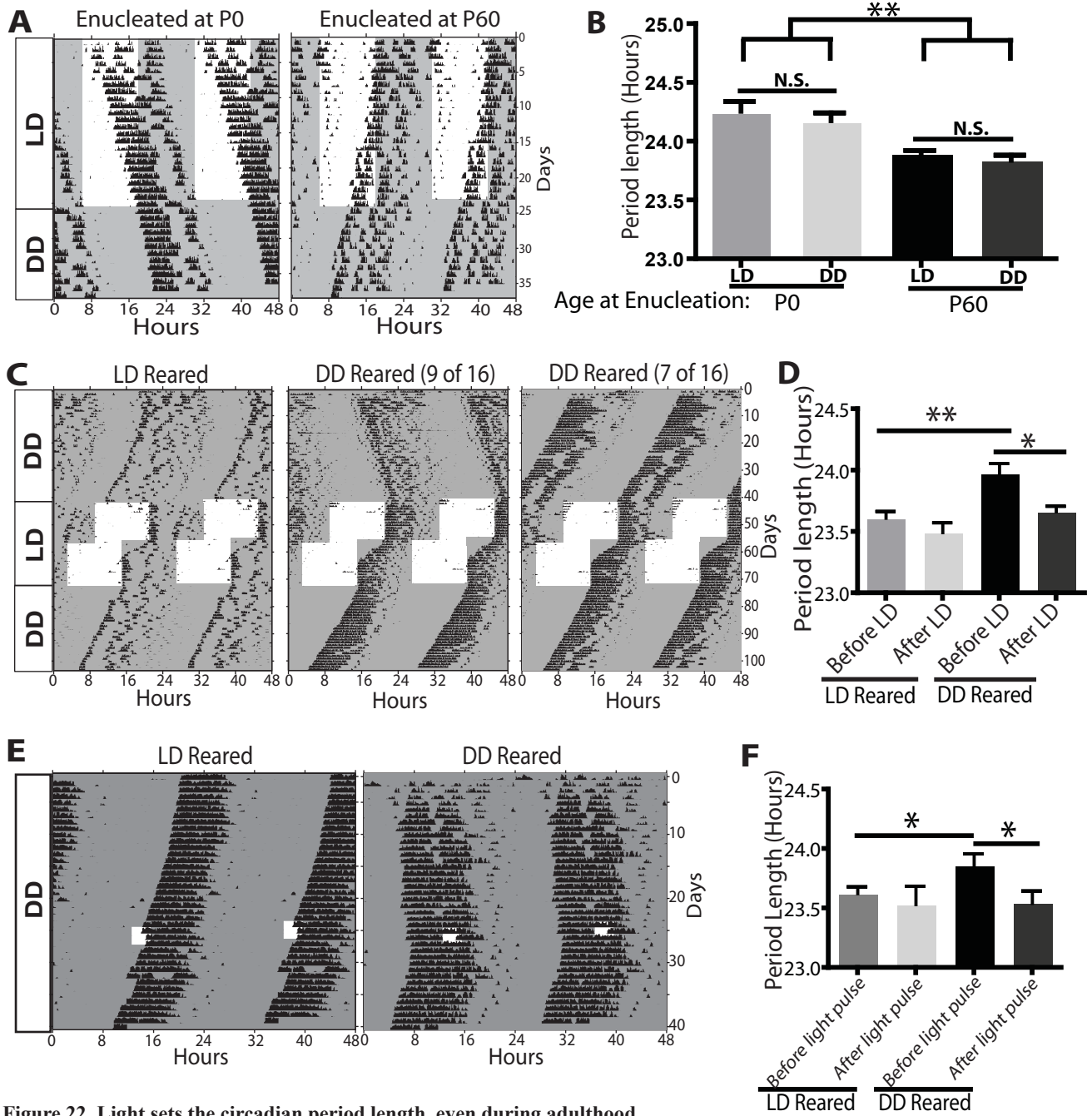
Figure 22. Light sets the circadian period length, even during adulthood
A. Representative wheel running activity actograms of WT mice, enucleated at either P0 or P60, under a 12:12 LD cycle and in constant darkness. B. Intrinsic circadian period. For either enucleation group there is no difference between the circadian period under a 12:12 LD cycle and under constant darkness. However, mice enucleated at P0 exhibited a significantly longer circadian period than mice enucleated at P60 (P0, 24.3 ± 0.2 hours vs. P60, 23.9 ± 0.1 hours). ** indicates $P<0.001$ with Student's t-test. Error bars represent s.e.m. C. Representative wheel running activity actograms of WT mice raised in either a 12:12 LD cycle or in constant darkness, and exposed to 12:12 LD cycle for 1 month. D. Intrinsic circadian period. Mice raised in constant darkness exhibited a significantly longer intrinsic circadian period (24.0 ± 0.3 hours) than mice raised in a 12:12 LD cycle (23.6 ± 0.1 hours). All mice photoentrained upon exposure to a 12:12 LD cycle and re-photoentrained following a 6-hour shift in the LD cycle. Following photoentrainment, the intrinsic circadian period of dark reared mice, under constant dark conditions, was then indistinguishable from mice raised in a 12:12 LD cycle. * indicates $P<0.05$ and ** indicates $P<0.001$ with Student's t-test. Error bars represent s.e.m. E. Representative wheel running activity actograms of WT mice raised in either a 12:12 LD cycle or in constant darkness, and then exposed to a 3 hour light pulse F. Mice raised in constant darkness exhibited a significantly longer intrinsic circadian period (23.9 ± 0.3 hours) than mice raised in a 12:12 LD cycle (23.6 ± 0.2 hours). All mice were given a 3 hour light pulse. Following this light pulse, the intrinsic circadian period of dark reared mice, under constant dark conditions, was then indistinguishable from mice raised in a 12:12 LD cycle. * indicates $P<0.05$ with Student's t-test. Error bars represent s.e.m.

All actograms for dark reared mice
Lengthened Period:
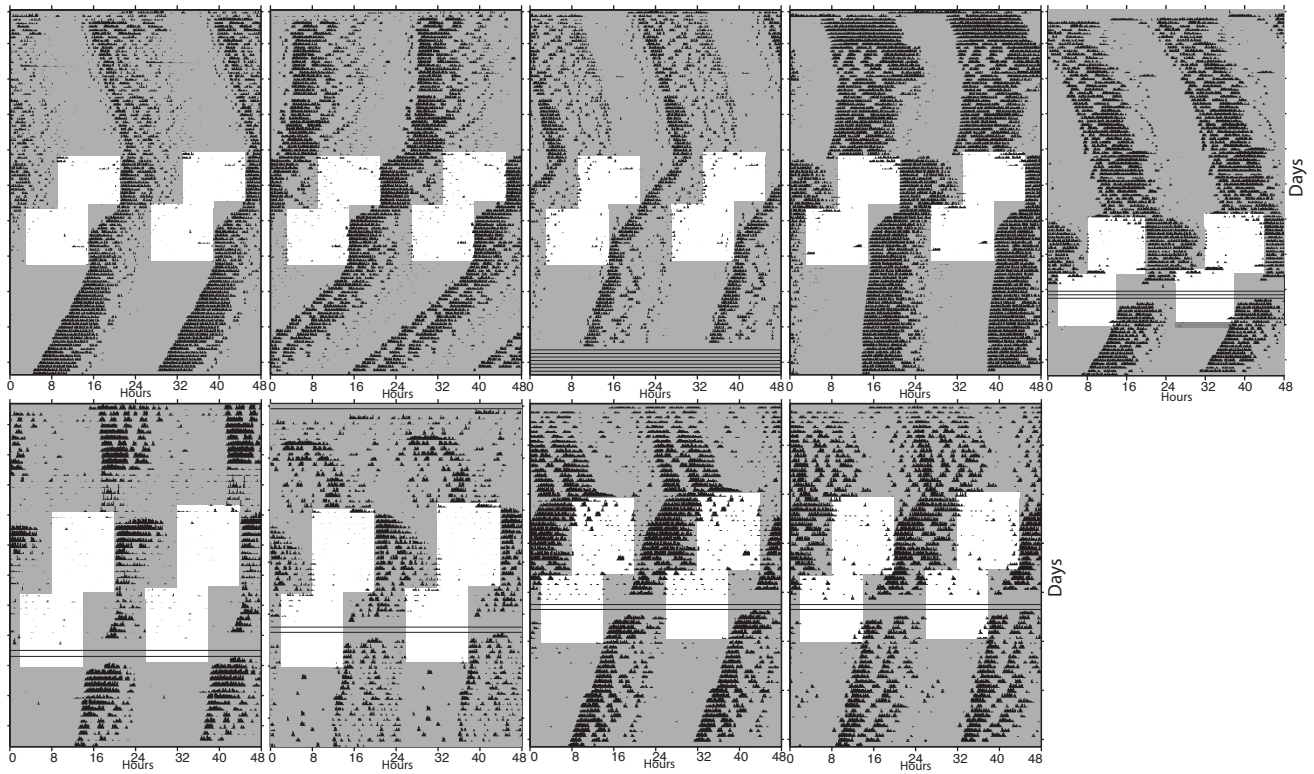
WT Period:
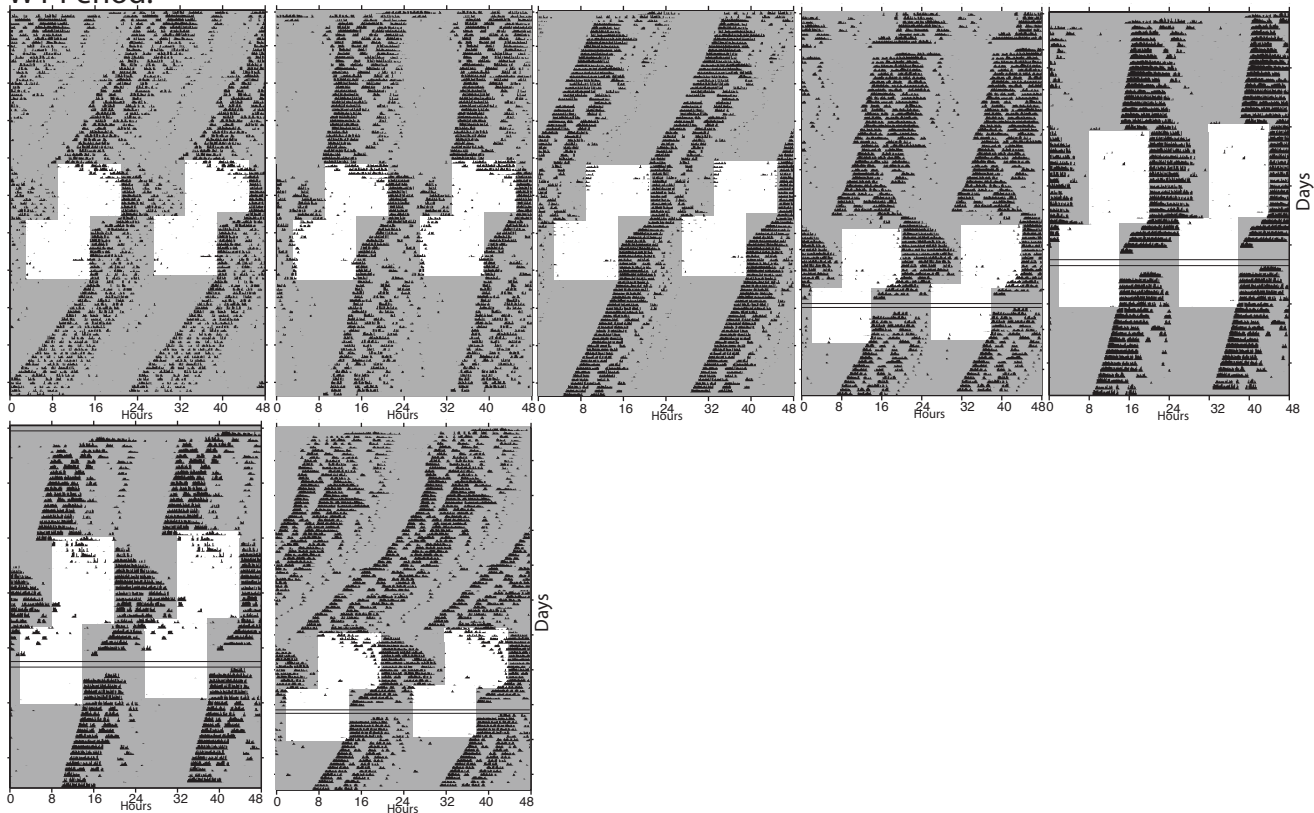
Figure 23: Actograms for all dark reared mice tested

circadian behavior of dark-reared mice. These data show that light input via ipRGCs is necessary for setting the circadian period and further, that upon light exposure, even in adults, the intrinsic circadian period is irreversibly set.

The remarkable plasticity in the circadian period length of WT animals raised under DD conditions, promoted us to determine the minimum length of light that could restore the circadian period. To do this, we reared WT animals from birth either under a 12:12 LD cycle or under constant darkness, recorded their wheel running activity under constant darkness and then exposed the animals to only a 3-hour light pulse (Figure 22E, F). After this 3-hour light pulse all dark-reared animals exhibited circadian periods that were statistically indistinguishable from mice reared in a standard LD cycle (Figure 22E, F). Thus, these data show that, surprisingly, merely 3-hours of light is sufficient to set the intrinsic circadian period of dark-reared animals.

Ablation of ipRGCs disrupts the organization of retinal projections to image-forming centers

Previously, we showed that ablating ipRGCs in adults does not cause any deficits in the retinal innervation of the dLGN, an area of the brain important for image formation (Güler et al., 2008). In adults, the dLGN receives segregated axonal input from the left and right eyes. We predicted that the innervation of the dLGN would be unaffected in adult *Opn4$^{DTA/DTA}$* mice. By tracing the axonal projections of all retinal ganglion cells with CTB at P60, we were surprised to observe that eye-specific axonal segregation was severely disrupted in the dLGN of adult *Opn4$^{DTA/DTA}$* mice (Figure 24A,B 25). Specifically, the boundaries of the ipsilateral terminal zone were much less defined in *Opn4$^{DTA/DTA}$* mice
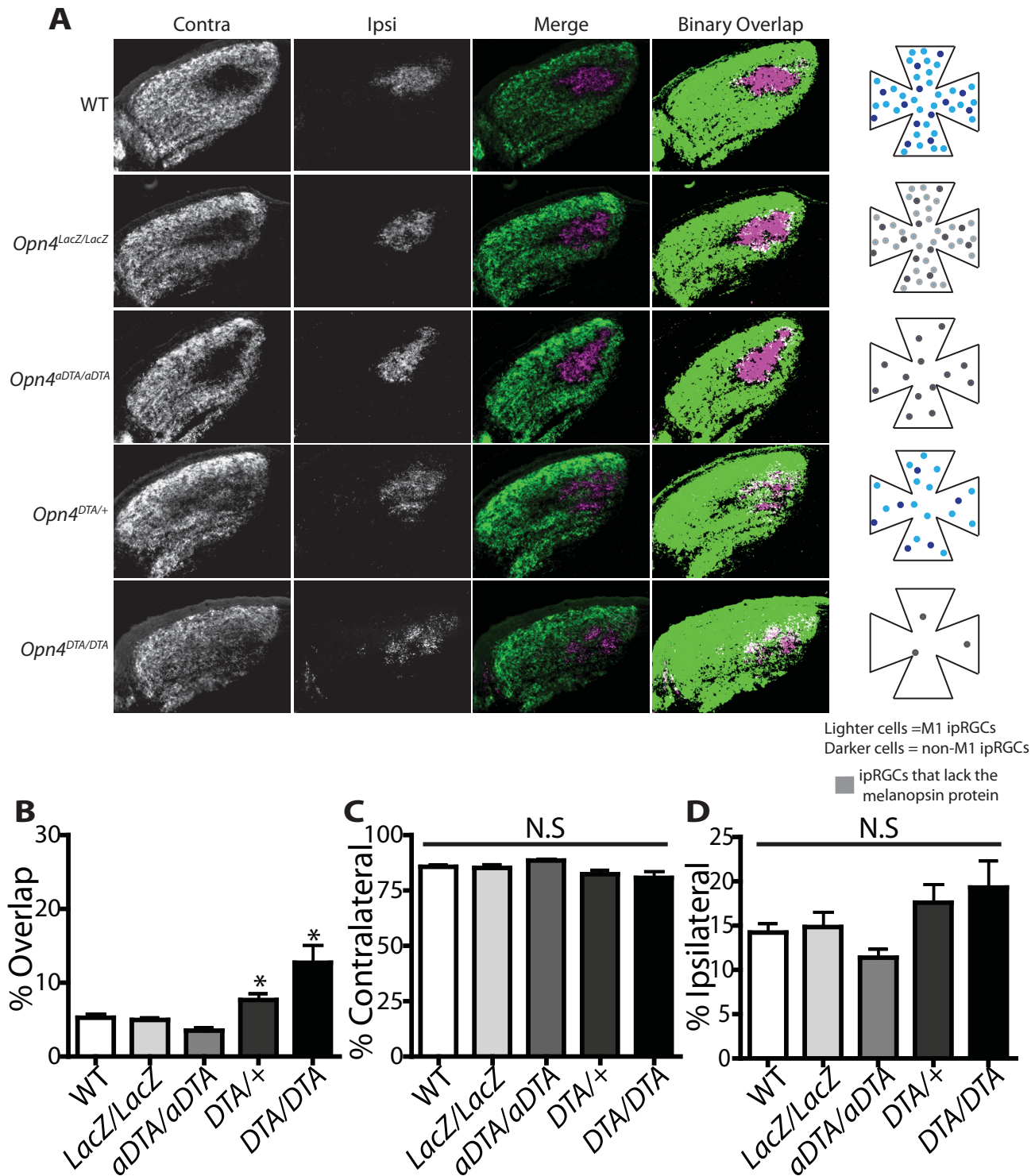
Figure 24. Adult Opn4$^{DTA/DTA}$ mice display disruption of eye-specific axonal segregation in the dLGN

A. RGC axonal innervation of the adult dLGN of WT, Opn4$^{LacZ/LacZ}$, Opn4$^{aDTA/aDTA}$, Opn4$^{DTA/+}$, and Opn4$^{DTA/DTA}$ mice. Alexa Fluor 594-(purple) and 488-(green) conjugated CTB were injected into the right and left eye respectively to label RGC projections. Images are of the right dLGN. The rightmost images represent a binarized version of the merged images to visualize the overlap between contralateral and ipsilateral RGC projections. B. Opn4$^{DTA/DTA}$ mice exhibited a significantly higher percentage of overlapping pixels (measured as number of pixels within the dLGN that contained fluorophore signals from both the contralateral and ipsilateral eyes) relative to the total number of LGN than any other tested genotype. Opn4$^{LacZ/LacZ}$ and Opn4$^{aDTA/aDTA}$ mice exhibited levels of overlapping pixels that were indistinguishable from WT. Opn4$^{DTA/+}$ mice exhibited levels of overlapping pixels that were intermediate compared to Opn4$^{DTA/DTA}$ and control mice. ** indicates $P<0.05$ by one-way ANOVA with Tukey post-hoc analysis. Error bars represent s.e.m. C. The percentage of the total number of pixels in the dLGN from ipsilateral fibers is similar among all tested genotypes. One-way ANOVA with Tukey post-hoc analysis. Error bars represent s.e.m. D. The percentage of the total number of pixels in the dLGN from contralateral fibers is similar among all tested genotypes. One-way ANOVA with Tukey post-hoc analysis. Error bars represent s.e.m.

74
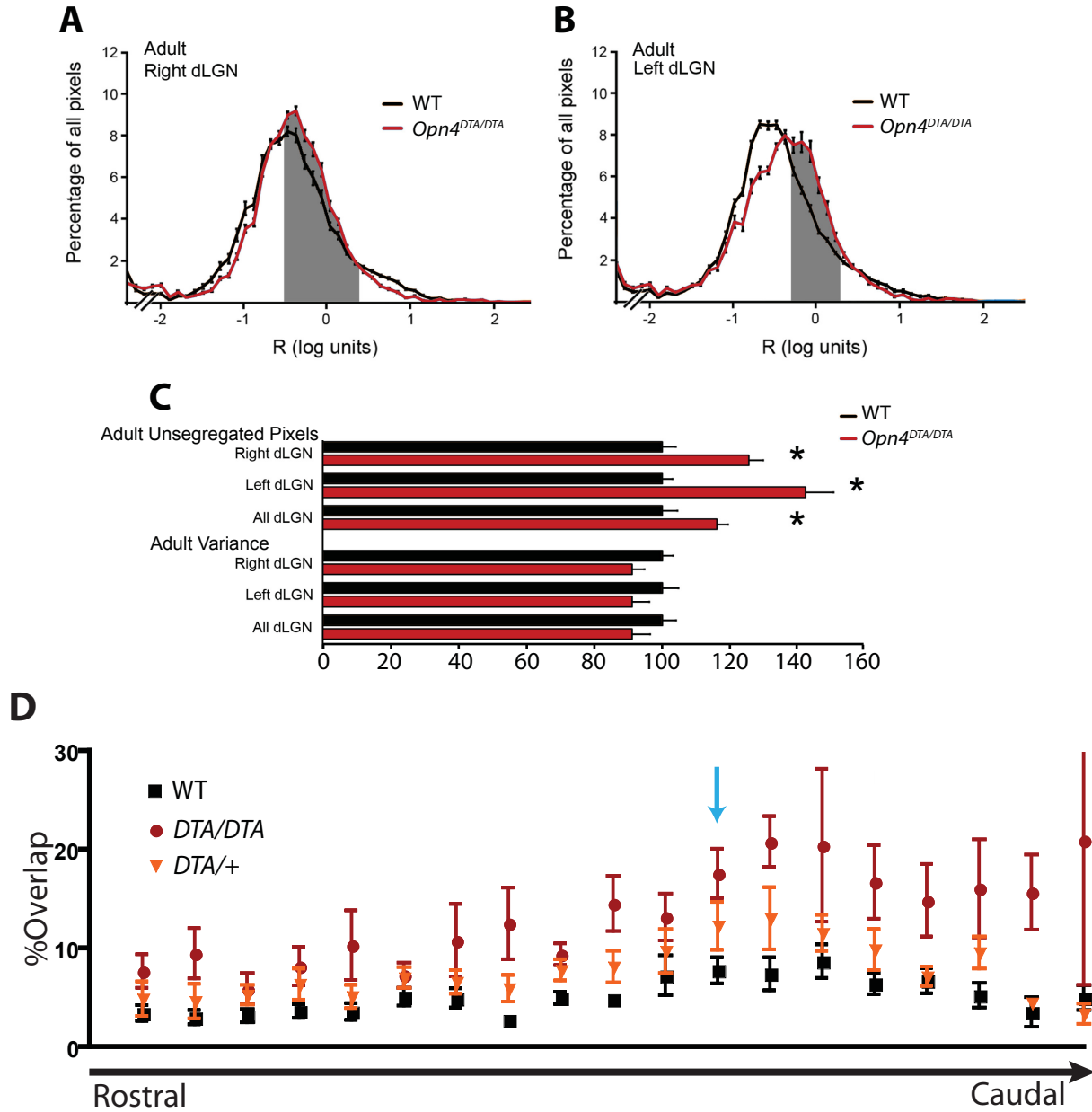
Figure 25: Disruption of eye-specific axonal segregation in the dLGN of adult Opn4$^{DTA/DTA}$ mice.
A-B. The averaged distribution of pixel intensity ratios (R) for all dLGN pixels in the right (A) and left (B) dLGN of adult WT (black curve) and Opn4$^{DTA/DTA}$ (red curve) mice are plotted. The mice were raised in 12:12 LD cycle. Opn4$^{DTA/DTA}$ mice have more unsegregated pixels (gray shaded area-see methods) than WT mice.
C. Pooled data normalized to WT mice indicated Opn4$^{DTA/DTA}$ mice have 16% more unsegregated pixels, and a 9% decrease in the variance of the R distribution (n= 4 WT, 4 Opn4$^{DTA/DTA}$, 15 sections/mouse/hemisphere). * indicates $p < 0.0001$. Error bars represent s.e.m.
D. The rostral to caudal distribution of percent overlap between contralateral and ipsilateral projections through the dLGN. The blue arrow indicates the section of the dLGN presented in (Figure 24). Error bars represent s.e.m.

compared to WT animals. In $Opn4^{DTA/DTA}$ mice, the ipsilateral zone contained substantial input from contralateral innervation, whereas in WT mice the ipsilateral terminal zone was devoid of contralateral input (Figure 24). We quantified these effects using three methods (Demas et al., 2006; Renna et al., 2011) and we describe these methods in detail in supplemental text (section 1.2). These results indicate that ipRGC ablation causes deficits in conventional ganglion cell axonal segregation in the dLGN.

The deficits in the $Opn4^{DTA/DTA}$ mice in the axonal segregation in the dLGN could arise from the lack of the melanopsin protein, the lack of ipRGCs in adult animals or the lack of ipRGCs during development. To test this, we used melanopsin knockout animals ($Opn4^{LacZ/LacZ}$), which lack the melanopsin protein, but retain the ipRGCs, and $Opn4^{aDTA/aDTA}$ mice, in which ipRGCs are only ablated in adults. In $Opn4^{LacZ/LacZ}$ and $Opn4^{aDTA/aDTA}$ mice, the percentage of overlap was indistinguishable from WT (Figure 24A, B). This indicates that neither melanopsin phototransduction nor the presence of ipRGCs in adults is required for ipRGCs to regulate the refinement of conventional RGCs, and rather, ipRGCs are indeed required during development to regulate the refinement of conventional RGC projections.

We then sought to determine if the extent of ipRGC loss during development correlated with the severity of the deficits in eye-specific axonal segregation in the dLGN. To test this, we utilized $Opn4^{DTA/+}$ mice that have less ipRGC ablation than $Opn4^{DTA/DTA}$ mice (Figure 17C). Interestingly, $Opn4^{DTA/+}$ mice exhibited an intermediate increase in the percentage of overlapping pixels compared to control and $Opn4^{DTA/DTA}$ mice (Figure 24A, B). Thus, these results reveal a correlation between the number of ipRGCs lost developmentally and the severity of the deficits in the eye-specific axonal segregation of conventional RGCs.

Three independent methods for quantifying eye-specific segregation in the dLGN

We first quantified eye-specific axonal segregation in the dLGN using a methods described previously (Demas et al., 2006). We measured the number of pixels within the dLGN that contained fluorophore signals from both the contralateral and ipsilateral eyes (presented as percent overlap relative to the total number of LGN pixels; Figure 24B). We found a significant increase in the percentage of overlapping pixels *Opn4^DTA/DTA* mice (Figure 24B). Additionally, the segregation defects were more severe in the central to caudal regions of the dLGN (Figure 25D). Importantly, the number of pixels from ipsilateral and contralateral fibers (presented as percent ipsilateral and percent contralateral relative to the total number of LGN pixels; Figure 24C, D) were not different between WT and *Opn4^DTA/DTA* mice (Figure 24C, D).

To further confirm the deficits in eye-specific segregation observed in *Opn4^DTA/DTA* mice, we utilized two additional methods of quantification (Pfeiffenberger et al., 2005; Renna et al., 2011). First, we identified pixels within the dLGN as 'mixed' if they received more balanced input from the two eyes than 99% of the pixels in the regions maximally dominated by input from one eye (Renna et al., 2011). Mice with early ablation of ipRGCs had significantly more such 'mixed' pixels throughout the dLGN than did WT controls eyes (WT, 36.71 $\pm$ 1.42%; *Opn4^DTA/DTA*, 46.04 $\pm$ 1.53%; p $\leq$ 0.0001; Figure 25A, B). Second, we applied an alternative analytic method, based on the variance of the distribution of the log ratio of ipsilateral and contralateral pixel values for each dLGN section (Torborg and Feller, 2004). In this analysis, reductions in segregation are reflected in lower variances, and this approach further confirmed the earlier analyses, with *Opn4^DTA/DTA* mice exhibiting a strong trend toward a lower variance in pixel values (i.e., less segregation) than in WT controls

(WT 0.433 $\pm$ 0.01; $Opn4^{DTA/DTA}$ 0.394 $\pm$ 0.02; p $\leq$ 0.058; Figure 25C). Combined, the three quantification methods showed that axonal segregation in the dLGN is severely disrupted in $Opn4^{DTA/DTA}$ mice.

Deficits in eye-specific axonal segregation in dLGN are present as early as P8

At early postnatal stages contralateral and ipsilateral retinal projections are less organized and refined during postnatal stages into a precise, stereotyped, and segregated pattern. Specifically, refinement of conventional RGC axons is associated with the onset of spontaneously driven activity in retina, termed retinal waves, which occur during the first postnatal week (Ackman et al., 2012; Chandrasekaran et al., 2005; Feller, 2002, 2009; Firth et al., 2005; McLaughlin et al., 2003a; Meister et al., 1991; Mrsic-Flogel et al., 2005; Muir-Robinson et al., 2002; Shatz and Stryker, 1988; Stellwagen and Shatz, 2002; Wong, 1999; Xu et al., 2011; Zhang et al., 2011). Thus, to help elucidate the mechanism by which ipRGCs could affect the eye-specific segregation of conventional RGCs, we sought to determine the age at which deficits arise. We raised $Opn4^{DTA/DTA}$ and WT mice in 12:12LD for the first week of life, injected CTB into the two eyes to trace the projections of all RGCs at P7, and harvested tissues at P8. We found a significant increase in the percentage of overlapping pixels $Opn4^{DTA/DTA}$ mice (Figure 26A, B). Importantly, the percentages of pixels from ipsilateral and contralateral fibers (Figure 26C, D) were not different between WT and $Opn4^{DTA/DTA}$ mice (Figure 26C, D). These data indicate that the deficits in eye-specific axonal segregation in dLGN in $Opn4^{DTA/DTA}$ mice are present as early as P8.

Ablation of ipRGCs alters the dynamics of spontaneous activity in the retina
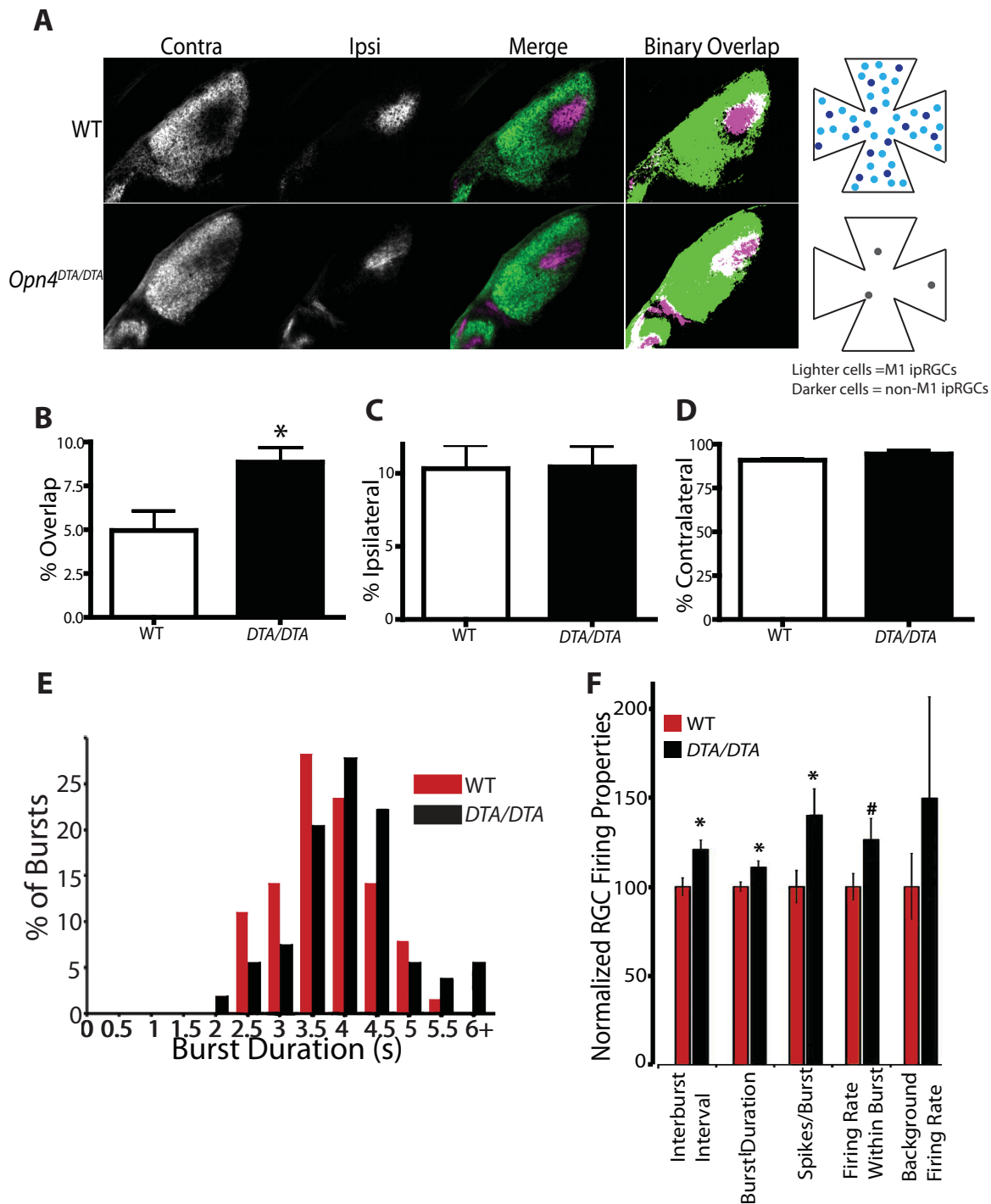
Figure 26. Opn4[DTA/DTA] mice display disrupted eye-specific axonal segregation as early as P8 and exhibit altered retinal wave dynamics

A. RGC axonal innervation of the dLGN in P8 WT and Opn4[DTA/DTA] mice. Alexa Fluor 594- (purple) and 488-(green) conjugated CTB were injected into the right and left eye respectively to label RGC projections. Injections were made at P7, and tissues were analyzed at P8. Images are of the right dLGN. The rightmost images represent a binarized version of the merged images to visualize the overlap between contralateral and ipsilateral RGC projections. B. At P8, Opn4[DTA/DTA] mice exhibit a significantly higher percentage of overlapping pixels (measured as number of pixels within the dLGN that contained fluorophore signals from both the contralateral and ipsilateral eyes) relative to the total number of LGN pixels than WT mice. * indicates $P< 0.05$ with Student's t-test; Error bars represent s.e.m. C. The percentage of the total number of pixels in the dLGN from ipsilateral fibers is not different between WT and Opn4[DTA/DTA] mice. Student's t-test; Error bars represent s.e.m. D. The percentage of the total number of pixels in the dLGN from contralateral fibers is not different between WT and Opn4[DTA/DTA]mice. Student's t-test; Error bars represent s.e.m. E. Distribution of wave-associated burst durations for individual ganglion cells. F. RGC spiking properties. The values were normalized to WT. Opn4[DTA/DTA] mice exhibit increased interburst interval (fewer bursts per minute), increased burst duration, and more spikes per burst. n=3 retinas (from 3 mice) of each genotype, n=64 cells from WT and n=54 cells from Opn4[DTA/DTA]. * indicates $p< 0.05$ and # indicates $p= 0.054$ with Student's t-test. Error bars represent s.e.m.
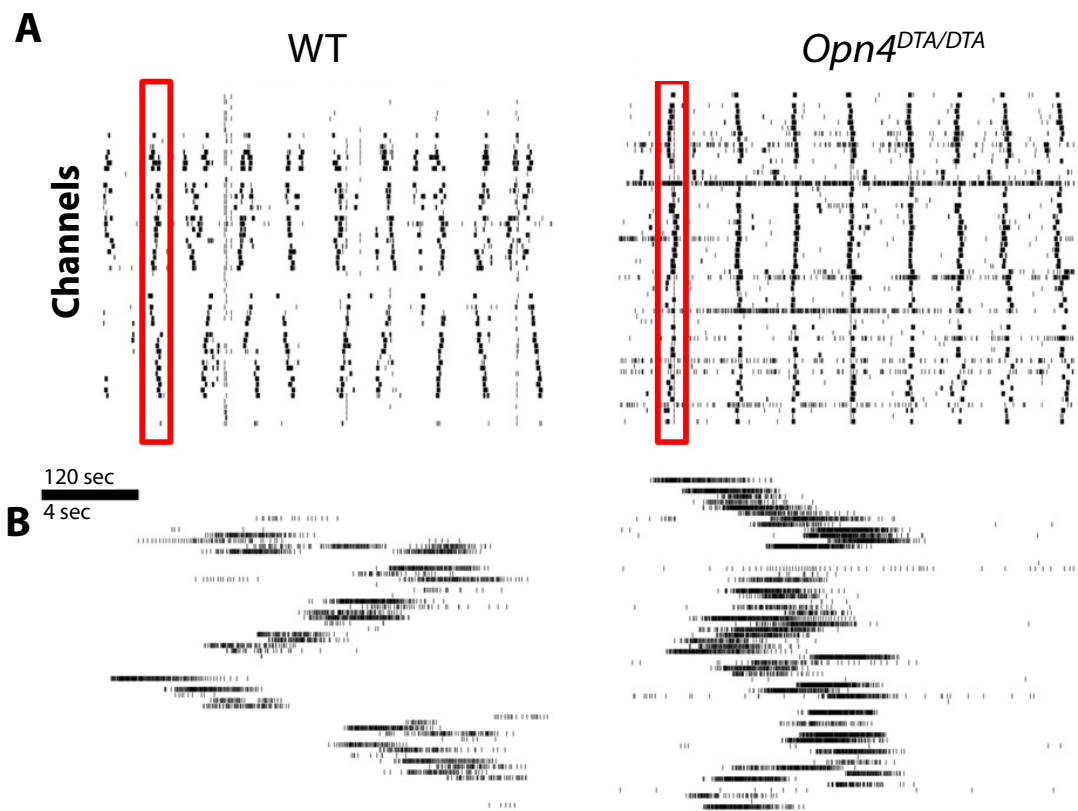
Figure 27: Opn4^DTA/DTA mice display altered retinal wave dynamics
A. Representative raster plots from multielectrode array (MEA) recording of retinal waves in P6 WT and Opn4^DTA/DTA mice in the dark. Each row represents the activity on a single electrode.
B. Expansion of one burst (identified by the red box in (A)).

The spatiotemporal patterns of retinal wave activity are considered important for the postnatal refinement of contralateral and ipsilateral retinal projections to image forming targets (Ackman et al., 2012; Chandrasekaran et al., 2005; Feller, 2002, 2009; Firth et al., 2005; McLaughlin et al., 2003a; Meister et al., 1991; Mrsic-Flogel et al., 2005; Muir-Robinson et al., 2002; Shatz and Stryker, 1988; Stellwagen and Shatz, 2002; Wong, 1999; Xu et al., 2011; Zhang et al., 2011). Retinal waves begin instructing RGC axonal refinement at early postnatal ages, coincident with the deficits in eye-specific axonal segregation in *Opn4$^{DTA/DTA}$* mice. We therefore explored the possibility that the deficits we observed in eye-specific axonal segregation of conventional RGCs in *Opn4$^{DTA/DTA}$* mice could be due to perturbations in retinal wave activity.

It has been recently shown that light can modulate retinal waves in a melanopsin-dependent manner (Renna et al., 2011); however, *Opn4$^{LacZ/LacZ}$* mice, which lack melanopsin phototransduction but retain all ipRGCs, do not exhibit any changes in spontaneous retinal waves in darkness (Renna et al., 2011) and do not exhibit disrupted eye-specific axonal segregation at adult stages (Figure 24A, B). Therefore, we recorded retinal waves in *Opn4$^{DTA/DTA}$* mice in the absence of light. We mounted isolated retinas from P6 mice on a multielectrode array (MEA) and recorded in complete darkness the spiking activity of single ganglion cells in both WT and *Opn4$^{DTA/DTA}$* mice (n = 3 retinas per genotype; WT = 64 cells; *Opn4$^{DTA/DTA}$* = 54 cells; Figure 27A,B). Mice with early ipRGC ablation (*Opn4$^{DTA/DTA}$*) exhibited an increase in the duration of wave-associated bursting (WT, 3.48 $\pm$ 0.091 sec; *Opn4$^{DTA/DTA}$*, 3.81 $\pm$ 0.12 sec; p $\leq$ 0.05; Figure 26E, F, Burst Duration), and an increase in the number of spikes per burst (WT, 92.5 $\pm$ 8.4; *Opn4$^{DTA/DTA}$*, 129.6 $\pm$ 13.7; p $\leq$ 0.05; Figure 26F, Spikes/Burst). There was no significant change in the elevated mean firing rate during the

burst (WT, 25.28 $\pm$ 1.88 Hz; *Opn4^DTA/DTA*, 31.96 $\pm$ 3.00 Hz; p = 0.054; Figure 26F, Firing Rate

Within Burst), or in the background firing rate (WT, 0.06 $\pm$ 0.01 Hz; *Opn4^DTA/DTA*, 0.09 $\pm$ 0.03

Hz; p = 0.38; Figure 26F, Background Firing Rate). This suggests that the change in wave-

associated spiking is the result of modulation of the wave-generating network, rather than

a change in basal excitability of the ganglion cells. In fact, despite the enhanced activity of

individual ganglion cells during the waves, the inter-burst interval was significantly longer

in *Opn4^DTA/DTA* than in WT mice (WT, 56.49 $\pm$ 2.82 sec; *Opn4^DTA/DTA*, 68.31 $\pm$ 2.93 sec; p $\leq$

0.0005; Figure 26F, Interburst Interval). These data provide the first evidence that ipRGCs

modulate normal retinal wave activity even in darkness, and specifically, are critical for

normal spatiotemporal properties of the waves.

Interestingly, changes in the dynamics of retinal waves result in deficits in eye-

specific axonal segregation in the dLGN but not in the superior colliculus (SC) (Xu et al.,

2011). This is in contrast to blocking retinal waves, which are associated with reductions in

eye-specific segregation in both the dLGN and the SC (Xu et al., 2011). Since we observed

changes in the dynamics of retinal waves in *Opn4^DTA/DTA* mice, we measured retinal

innervation of the eye-specific segregation in the SC in these animals. The ablation of

ipRGCs has no effect on the innervation of the SC by retinal fibers in the *Opn4^DTA/DTA* mice.

Furthermore, as shown previously in animals that have only changes in the dynamics of

retinal waves (Xu et al., 2011), the segregation of contralateral and ipsilateral retinal

projections to the SC in *Opn4^DTA/DTA* mice is comparable to WT (Figure 28). Normal eye-

specific segregation in the SC bolsters our conclusion that the changes in retinal wave

dynamics that occur in the absence of ipRGCs underlie the deficits observed in dLGN

segregation.
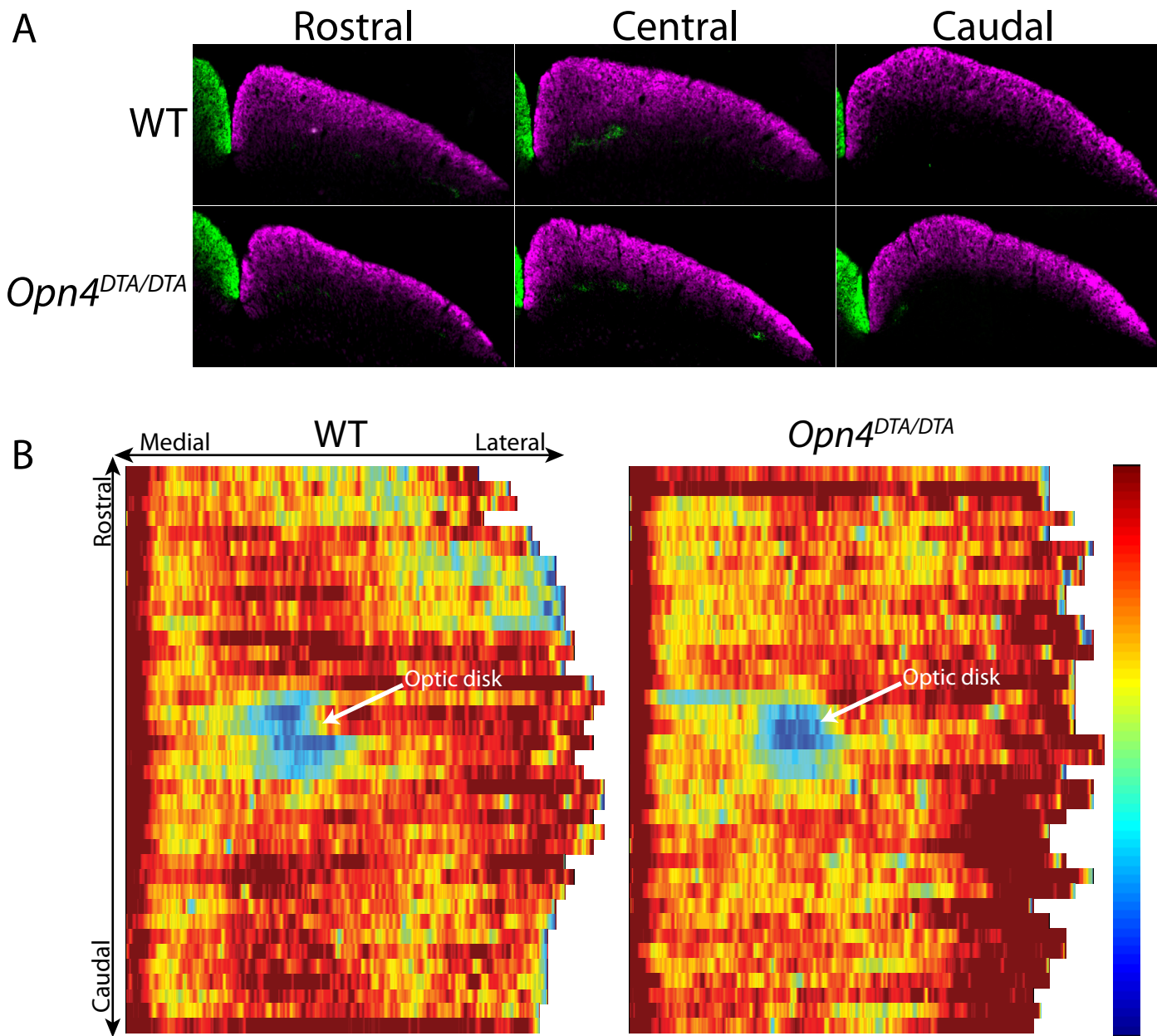
Figure 28: Retinal innervation of the SC in Opn4$^{DTA/DTA}$ mice is indistinguishable from WT mice
A. Representative images of RGC axonal innervation of the adult SC in WT and Opn4$^{DTA/DTA}$ mice. Alexa Fluor 594- (purple) and 488-(green) conjugated CTB were injected into the right and left eye respectively to label RGC projections. Images are of the left SC. B. Heat map showing a reconstruction of the dorsal view of the SC retinotopic map

Mice with early postnatal ablation of ipRGCs have deficits in visual acuity

To determine the functional consequence of the disruptions in eye-specific segregation in the dLGN observed in animals with early ipRGC ablation, we compared adult (2-4 month old) WT (n=10), *Opn4^{LacZ/LacZ}* (n=6), *Opn4^{DTA/+}*(n=6), and *Opn4^{DTA/DTA}* (n-10) mice on two behavioral tests of visual acuity: the virtual optomotor system and the visual water task (Douglas et al., 2005; Prusky et al., 2000). By both measures, *Opn4^{DTA/DTA}* animals exhibited reduced visual acuity compared to controls (WT and *Opn4^{LacZ/LacZ}*; Figure 29A, B). Thus, these data demonstrated that the loss of ipRGCs at an early postnatal stage leads to severe visual deficits. Interestingly, *Opn4^{DTA/+}* mice exhibited deficits that were intermediate between controls and *Opn4^{DTA/DTA}* mice (Figure 29A, B), which mirror the intermediate deficits observed in axonal segregation (Figure 24). Thus, the amount of ipRGC ablation correlates with the severity in deficits in eye-specific axonal segregation, which in turn correlates with the extent in the reduction of visual function.

Merely 200 M1 ipRGCs are sufficient for both setting the intrinsic period of the circadian clock and refining the imaging-forming visual system

The five subtypes of ipRGCs project to different brain regions that include both image and non-image centers. M1 ipRGCs project to non-image-forming targets, and M2-M5 ipRGCs project at least in part to image-forming targets (Ecker et al., 2010; Estevez et al., 2012). The M1 subtype can be further subdivided based on whether or not the transcription factor Brn3b (Pou4f2) is expressed (Chen et al., 2011; Jain et al., 2012). Among M1 ipRGCs, about 200 cells do not express Brn3b, project only to circadian centers
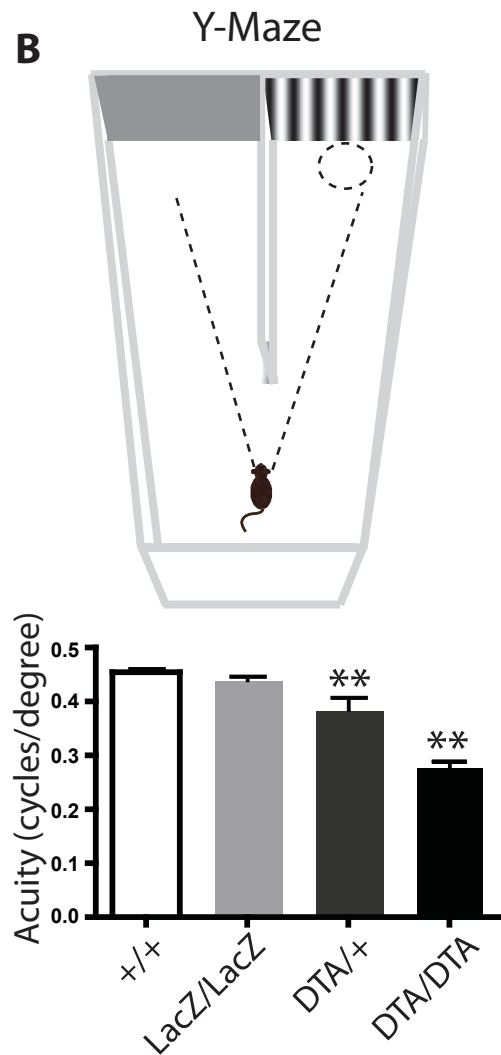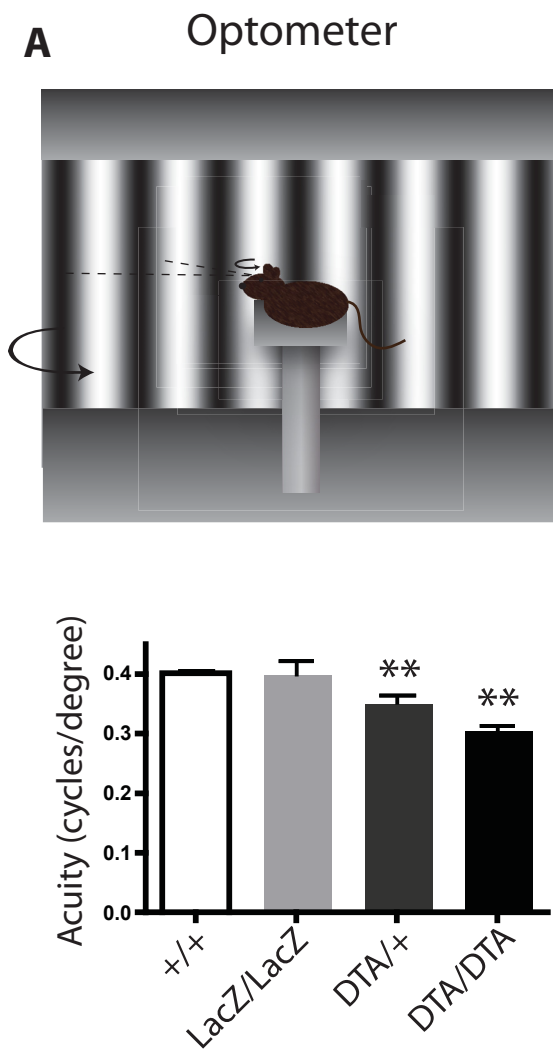
Figure 29: Opn4$^{DTA/DTA}$ mice have deficits in visual tasks

A. The virtual optokinetic system was used to assess visual function WT, Opn4$^{LacZ/LacZ}$, Opn4$^{DTA/+}$, and Opn4$^{DTA/DTA}$ mice. WT and Opn4$^{LacZ/LacZ}$ mice were indistinguishable. Opn4$^{DTA/DTA}$ mice exhibit a significantly lower spatial frequency threshold (0.31 ± 0.02 cycles/degree) than WT mice (0.40 ± 0.02 cycles/degree), and Opn4DTA/+ mice (0.35 ± 0.04 cycles/degree) exhibited spatial frequency intermediate to WT and Opn4$^{DTA/DTA}$ mice. B. The visual water task was used to assess visual function WT, Opn4$^{LacZ/LacZ}$, Opn4$^{DTA/+}$, and Opn4$^{DTA/DTA}$ mice. WT and Opn4$^{LacZ/LacZ}$ mice were indistinguishable. Opn4$^{DTA/DTA}$ mice exhibit a significantly lower grating acuity (0.28 ± 0.03 cycles/degree), than WT mice (0.45 ± 0.02 cycles/degree), and Opn4DTA/+ mice (0.38 ± 0.05 cycles/degree) exhibited spatial frequency intermediate to WT and Opn4$^{DTA/DTA}$ mice. *** indicates P<0.0001 with Student's t-test. Error bars represent s.e.m.
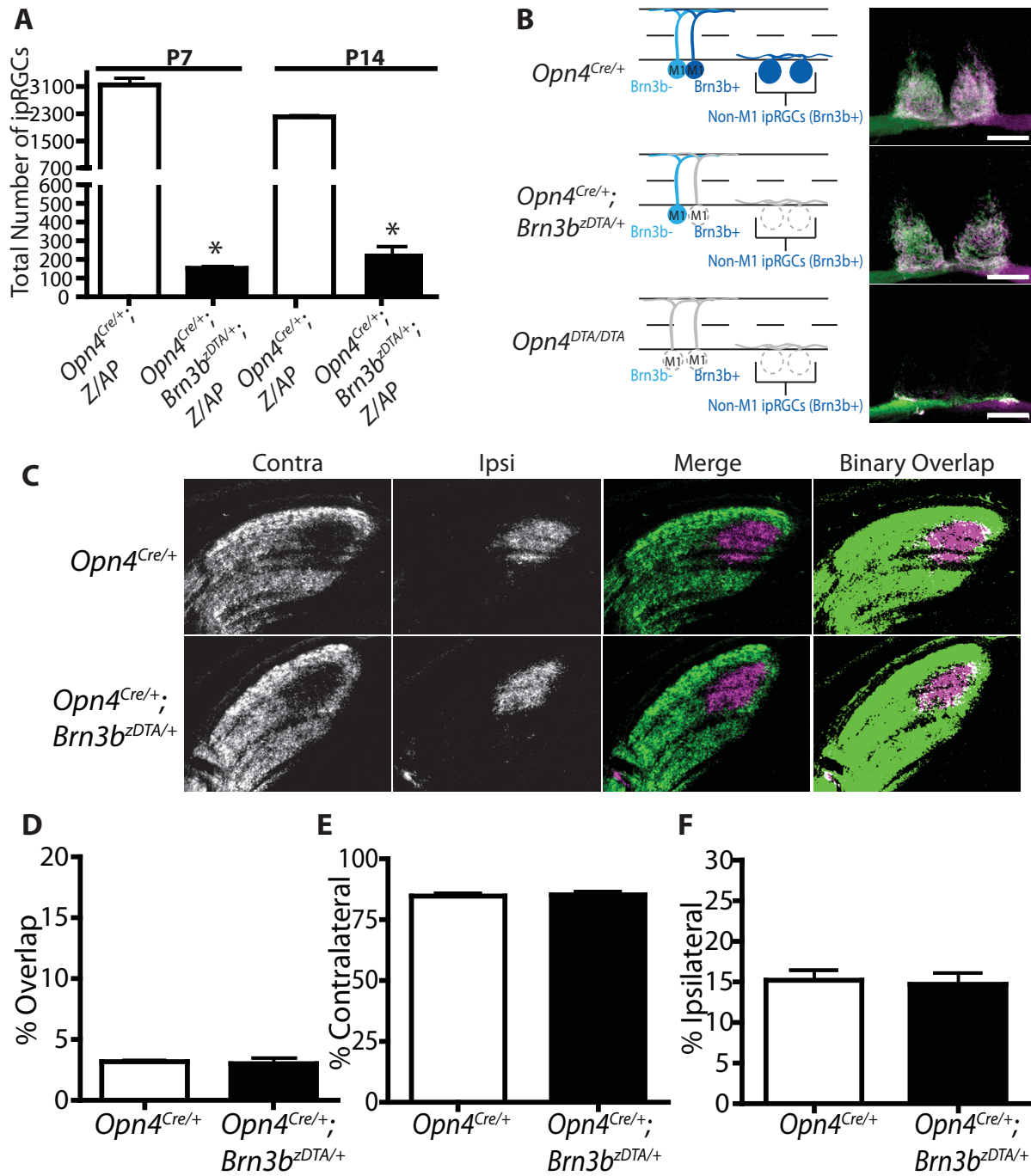
Figure 30. ~200 Brn3b-negative M1 ipRGCs are sufficient for eye-specific axonal segregation in the dLGN

A. Cell counts of total number of ipRGCs in Opn4[Cre/+]; Z/AP (control) and Opn4[Cre/+]; Brn3b[zDTA/+]; Z/AP mice at P7 and P14. ipRGCs were identified by AP staining. In Opn4[Cre/+]; Brn3bzDTA/+; Z/AP mice, there was a significant loss of ipRGCs by P7 (Opn4[Cre/+]; Z/AP, 2563 ± 798 cells vs. Opn4[Cre/+]; Brn3b[zDTA/+]; Z/AP, 154 ± 25 cells) and no further loss at P14 (Opn4[Cre/+]; Z/AP, 2180 ± 86 cells vs. Opn4[Cre/+]; Brn3b[zDTA/+]; Z/AP, 240 ± 43 cells) suggesting that the loss of all but ~200 ipRGCs is complete by P7. ** indicates $P<0.001$ by one-way ANOVA with Tukey post-hoc analysis. B. Total retinal innervation of the SCN visualized with Alexa Fluor 594- (purple) and 488-(green) conjugated CTB in Opn4[Cre/+], Opn4[Cre/+]; Brn3b[zDTA/+], and Opn4[DTA/DTA] mice. C. RGC axonal innervation of the adult dLGN. Alexa Fluor 594- (purple) and 488-(green) conjugated CTB were injected into the right and left eye respectively to label RGC projections in adult Opn4Cre/+(control) and Opn4Cre/+; Brn3bzDTA/+ mice. Images are of the right dLGN. The rightmost images represent a binarized version of the merged images to visualize the overlap between contralateral and ipsilateral RGC projections. Representative images were taken from the same region of the dLGN as presented in (Figure 25). D-F. Eye-specific axonal segregation within dLGN in Opn4[Cre/+] (control) and Opn4[Cre/+]; Brn3b[zDTA/+] mice. Quantification was performed as in (Figure 24D-F) and (Figure 26B-D). There was no significant difference between Opn4[Cre/+] and Opn4[Cre/+]; Brn3b[zDTA/+] mice in the percentages of dLGN represented by overlapping pixels, ipsilateral pixels, and contralateral pixels. Indicating that only ~200 M1 ipRGCs are sufficient for modulating the refinement of RGCs projections. Student's t-test. Error bars represent s.e.m.

(predominantly to the SCN) and are sufficient for circadian photoentrainment (Chen et al., 2011). The other M1 ipRGCs as well as all non-M1 ipRGCs express Brn3b and can be selectively ablated by crossing *Opn4^{Cre/+}* mice with *Brn3b^{Z-DTA/+}* mice, in which a floxed stop cassette followed by DTA has been inserted into the *Brn3b* locus (Mu et al., 2005). In *Opn4^{Cre/+};Brn3b^{Z-DTA/+}* offspring, DTA is expressed only in cells in which both the *Brn3b* and *Opn4* promoters are active; thus, Brn3b-positive ipRGCs are killed, while Brn3b-negative ipRGCs and all conventional RGCs are spared (Chen et al., 2011) (Table 2).

Despite the substantial ablation of ipRGCs in *Opn4^{Cre/+}; Brn3b^{Z-DTA/+}* mice, the intrinsic circadian period of these mice is indistinguishable from controls (Chen et al., 2011). This is in marked contrast to the lengthened circadian period of *Opn4^{DTA/DTA}* mice (Figure 19A, B). A trivial explanation is that ipRGCs are not ablated developmentally in *Opn4^{Cre/+}; Brn3b^{Z-DTA/+}* mice, essentially making them similar to *Opn4^{aDTA/aDTA}* animals, which show normal circadian period length. To test this, we introduced the *Z/AP* transgene into *Opn4^{Cre/+}; Brn3b^{Z-DTA/+}* mice to label ipRGCs with AP. In the resulting *Opn4^{Cre/+}; Z/AP; Brn3b^{Z-DTA/+}* mice, only ~200 ipRGCs remain at early postnatal stages (P7 and P14, Figure 30A), matching the number in adult animals (Chen et al., 2011). This indicates that ablation of Brn3b-positive ipRGCs in these mice is complete by P7 and the remaining ipRGCs belong to the M1 subtype (Chen et al., 2011). The ablation of ipRGCs in development in the *Opn4^{Cre/+}; Brn3b^{Z-DTA/+}* mice indicates that only ~200 Brn3b-negative M1 ipRGCs are sufficient to set the circadian period.

Based on the innervation pattern of the non-M1 ipRGCs to image forming centers, we expected that *Opn4^{Cre/+}; Brn3b^{Z-DTA/+}* mice, which lose all non-M1 ipRGCs, would show deficits similar to *Opn4^{DTA/DTA}* mice. Strikingly, we found that the organization of retino-

geniculate projections in *Opn4^Cre/+; Brn3b^Z-DTA/+* was indistinguishable from controls. These results are remarkable since the *Opn4^DTA/+* mice have ~500 surviving ipRGCs (only 75 of which are M1) and showed significant impairment of eye-specific segregation (Figure 24 and 26) and visual acuity (Figure 29). Whereas, the *Opn4^Cre/+; Brn3b^Z-DTA/+* mice, which only have ~200 Brn3b-negative M1 ipRGCs projecting to circadian centers, exhibited both normal eye-specific segregation in the dLGN (Figure 30C-E) and normal visual acuity (Chen et al., 2011). These results indicate that a subset of ipRGCs that innervate the circadian clock is sufficient for normal development not only of the circadian system but also of the image-forming visual system (Figure 32), a system with which they have no direct connection (Chen et al., 2011).

DISCUSSION

In this study, we investigated, for the first time, the role of ipRGCs in the development of the circadian and image-forming visual systems. We found that the networks devoted to image-forming vision and the circadian clock are both dependent upon ipRCCs to develop adult attributes. Specifically, contrary to the view that the circadian clock develops autonomously within the SCN, the circadian clock requires light input to acquire normal intrinsic properties. Although light exposure usually occurs during early postnatal stages, the setting of the intrinsic period of the circadian clock can take place even in adulthood and only requires a minimum of 3 hours of light. Furthermore, ipRGCs modulate the dynamics of retinal waves, and they are necessary for the refinement of eye-specific axonal segregation in the dLGN and normal visual acuity. Most surprisingly, a subset of ipRGCs, the Brn3b-negative M1 ipRGCs, which has been known to function as

circadian photoreceptors, is sufficient to modulate the development of both the circadian and image-forming systems.

The geniculate organization and visual acuity are normal in animals that have ~200 Brn3b-negative M1 ipRGCs but lack all other ipRGCs. In *Opn4^{DTA/+}* mice, which have wild-type like circadian photoentrainment and contain ~500 surviving ipRGCs but only 75 M1 ipRGCs, still show deficits in both geniculate organization and visual acuity. Further loss of M1 ipRGCs in *Opn4^{DTA/DTA}* mice, including the Brn3b-negative M1 ipRGCs as is indicated by the lack of any innervation of the SCN, results in more extensive deficits in geniculate organization and visual acuity. These results show that the loss of ipRGCs that project to the dLGN are surprisingly not the cause for the deficits in geniculate organization and visual acuity, but instead the presence of only ~200 Brn3b-negative M1 ipRGCs is sufficient for normal geniculate organization and visual acuity.

The fact that the Brn3b-negative M1 ipRGCs, which do not project to image forming centers of the brain, are sufficient for the development of the image forming system indicates that these cells must have an intra-retinal role. Our recent work (Joo et al., 2013) provides an intriguing clue as to how this intra-retinal regulation could occur. Some ipRGCs have intra-retinal collateral axons branching off the primary axon (Joo et al., 2013). These intraretinal collaterals terminate in the inner plexiform layer, where they could influence bipolar, amacrine or ganglion cells (Joo et al., 2013). Importantly, we show here that intra-retinal collaterals are present by P7 (Figure 31). We provide several mechanistic insights of how these collateral axons could regulate wave dynamics in supplemental text (section 1.3). Regardless, our data show that a single population of merely ~200 M1 ipRGCs are sufficient to both drive the maturation of the circadian clock, a process which is light dependent, as
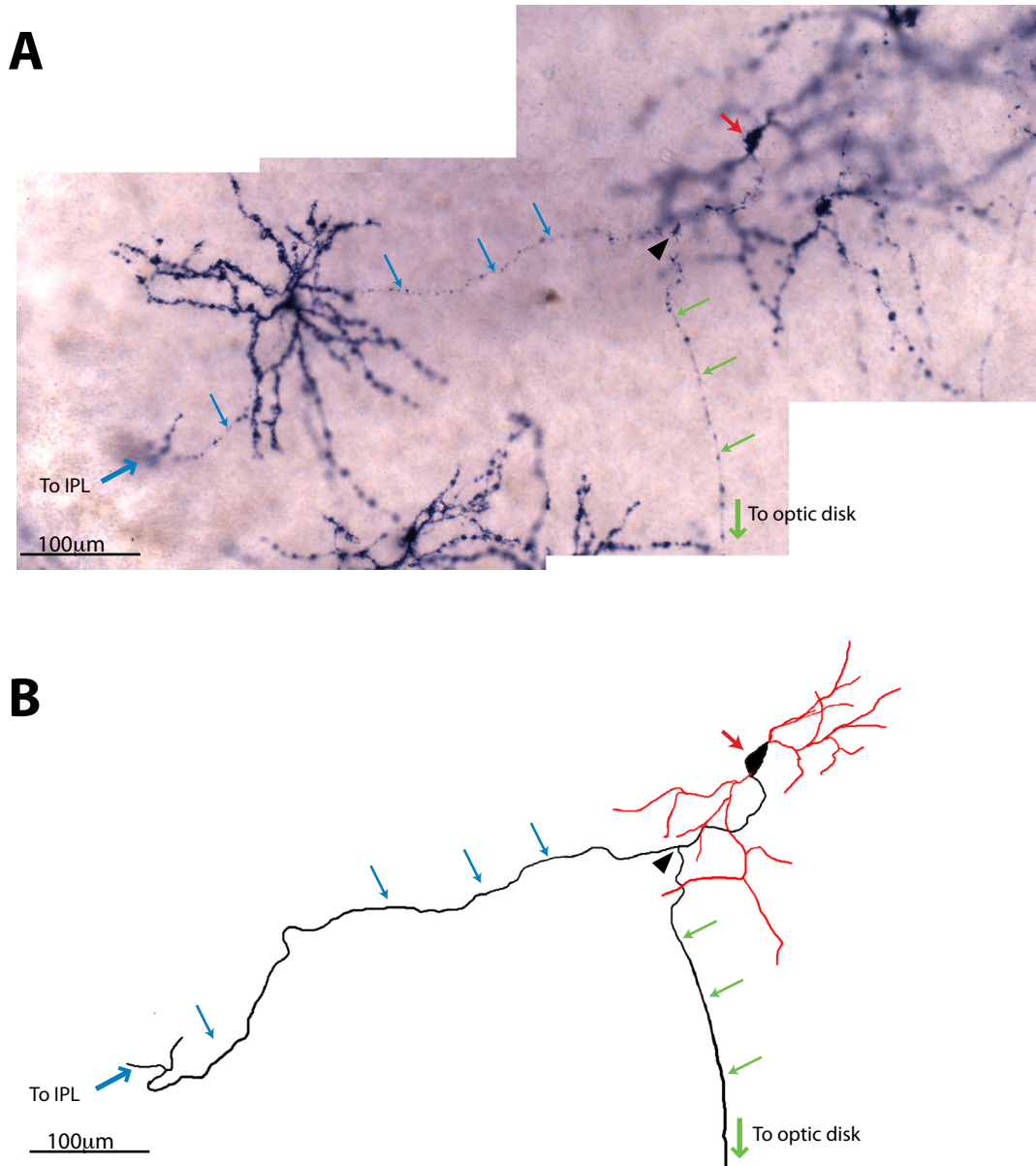
Figure 31: ipRGC intra-retinal axonal collaterals are present by P7

A. Alkaline phosphatase (AP) staining in P7 Opn4$^{CreERT2/+}$ retinas (10) from mice that had been injected with a low dose of tamoxifen at P0, which resulted in sparse labeling of ipRGCs with AP. This image shows an ipRGC axon branching with one branch (green arrows) projecting to the optic disk and the other (blue arrows) to the inner plexiform layer (IPL). Red arrow indicates the cell body, and the black arrowhead indicates the branching point of the axon.

B. A trace of the ipRGC shown in (A) that projects an intra-retinal axon collateral. The trace was compiled from images of consecutive focal planes. Red lines indicate dendrites and black lines indicate the axon.

well as modulate retinal waves and the development of the morphology and function of the image-forming visual system, in a light independent manner.

We surprisingly found that, contrary to the dogma that the circadian clock develops independent of environmental input, light is necessary for setting the intrinsic period of the circadian clock. When WT animals were raised in constant darkness, they exhibited a lengthened circadian period similar to that observed in mice enucleated at P0, or in which DTA killed ipRGCs early in development (Figure 19, 22). Remarkably, when these dark-reared mice were exposed to light for the first time during adulthood, their period length became indistinguishable from mice reared under a 12:12 LD cycle. This result suggests there is no critical developmental window during which the intrinsic properties of the circadian clock must be set by light. Moreover, once animals are exposed to the light, the circadian period is irreversibly set. It will be of interest to investigate the mechanisms by which light detection by ipRGCs induces this permanent change in the circadian clock. Interestingly, we noticed that the phenotype exhibited by dark-reared animals was less penetrant. Though a majority of dark-reared animals (1st round: 9 of 16; 56%; second round 6 of 12 %50) exhibited a lengthened period, the remainder did not (Figure 23). By contrast, virtually all mice enucleated at P0 or suffering early loss of ipRGCs (*Opn4$^{DTA/DTA}$*) exhibited lengthened circadian periods. What accounts for this variability in circadian periods among dark-reared mice? One possible interpretation could be that the process of setting the circadian period is highly sensitive to light. Thus, even brief or dim light exposures would be sufficient. This interpretation is supported by the observation that *Opn4$^{DTA/LacZ}$* animals, which retain weak light responsiveness, have a normal circadian period (Figure 19). In addition, mice that functionally lack all photoreceptors (*GNAT1$^{-/-}$*;

GNAT2^{-/-}; Opn4^{LacZ/LacZ}) free-run regardless of the light-dark cycle, but show a normal

circadian period (23.83 ± 0.14 hours). *GNAT1^{-/-}, GNAT2^{-/-}* mice have been shown to have a

residual ERG response at 3-6 months of age (Allen et al., 2010), providing further evidence

that a weak light response maybe sufficient to set the intrinsic period of the circadian clock,

even when it is not sufficient for circadian photoentrainment. In this study, some dark-

reared animals could have been exposed to, say, very weak light occasionally leaking from

night vision goggles. Regardless of the reason for the variable circadian periods among

dark-reared animals, period resetting is more sensitive to the effects of light than is

circadian photoentrainment. In fact, we showed that merely 3 hours of light was sufficient

to permanently setting the intrinsic period of the circadian clock.

An even more surprising finding was that early genetic ablation of ipRGCs led to

disrupted eye-specific axonal segregation in the dLGN, potentially due to altered dynamics

of spontaneous retinal waves, and reduced visual acuity (Figure 24-27, 29). Retinal waves

are considered a key driver of activity-dependent refinement of developing visual

pathways (Ackman et al., 2012; Chandrasekaran et al., 2005; Feller, 2002, 2009; Firth et al.,

2005; McLaughlin et al., 2003a; Meister et al., 1991; Mrsic-Flogel et al., 2005; Muir-

Robinson et al., 2002; Shatz and Stryker, 1988; Stellwagen and Shatz, 2002; Wong, 1999; Xu

et al., 2011; Zhang et al., 2011). It is therefore plausible that in *Opn4^{DTA/DTA}* mice, the altered

retinal waves led to the disorganization of axonal innervation of the dLGN, which in turn

resulted in the visual acuity deficits.

Our data further implicated the same Brn3b-negative M1 ipRGCs, which have been

viewed primarily as circadian photoreceptors and are sufficient to regulate the

development of the circadian clock, in playing a particularly important role in the
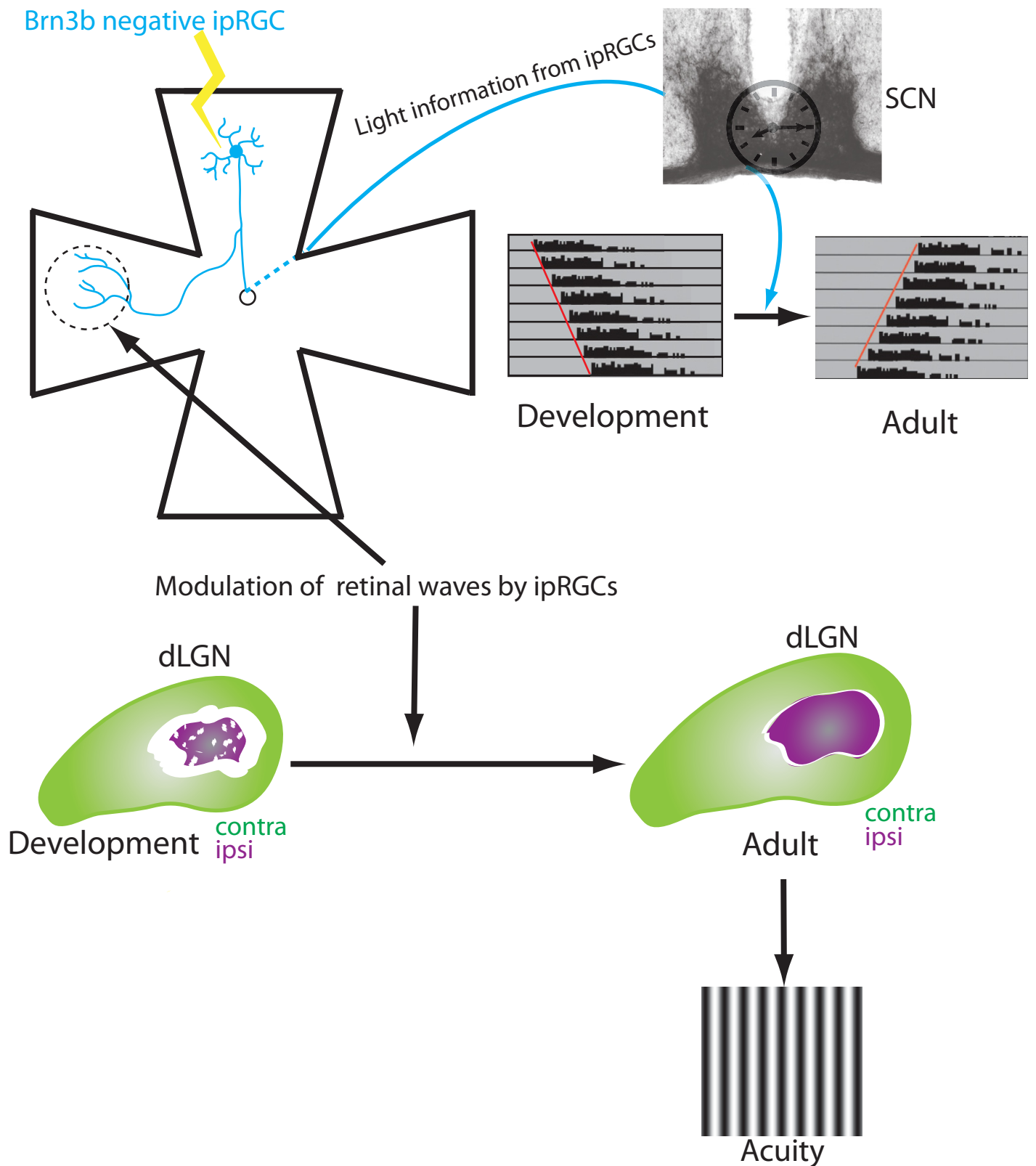
Figure 32. Role of ipRGCs in the development of image and non-image forming vision
ipRGCs are necessary for the proper development of both the circadian and the image-forming visual systems. ~200 Brn3b-negative M1 ipRGCs are sufficient to relay light information that is critical for the establishment of normal intrinsic properties of the circadian clock, including the length of the circadian period. The same ~200 Brn3b-negative M1 ipRGCs are also sufficient for the refinement of eye-specific axonal segregation of RGC projections in the dLGN, potentially by regulating retinal wave dynamics through intra-retinal axonal collaterals.

development of the image-forming visual system. In *Opn4$^{Cre/+}$; Brn3b$^{Z-DTA/+}$* mice, ipRGC subtypes known to innervate the dLGN (i.e., M2-M5 cells) are developmentally ablated (Figure 30A) and only ~200 Brn3b-negative, circadian center projecting-M1 ipRGCs remain (Chen et al., 2011). Many of these 200 Brn3b-negative ipRGCs project intra-retinal axonal collaterals, which provide an obvious potential mechanism for how these few cells could regulate such an extensive phenomena as retinal waves. ipRGCs have previously been shown to have a number of intra-retinal excitatory influences, which could be occurring through intra-retinal collaterals. These roles include effects on dopaminergic amacrine cells in the adult retina (Renna et al., 2011; Zhang et al., 2012; Zhang et al., 2008a), and ipRGCs may modulate signaling in the outer retina (Hankins and Lucas, 2002). Interestingly, dopaminergic amacrine cells have recently been proposed as elements in a circuit by which ipRGCs might influence the waves (Kirkby et al., 2012). Dopaminergic amacrine cells also release GABA (Contini and Raviola, 2003; Hirasawa et al., 2009; Zhang et al.; Zhang et al., 2008a), a fast inhibitory transmitter known to regulate burst activity during spontaneous retinal waves (Fischer et al., 1998). Blockade of GABAergic inhibition and early ablation of ipRGCs produce similar effects on the retinal waves, increasing both the number of spikes per burst and burst duration (Fischer et al., 1998; Sernagor et al., 2003; Wong, 1999; Wong et al., 1998). Though other mechanisms of intra-retinal influence are possible, such as gap junctions, intra-retinal axon collaterals on M1 ipRGCs appear to be a likely mechanism for the intra-retinal signaling that supports ipRGCs' influences on retinal waves and, through them, on the image-forming visual system.

ACKNOWLEDGEMENTS

METHODS

Animal Models:

Animals were housed and treated in accordance with NIH and IACUC guidelines, and used protocols approved by the Johns Hopkins University Animal Care and Use Committee.

Generation of Opn4^{DTA} mice

To generate *Opn4^{DTA}* mice, we used the targeting arms and general strategy detailed in (Ecker et al., 2010; Güler et al., 2008; Hattar et al., 2002). The construct contained a 4.4 kb sequence immediately 5' of the start codon for mouse melanopsin, followed by the coding sequence for diphtheria toxin A (DTA) subunit, an internal ribosomal entry site (IRES), the coding sequence for tauLacZ, and a self-excising neomycin resistance construct (loxP-tAce-Cre-Pol II-Neo-loxP) (Bunting et al., 1999) (Figure 18A). Embryonic stem (ES) cells were first screened for homologous recombination by PCR, and then homologous recombination was confirmed with Southern blot analysis (a restriction digestion with SpeI

resulted in a 10.7kb band for the wild type allele and a 5.3kb band for the recombined

allele) (Figure 18B). The blastocyst injection was performed by the Johns Hopkins

transgenic core facility. The germline transmission was obtained by crossing chimeric

males with C57Bl/6 females. The genotyping was done by PCR. The DTA allele was

detected with the primers: AACTTTTCTTCGTACCACGG (forward) and

ACTCATACATCGCATCTTGG (reverse), and the WT allele was detected with the primers:

CCCCTGCTCATCATCATCTTCTG (forward) and TGACAATCAGTGCGACCTTGGC (reverse).

Alkaline Phosphatase staining:

A cre-mediated alkaline phosphatase (AP) reporter, provided by Tudor Badea in

Jeremy Nathan's lab, was expressed in conjunction with *Opn4^{Cre}* (Ecker et al., 2010). Mice

were deeply anesthetized with 30 ml/kg Avertin and then intracardially perfused with

phosphate-buffered saline for 3 min followed by 40 ml of 4% paraformaldehyde. Brains

and retinas were isolated and post-fixed for 40 min in 4% paraformaldehyde. Brains were

mounted in 3% agarose and then cut into 200μm sections on a vibrating microtome (Vibra-

tome 1000 Plus). Tissue was heat-inactivated for overnight at 65°C. Alkaline phosphatase

histochemistry was performed using NBT/BCIP tablets (Roche) for 2–4 hr in the dark with

constant shaking. Tissue was washed three times with phosphate-buffered saline

containing 0.1% Tween-20 (Sigma-Aldrich). Retinas were mounted immediately and

imaged. Brains were fixed 3 hr in 4% paraformaldehyde at 4°C, then counterstained with

1:5 Fast Red nuclear stain (Vector Labortories) in water for 7 minutes. The sections were

then dehydrated in an ethanol series, and after at least in hour in 100% ethanol, the

sections were cleared in a 2:1 mixture of benzyl benzoate:benzyl alcohol (Sigma-Aldrich),

mounted in glycerol, and imaged immediately. To measure cell density, we counted the

number of ipRGCs, in four representative areas of each retina, and calculated the density of

ipRGCs per mm^2.

Retinal wave recordings:

Mice were shipped overnight at postnatal day 5 (*Opn4$^{DTA/DTA}$* from Johns Hopkins

University and wild-type control mice from Jackson Laboratories). All procedures

involving the use of animals were in accordance with the National Institutes of Health and

approved by the Brown University Institutional Animal Care and Use Committee. Upon

arrival at Brown University, the P6 mice were sacrificed via a lethal intraperitoneal

injection of Beuthanasia. As previously described, retinas were extracted and placed

ganglion-cell side down on the array under dim red light. The retinas were continuously

superfused with oxygenated Ames solution maintained at 36-37°C, and were kept in

constant darkness. Recordings were made after at least 30 minutes of dark adaptation.

The raw analog data was digitized using MC Rack software (Multi Channel Systems)

before being filtered. Further processing was done in OfflineSorter (Plexon Inc.). In order to

determine the number of neurons being sampled by each electrode, we filtered the raw

digitized data using a 125 Hz high-pass filter. A threshold of 5 standard deviations from the

baseline voltage was used as the criterion for a spike. The candidate spikes were then

sorted using OfflineSorter (Plexon Inc.) for the first two principal components of the

waveforms, using a standard T-distribution E-M distribution (Shoham et al., 2003). Cluster

analysis was then performed with a manually adjusted Degrees of Freedom multiplier

introduced in OffineSorter. Spikes appearing within a 1 msec window on 70% of channels were assumed to be artifacts (caused by bubbles or other disturbances) and were discarded. Only electrodes sampling spikes from a single cell were used for further analysis.

Spike times were extracted from the digitized data and exported to Microsoft Excel. As described by (Renna et al., 2011), the spikes were summed into bins of 250 msec and collated into a list of presumed wave-associated bursts. Bursts were considered to begin when the firing rate exceeded twice the channel's average firing rate for more than 500 msec, and to end when the firing rate fell below baseline for more than 1 sec. The macro identified probable burst events. A small percentage of bursts required a manual adjustment to the start and/or end time to more accurately reflect the criteria set for the start and end of the burst. Finally, verification of the bursts was made by reviewing the raw data (on MC Rack) and by implementing the following criteria: a burst was considered wave-associated if it coincided with bursts on two adjacent electrodes; if not, it was disregarded. Data from electrodes that sampled less three waves or that averaged fewer than 15 spikes per wave were discarded. This was done in order to eliminate electrodes with poor contact with the retina, as often occurs due to imperfectly flat tissue. Standard student t-tests were performed on the analyzed data.

Cholera toxin injections:

Mice used to examine central projections at P8 were born and raised in continuous darkness. At P7, mice were anaesthetized on ice, and ocular injections of contrasting fluorescent anterograde tracers (cholera toxin subunit B (CTB)-Alexa-488 and CTB-Alexa-

594) were made. At P8 mice were perfused with 4% PFA and the tissue was harvested. 50 µm sections were taken of the brain using a vibratome.

Mice used for examination of adult central projections were raised in a standard 12:12 LD cycle. Mice were anaesthetized with 20mL/kg of Avertin. Eyes were injected intravitreally using a glass pipet with approximately 2µl of cholera toxin B subunit conjugated with Alexa Fluor 488 or Alexa Fluor 555 (Invitrogen) using a Harvard Apparatus HL-190 picospritzer. CTB-488 was used at a concentration of 6.25µg/µL and CTB-594 was used at 5µg/µL for all injections (Speer et al., 2010). Three days after injection, mice were perfused with 4% PFA, and brains were isolated, cryoprotected in 30% sucrose, frozen in OCT, and 40µm sections we taken using a cryostat. Sections were dried overnight, mounted in VectaShield, and imaged on a Zeiss Imager M1 upright epifluorescence microscope (AxioVision). Retinas were also dissected, mounted in vectashield, and examined for good injection quality.

Quantification of eye-specific segregation:

Quantifications were performed with the analyzer blinded to the genotypes being measured.

Percent overlap between contralateral and ipsilateral projections:

40µm serial sections were taken spanning the dLGN. Images were taken of every section containing the dLGN. In ImageJ, for each image, a background threshold was determined by measuring the maximum intensity of pixels in regions of the section that contained no retinal innervation. Each image was binerized at this intensity threshold. Pixels from contralateral fibers were psedo-colored red and pixels from ipsilateral fibers were psedo-

colored green. The whole dLGN was selected. Percent overlap represents ((number of yellow pixels/total number of pixels)*100)), percent ipsilateral represents ((number of green pixels/total number of pixels)*100)), and percent contralateral represents ((number of red pixels/total number of pixels)*100))(Demas et al., 2006). Averages presented in bar graphs represent all sections from the dLGN pooled, and the distribution of segregation throughout the dLGN is shown in Figure 25.

Virtual optomotor system

When using the virtual optokinetic system (Douglas et al., 2005) we placed individual mice in a box created using four computer screens (Figure 29), which display sine wave gratings that move to create virtual cylinder. If mice can see the gratings, they track the moving bars by turning their head. To obtain an estimate of visual acuity using this setup, we increased the spatial frequency (SF) of the gratings until the mice no longer tracked the movement of the gratings.

The visual water task

In the visual water task (Prusky et al., 2000), mice are place in a trapezoidal shaped maze that contains water and has a divider down the middle to create two arms. At the end of one arm a gray panel in displayed, and in the other arm sine wave grating is displayed (Figure 29). Mice were trained, using gratings with a low SF, to associate the gratings with a hidden platform that allows them to escape from the water. The location of the grey panel and gratings with the hidden platform were moved between the arms in a pseudorandom pattern that mice cannot memorize. Any entrances into the arm containing

the grey panel were recorded as incorrect, after the mice could reliably swim to the

platform with greater that 90% accuracy, the SF of the gratings was increased. An animal's

threshold was considered to have been reached once they failed to have better than 70%

accuracy out of 10 trials. This threshold was confirmed by retesting the previous SF, which

is 0.02cycles/degree lower, and then retesting the spatial frequency that the mice initially

failed. If the mouse's behavior repeated where they could see the lower SF, but not one

increment higher, then the visual acuity of that mouse was recorded as the last spatial

frequency where they had better than 70% accuracy.

Enucleations:

In order to remove the eyes, P0 mice were placed on ice for 2 minutes, and then a 1-

2mm incision was made across each eyelid using a sterile scalpel blade. The scalpel blade

was then used to puncture the eyes and forceps were used to pull the eyes free of the

orbitals. P60 mice were first anesthetized with intraperitoneal injection of 20 mL/kg of

Avertin. Fingers were placed on either side of the eye causing it to bulge, a curved pair of

scissors was placed between the eye and the skin, and the optic nerve was cut. Bleeding

was controlled by orbital pressure. The animal was monitored over the next several days

for signs of infection.

Wheel Running Behavior:

Mice were placed in cages with a 4.5-inch running wheel, and their activity was

monitored with VitalView software (Mini Mitter), and cages were changed at least every 2

weeks. All free-running periods were calculated with ClockLab (Actimetrics)

WT, *Opn4$^{LacZ/LacZ}$*, *Opn4$^{DTA/+}$*, *Opn4$^{DTA/LacZ}$*, *Opn4$^{aDTA/aDTA}$*, and *Opn4$^{DTA/DTA}$* mice were placed in 12:12 LD for 10 days followed by constant darkness for 14 days. For phase-shifting experiments, each animal was exposed to a light pulse (500 lx; CT16) for 15 min, after being in constant dark for 14 days.

P0 and P60 ennucleated animals were placed in 12:12 LD for 24 days followed by constant darkness for 14 days.

Dark-reared animals and control mice (raised in 12:12 LD) were placed in constant darkness without any exposure to light. Wheel running behavior was recorded in constant darkness for 1-3 months. Mice were then either given a 3 hour light pulse or placed in 12:12 LD for 14 days and then presented with a 6-hour shift and allowed to re-entrain for 14 days. Mice were then returned to constant darkness for 1 month.

X-gal staining:

Mice were deeply anesthetized with 30 ml/kg Avertin followed by cervical dislocation. Eyes were isolated and fixed in 4% paraformaldehyde for 10 minutes. Retinas were dissected out and then incubated in buffer B (100 mM phosphate buffer at pH 7.4, 2 mM MgCl$_2$, 0.01% sodium deoxycholate, 0.02% IGEPAL) then stained for 3 days in buffer B plus 5 mM potassium ferricyanide, 5 mM potassium ferrocyanide and 1 mg/ml X-gal as described in (Hattar et al., 2002).

Hematoxilin and Eosin Staining

Animals were anesthetized with 30 ml/kg Avertin, and eyes were removed fixed in 4% PFA for 1 hour. Retinas were dissected in PBS, placed in cartridges (Tissue-Tek Biopsy Uni-Cassette), and processed and embedded in paraffin overnight. Eyecups were sectioned at 6

μm. Resulting sections were deparaffinize by immersion in 2 changes of xylene for 10 minutes each. Sections were then rehydrated in descending series of ethanol ending in water for 5 minutes. Sections were stained with hematoxylin for 30 sec, washed with tap water for 10 dips, placed briefly in 0.1% sodium bicarbonate, and then rinsed in clean tap water for 10 dips. Sections were rinsed in 70% ethanol for 5 dips and stained in eosin for 20 sec. Sectioned were dehydrated with an ascending series of ethanol, ending with two washes of 100% ethanol. Sections were placed in 2 washes of xylene (5 minutes each), and mounted in Permount.

Immunohistochemistry

Whole eyes were fixed for 15 minutes in 2% paraformaldehyde (PFA) diluted in PBS and were then dissected to remove the cornea and lens. Whole eyecups were fixed for additional 45 minutes in 2% PFA diluted in PBS. Further dissection was done to release the retinas from the RPE, and 4 nicks were made so that the retina would lay flat. Whole retinas were blocked in 500μL of PBS containing 0.3% Triton X100 and 3% goat serum for 2 hours at RT. Either mouse anti-Brn3a (Millipore, cat #AB5945) (1:250), rabbit anti-γ13 (generously provided by Robert Margolskee)(1:500), rabbit anti-calretinin (Swant, cat #CR 7699/3H)(1:500), goat anti-ChAT (Millipore, cat #Ab144p) (1:200), or mouse anti-SMI-32 (Covance, cat #SMI-32R) (1:500) was diluted in blocking solution and incubated overnight at 4°C. Retinas were washed 10 minutes in 3 changes of PBS, then placed in 1:500 Alexa Fluor secondary antibody (Invitrogen) overnight at 4°C. Retinas were washed as above and mounted flat on slides in VectaShield (Vector Labs). To measure cell density was measured

by counting cells in four representative areas of each retina, and density was calculated as the number of cells per mm^2.

PNA staining

Mice were deeply anesthetized with 30ml/kg Avertin followed by cervical dislocation. Eyes were isolated and fixed in 4% PFA for 1 hour. Retinas were dissected out and then incubated for 2h in Alexa 488-conjugated lectin peanut agglutinin (PNA) (Invitrogen cat# L21409) diluted 1:200 in PBS with 0.3% Triton X100 and 3% goat serum. Retinas were then washed in PBS and mounted in VectaShield (Vector Labs)(Wassle et al., 2009).

In-situ hybridization

Mice were anesthetized with a ketamine/xylazine mixture before transcardially perfusing with 0.9% saline followed by 4% PFA in PBS, pH 7.4. All tissues were post fixed in 4% PFA overnight at 4ºC, cryoprotected in 20% sucrose in PBS, frozen in O.C.T. Compound Embedding Medium (Tissue-Tek), and stored at -75ºC. Serial sections (20µm) were cut on a Hacker cryostat and thaw mounted on Superfrost Plus slides (Thermo Fisher Scientific). Five adjacent sets of sections were prepared from each postnatal age and stored at –20ºC.

Plasmids for *in situ* hybridization probes were acquired from published sources (Burns et al., 2008; Gray et al., 2004; Zhang et al., 2008b) or purchased from Open Biosystems. Gene fragments from verified plasmids were linearized by direct amplification by sequence or vector-specific PCR. Digoxigenin (DIG)-labeled anti-sense and sense RNA probes were

made using PCR products as template and T7, T3, or SP6 RNA polymerases (Roche). cRNA probes were purified using Quick Spin columns (Roche) and quantified by spectrophotometry. Probes were used at a concentration of 1-2µg/ml. Sense counterparts of all probes were tested to ensure probe specificity.

Slides were immersed in 4% PFA, permeabilized with proteinase K, returned to 4% PFA before being washed in 0.1 M triethanolamine-HCl with 0.25% acetic anhydride. Once blocked in hybridization buffer at 65ºC slides were incubated in hybridization buffer containing 1-2 µg/ml DIG-labeled anti-sense cRNA overnight at 65ºC. Slides were then washed in 2XSSC buffer at 62ºC, washed in 0.2XSSC at 65ºC, blocked with 10% normal horse serum (NHS) in 0.1M PBS, and incubated in alkaline phosphatase labeled anti-DIG antibody (1:2000 in 10% NHS; Roche) overnight. Sections were washed and color was visualized using Nitro blue tetrazolium and 5-Bromo-4-chloro-3-indolyl phosphate (Roche). Staining was stopped after visual inspection. Sections were washed, fixed in 4% PFA, and coverslipped in 90% glycerol, Vectashield Mounting Medium (Vector Laboratories), or UltraCruz Mounting Media with DAPI (Santa Cruz Biotechnology).

Images were acquired using a Nikon Eclipse 90i microscope, Photometrics Coolsnap HQ2 camera with a Prior Scientific ProScan II motorized translation stage, and acquired in Volocity (PerkinElmer Life and Analytical Sciences). Images were exported as 8bit JPEG or TIFF files. All images were adjusted for clarity by filtering and/or modifying levels, as necessary, in Photoshop (Adobe Systems).

Quantification of eye-specific segregation

'Mixed pixels'

A complete series of 50 μm sections spanning the dLGN were digitally imaged with settings (gain, exposure time and gamma level) that were identical for all photomicrographs and for both tracers for all mice. Sections from each brain were aligned to ensure all images analyzed were within the same region of the dLGN. We were blind to genotype until data were processed and analyzed, as described by (Renna et al., 2011). Briefly, 10 sections per p8 mouse and 15 sections per adult mouse, per dLGN hemisphere were selected and R-values were calculated for all pixels within each dLGN. Next, 8 representative dLGN sections from the WT mice were used to calculate the unsegregated pixel values from each dLGN. This was done by selecting a region of interest that was maximally innervated by the contralateral eye and a region of interest that was maximally innervated by the ipsilateral eye. The R-distribution for maximally ipsilateral segregated pixels and maximally contralateral pixels were calculated and averaged across all 8 dLGN sections. Pixels with an R-value less than 99.9% of the maximally contra segregated pixels and more than 99.9% of all maximally ipsilateral segregated pixels were termed unsegregated pixels.

Variance of R-distribution

As described by (Torborg and Feller, 2004), we calculated the variance for each dLGN R-distribution. Larger variances are indicative of a wider range of values (more ipsilateral dominant pixels and contralateral dominate pixels), and thus, fewer pixels with more balanced left and right eye input.

Reconstruction of retinal innervation of the SC

Similar to (Fernandez et al., 2012), Coronal sections were used for the SC reconstruction using Matlab (Math Work). For each section, the retino-recipient SC was outlined, and the total retinotopic area was calculated. Images were converted to 8-bits of grey scale and the optic density of CTB-staining was calculated. The total length was measured and divided in bins (4 μm) from the medial to lateral region. The CTB density was obtained by dividing the total pixel area by CTB+ pixels. Finally, a colorimetric thermal representation was applied (from 0% = blue to 100% = red). All sections containing the SC were used for a final reconstruction of the retinal projection to the SC.

CHAPTER 4: PHOTOTRANSDUCTION IN IPRGCS

The contents of this chapter have been published in PLoS ONE

INTRODUCTION

Intrinsically photosensitive retinal ganglion cells (ipRGCs) comprise a distinct subset of retinal ganglion cells (RGCs) and express the photopigment melanopsin (*Opn4*) (Provencio et al., 1998). ipRGCs constitute the sole conduit of light information from the retina to non-image forming visual centers in the brain and are responsible for driving a variety of behaviors (Güler et al., 2008; Hattar et al., 2003). These behaviors include circadian photoentrainment, which is the process by which the circadian clock is aligned to the environmental light-dark cycle, and the pupillary light reflex (PLR), in which the area of the pupil changes in response to changes in light intensity.

Despite the well-established role for ipRGCs and melanopsin in the regulation of non-image forming visual functions, little is known about the molecular components of melanopsin phototransduction. Previous research has suggested that ipRGCs likely utilize a phototransduction pathway similar to that used in *Drosophila* microvillar photoreceptors (Graham et al., 2008; Provencio et al., 1998), in which the activated opsin stimulates a $G_{q/11}$ protein. In *Drosophila*, the α-subunit of the $G_{q/11}$ protein activates phospholipase C-β (PLC-β), which results in the opening of TRP and TRPL channels allowing Na^+ and Ca^{2+} to flow into the cell resulting in depolarization of the rhabdomere in response to light (Hardie, 2001; Huang et al., 2010).

Homologs of the components of the *Drosophila* phototransduction pathway are found in mice. Specifically, there are four $G_{q/11}$ genes (*Gnaq, Gna11, Gna14,* and *Gna15*), four *Plc-β* genes (*Plc-β1 – 4*), and seven *Trpc* channel genes (*Trpc1-7*). The tandemly duplicated *Gna15* and *Gna11* genes are linked to mouse chromosome 10 (Davignon et al., 1996; Wilkie et al., 1991), and *Gnaq* and *Gna14* colocalize to mouse chromosome 19 (Offermanns et al., 1998). To

date, there have been several electrophysiological studies implicating $G_{q/11}$, *Plc-β*, and *TrpC* genes in ipRGC phototransduction(Graham et al., 2008; Perez-Leighton et al., 2011; Xue et al., 2011). However, there have been no functional studies investigating the identity of the $G_{q/11}$ protein utilized by melanopsin *in vivo* or any studies of the effects of the loss of any presumptive ipRGC phototransduction genes on behavior. In this study, we sought to determine the identity(ies) of the $G_{q/11}$ protein(s) utilized for melanopsin phototransduction *in vivo*.

We performed single-cell RT-PCR on individual ipRGCs to determine which of the genes were expressed in ipRGCs and if there was heterogeneity in their expression among the ipRGC population. Similar to previous studies, we found that the majority of ipRGCs express both *Gna11* and *Gna14*, but not *Gnaq* or *Gna15*. Since loss of the melanopsin protein results in well-characterized deficits in the pupillary light reflex and circadian behaviors, we examined these non-imaging forming visual functions in $Gna11^{-/-}$; $Gna14^{-/-}$ (*Gna11*; *Gna14* DKO) mice and $Gnaq^{flx/flx}$; $Gna11^{-/-}$; $Opn4^{Cre/+}$ (*Gnaq*; *Gna11* DKO) mice as well as several single $G_{q/11}$ gene knockouts (Davignon et al., 2000; Offermanns, 2003; Offermanns et al., 1998; Wettschureck et al., 2001). All genotypes examined exhibited non-image forming visual functions indistinguishable from WT. Furthermore, multielectrode array recordings revealed no deficits in ipRGC light responses in *Gna11*; *Gna14* DKO animals. Contrary to previous work, this study indicates that ipRGCs may be able to utilize a $G_{q/11}$-independent phototransduction cascade *in vivo*.

RESULTS

Gna11 and *Gna14* are expressed in ipRGCs
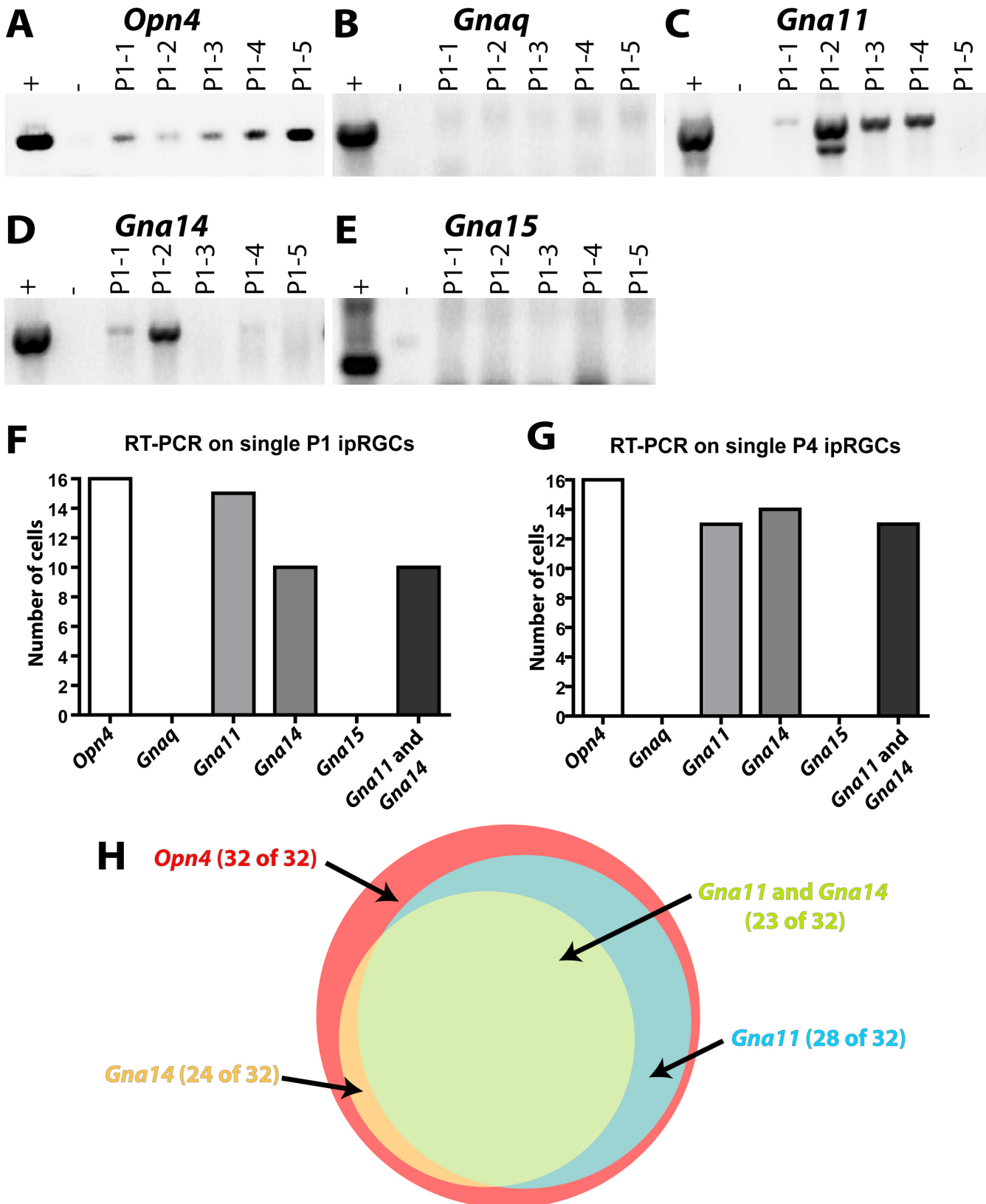
Figure 33: Gna11 and Gna14 are expressed in ipRGCs, often in combination
A-E. Representative images of RT-PCR analysis of single ipRGCs for Opn4, Gnaq, Gna11, Gna14, and Gna15. All representative gels show RT-PCR analysis of single ipRGCs taken from P1 Opn4Cre/+; Z/EG mice. Each lane represents one cell, the positive control is whole retinal RNA, and the negative control is water. F-G Summary of expression of Gq/11 family members in the 16 ipRGCs obtained from P1 and P4 Opn4Cre/+; Z/EG mice. All cells expressed melanopsin. 15 cells expressed Gna11, 10 of which also expressed Gna14. H. Venn diagram showing the distribution of Gq/11 family member expression in all 32 ipRGCs sampled.

111

Previous reports have shown that $G_{q/11}$ genes are expressed in ipRGCs. However, there has been disagreement regarding which $G_{q/11}$ genes are actually expressed, with one study reporting heterogeneous expression of each of the four $G_{q/11}$ genes and another reporting primarily *Gna14* and some *Gna11* expression (Graham et al., 2008; Siegert et al., 2012). We therefore sought to definitively identify which $G_{q/11}$ genes are expressed in ipRGCs. We isolated individual ipRGCs by dissociating retinas of *Opn4*$^{Cre/+}$ *Z/EG* mice, in which ipRGCs ipRGCs are labeled with GFP, and picking individual ipRGCs with a microneedle. We specifically chose to utilize retinas from P1 and P4 mice since there is GFP labeling of some cones in adult *Opn4*$^{Cre/+}$ *Z/EG* mice (Ecker et al., 2010). By RT-PCR, we confirmed that the 32 isolated cells expressed melanopsin (Figure 33A, F-H), and then screened those 32 melanopsin-expressing cells for the four $G_{q/11}$ genes (Figure 33B-H). 23 of the 32 ipRGCs expressed both *Gna11* and *Gna14*, and an additional 6 cells expressed either *Gna11* or *Gna14* (Figure 33F-H). Neither *Gnaq* nor *Gna15* were detected in any of the melanopsin-expressing cells, and 3 melanopsin-expressing cells had no detectable levels of any $G_{q/11}$ gene (Figure 33F-H).

Loss of $G_{q/11}$ genes does not affect non-image forming visual functions.

Mice that lack melanopsin phototransduction due to loss of melanopsin have several well characterized deficits in non-image forming visual behaviors including defects in the PLR at high light intensities and a deficit in circadian period lengthening in response to constant light. Since *Gna11* and *Gna14* were the only $G_{q/11}$ genes identified as being expressed in ipRGCs and nearly all cells tested expressed at least one, we produced *Gna11*$^{-/-}$; *Gna14*$^{-/-}$ (*Gna11; Gna14* DKO) mice from previously published single knockouts (Dennis and Bradshaw, 2011; Offermanns, 1999, 2003). We recorded the pupillary light reflex of 4-6 month old WT (n = 16),
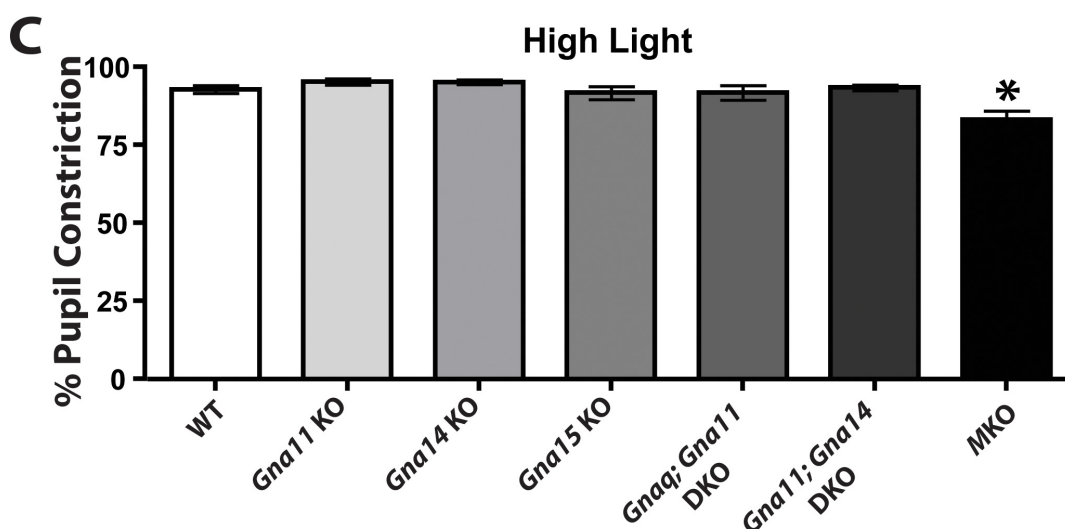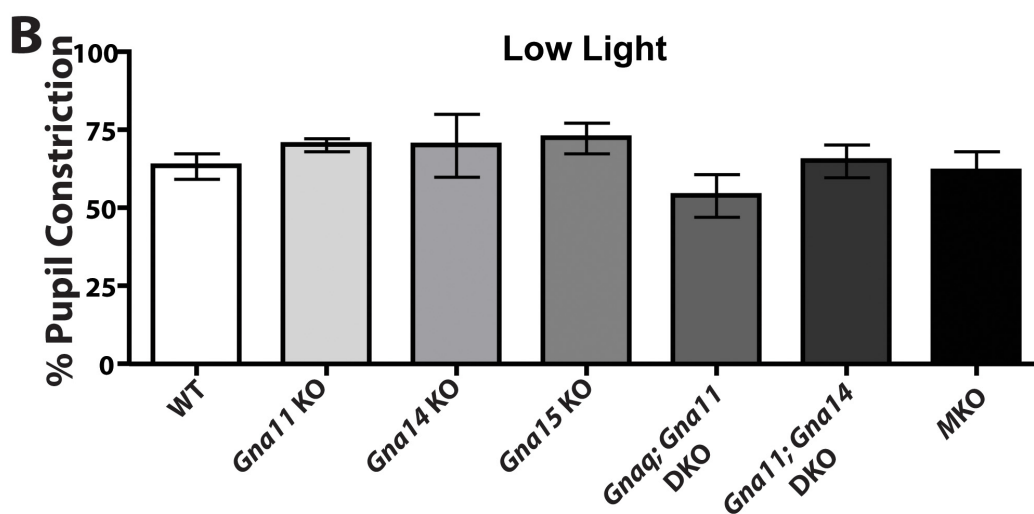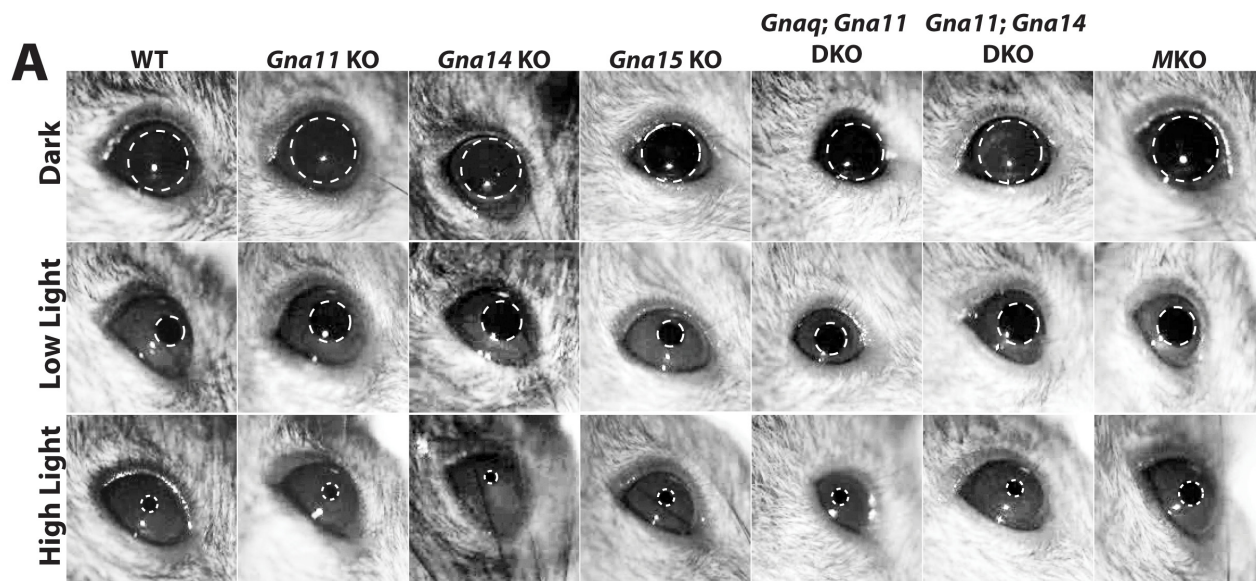
Figure 34: Gq/11 mutant lines exhibit pupillary light reflex indistinguishable from WT
A. Representative images of the pupil constriction in WT (16 animals), Opn4LacZ/LacZ (MKO, 7 animals), Gna11-/- (Gna11 KO, 4 animals), Gna14-/- (Gna14 KO, 5 animals), Gna15-/- (Gna15 KO, 7 animals), Gnaqflx/flx; Gna11-/-; Opn4Cre/+ (Gnaq; Gna11 DKO, 9 animals), and Gna11-/-; Gna14-/- (Gna11; Gna14 DKO, 7 animals) at both high (1.4×10^{16} photons/cm2/sec) and low (7.3×10^{13} photons/cm2/sec) light intensities. B-C. Quantification of the pupillary light reflex at low (7.3×10^{13} photons/cm2/sec) and high (1.4×10^{16} photons/cm2/sec) light intensities. All animals exhibited pupillary light reflex indistinguishable from WT. One-way ANOVA with Tukey post-hoc analysis. Error bars represent s.e.m.
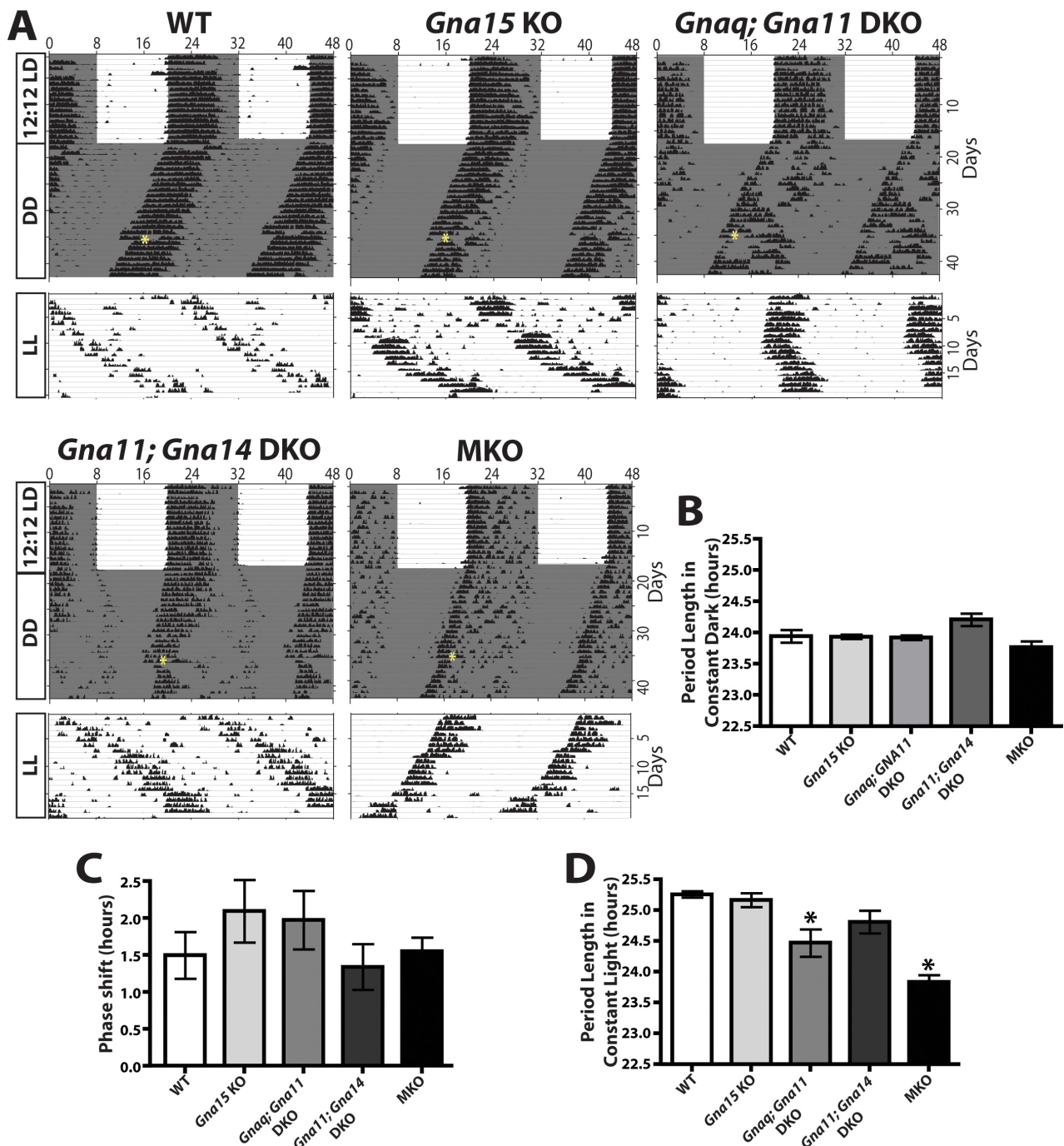
Figure 35: Gq/11 mutant lines exhibit circadian behaviors indistinguishable from WT

A. Representative actograms of wheel running activity from WT (14 animals), MKO (9 animals), Gna15 KO (7 animals), Gnaq; Gna11 DKO (8 animals), and Gna11; Gna14 DKO (7 animals) mice under a 12:12 LD cycle, constant darkness, and constant light. The white background indicates light, grey background indicates darkness, and the yellow asterisk indicates a 15-minute light pulse at circadian time (CT) 15. All mice photoentrained to the LD cycle. B. Quantification of free-running period under constant dark conditions. All animals exhibited circadian periods indistinguishable from WT. One-way ANOVA with Tukey post-hoc analysis. Error bars represent s.e.m. C. Quantification of phase shifting to a 15-minute light pulse given at CT 15. All animals exhibited phase shifting indistinguishable from WT. One-way ANOVA with Tukey post-hoc analysis. Error bars represent s.e.m. D. Quantification of free running period under constant light. As previously reported, MKO mice exhibited reduced lengthening of their circadian period under constant light conditions. Gnaq; Gna11 DKO exhibited a slight reduction in the lengthening of their circadian period in constant light, and their period length was significantly different from both WT and MKO. Gna15 KO and Gna11; Gna14 DKO exhibited lengthened periods that were indistinguishable from WT. One-way ANOVA with Tukey post-hoc analysis. Error bars represent s.e.m.

Opn4^{LacZ/LacZ} (MKO; n =, 7), *Gna11^{-/-}* (*Gna11* KO; n = 4), *Gna14^{-/-}* (*Gna14* KO; n = 5), *Gna15^{-/-}* (*Gna15* KO; n = 7), *Gnaq^{flx/flx}*; *Gna11^{-/-}*; *Opn4^{Cre/+}* (*Gnaq; Gna11* DKO; n = 9), and *Gna11^{-/-}*; *Gna14^{-/-}* (*Gna11; Gna14* DKO; n = 7) at both low and high light intensities (Figure 34). Consistent with previous studies (Lucas et al., 2003), MKOs exhibited deficits at high light intensities. Surprisingly, all mice mutant for $G_{q/11}$ genes were indistinguishable from WT animals at both low and high light intensities (Figure 34).

We also recorded wheel-running activity in 4-6 month old WT (n = 14), MKO (n = 9), *Gna15* KO (n = 7), *Gnaq; Gna11* DKO (n = 8), and *Gna11; Gna14* DKO (n = 7) mice to measure the daily activity rhythms of these mice (Figure 35). We conducted these measurements under three different conditions: a 12:12 light/dark cycle, constant darkness, and constant light. We also administered a 15-minute light pulse in constant darkness to determine the amplitude of the light-evoked circadian phase shifts in each mouse line. All genotypes were able to photoentrain to the 12:12 light/dark cycle. All mutant lines exhibited a normal circadian period under constant darkness (WT: 23.85 ± 0.36 hours, MKO: 23.68 ± 0.26 hours, *Gna15* KO: 23.84 ± 0.08 hours, *Gnaq; Gna11* DKO: 23.83 ± 0.10 hours, and *Gna11; Gna14* DKO: 24.01 ± 0.24 hours) (Figure 35A, B). All mice phase shifted normally to a light pulse presented at CT15. We observed no deficits in phase delay among any genotypes tested (WT: 1.40 ± 0.78 hours, MKO: 1.45 ± 0.49 hours, *Gna15* KO: 1.96 ± 1.04 hours, *Gnaq; Gna11* DKO: 1.85 ± 0.74 hours, and *Gna11; Gna14* DKO: 1.25 ± 0.65 hours) (Figure 35A,C). Melanopsin knockout animals have well-characterized deficits in lengthening their circadian period under constant light (Ruby et al., 2002) that we confirmed here (WT period: 25.08 ± 0.17 hours, MKO period: 23.75 ± 0.28 hours). (Figure 35A, D). In constrast, *Gna15* KOs (24.99 ± 0.28 hours) and *Gna11; Gna14* DKOs (24.66 ± 0.42 hours) were indistinguishable from WT mice. While *Gnaq; Gna11* DKO animals (24.34 ±
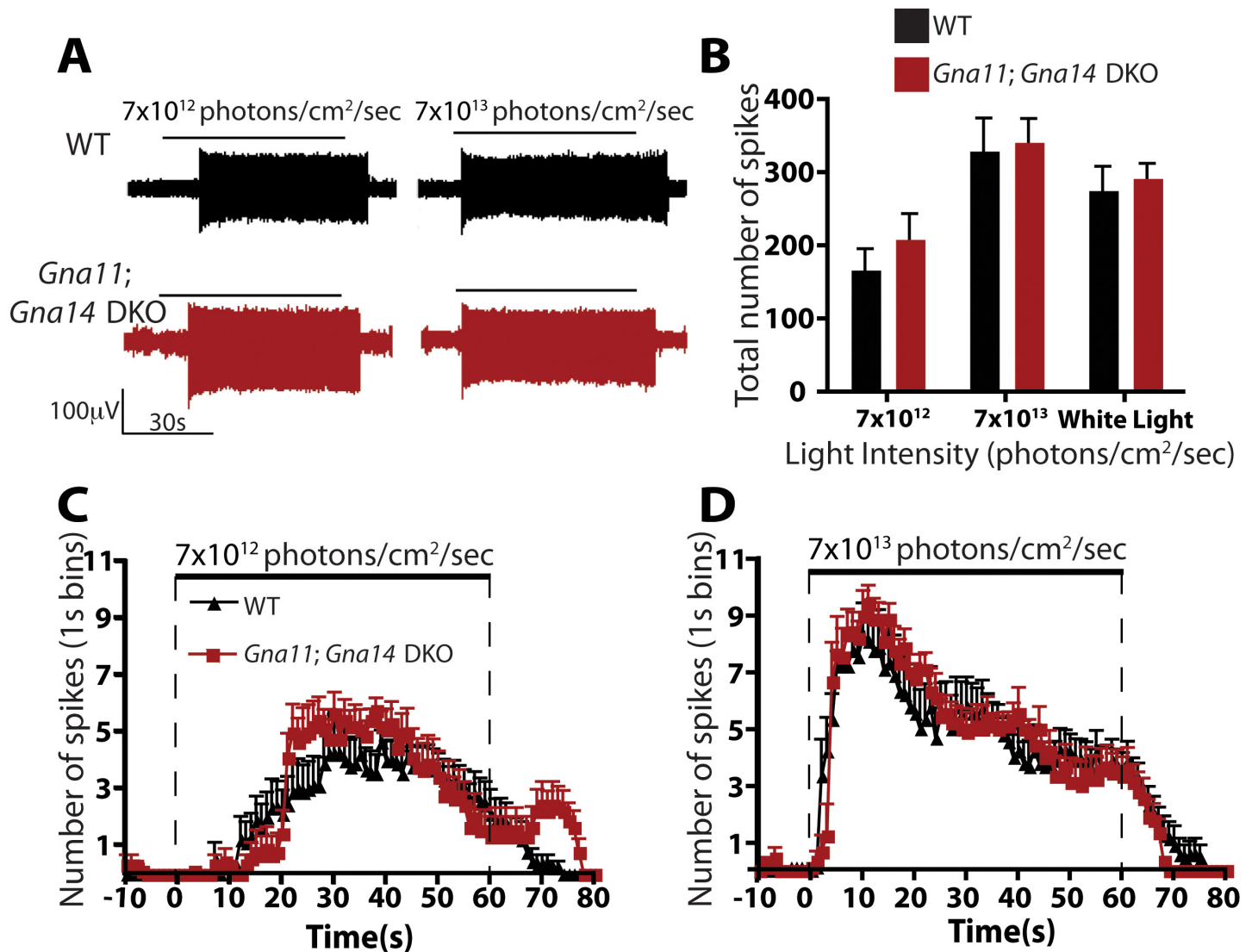
Figure 36: ipRGC intrinsic phototransduction persists in Gna11; Gna14 DKO mice
A. Representative voltage traces for ipRGC intrinsic light responses in WT and Gna11; Gna14 DKO retinas at two 480 nm light intensities (7x1012 and 7x1013 photons/cm2/sec). Horizontal bar represents light stimulation (60 sec). Vertical scale bar is 100 µV.   B. Total number of spikes in ipRGCs light responses to two 480nm light intensities (7x1012 and 7x1013 photons/cm2/sec) and white light (267 mW/cm2). ipRGC light responses in Gna11; Gna14 DKO were indistinguishable from WT. Student's t-test. Error bars represent s.e.m.   C-D. Quantification of the number of spikes, in 1 second bins, during a 60 second pulse of either 7x1012 photons/cm2/sec or 7x1013 photons/cm2/sec 480nm light. Photoresponses in Gna11; Gna14 DKO mice were indistinguishable from WT. Student's t-test. Error bars represent s.e.m.

0.5 hours) did show a significantly shorter period than WT animals, the period was still

significantly longer than MKO animals (Figure 35A, D).

ipRGC light responses persist in *Gna11*; *Gna14* double knockouts

The lack of behavioral deficits in $G_{q/11}$ mutant animals led us to examine whether

melanopsin phototransduction is perturbed at the cellular level in these lines. We therefore

examined the light responses of ipRGCs in isolated retinas of WT and *Gna11; Gna14* DKO mice

using multielectrode array (MEA) recordings. We recorded from retinas of postnatal day 3 mice,

since it has been shown that outer retinal signaling to ganglion cells is not present at early

postnatal ages (Sernagor et al., 2001), and thus ipRGCs constitute the only light-responsive

ganglion cells at this age (Sekaran et al., 2005; Tu et al., 2005). Nonetheless, to guarantee that all

detected light responses were from ipRGCs, we included a cocktail of synaptic blockers in the

Ames' medium to inhibit any glutamatergic, GABAergic, and glycinergic signaling to ipRGCs.

Additionally, we included cholinergic blockers to minimize interference from retinal waves

present at this developmental stage (Sun et al., 2008). Retinas were dark adapted for at least 20

min and then stimulated with diffuse, uniform light of both low (7×10^{12} photons/cm^2 · sec) and

high light intensity (7×10^{13} photons/cm^2 · sec) for 60 sec at 480 nm, the peak wavelength for

melanopsin activation (Berson, 2007; Do et al., 2009). We also stimulated the retinas with bright

white light (267 mW/cm^2). The retinas were allowed to readapt to dark for 5 min between

stimulations. Figure 36A shows representative voltage traces of typical ipRGCs in WT and

Gna11; Gna14 DKO mice at both low and high light intensity. We found that *Gna11; Gna14*

DKO ipRGCs were indistinguishable from the WT controls. ipRGCs in both WT and *Gna11;*

Gna14 DKO mice responded to increasing light intensities with increased spiking (Figure 36B)
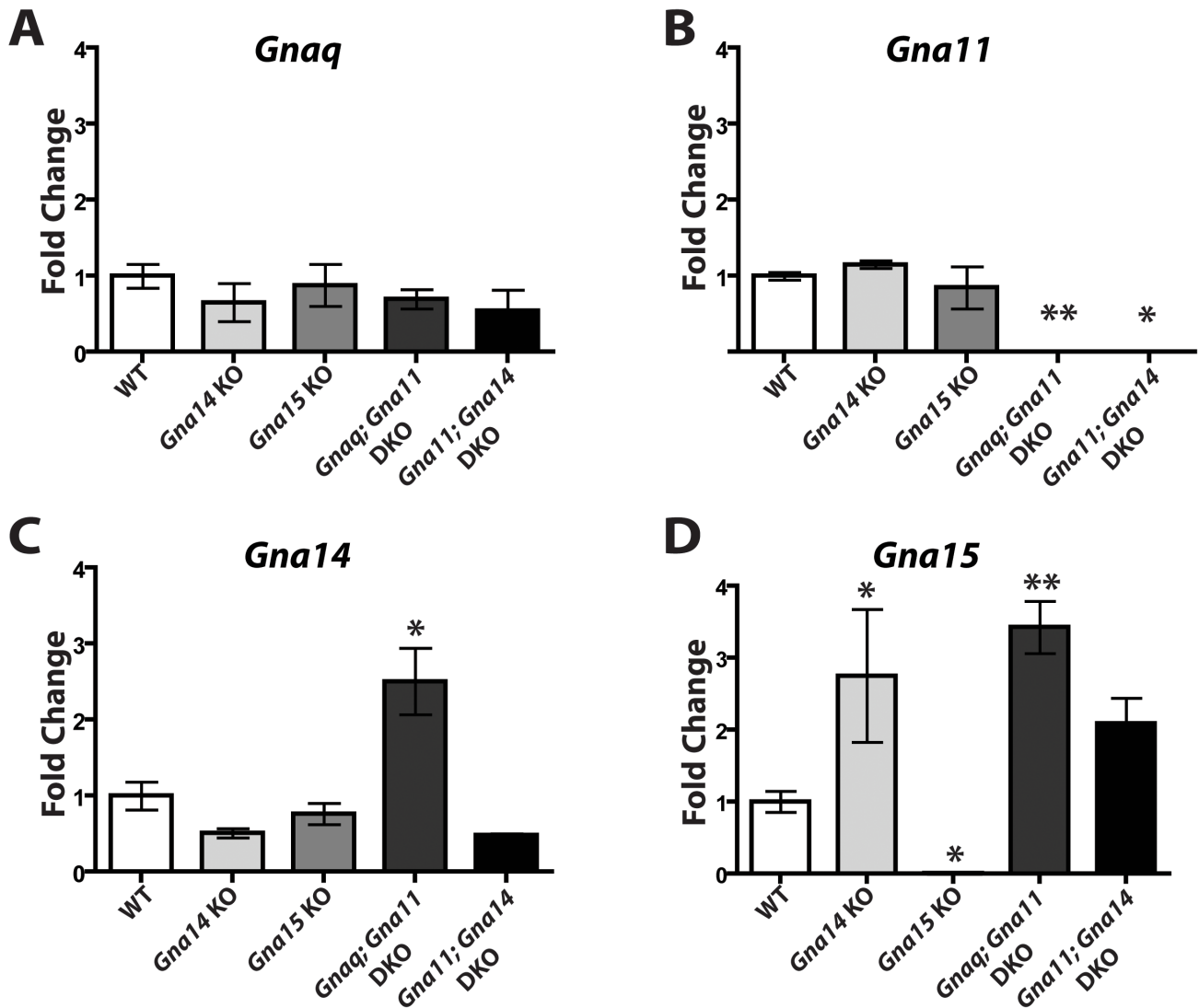
Figure 37. Gq/11 family members are upregulated in the retinas of some Gq/11 mutant lines
A-D. Expression levels of Gnaq, Gna11, Gna14, and Gna15 in the retina relative to WT in Gna14 KO, Gna15 KO, Gnaq; Gna11 DKO, and Gna11; Gna14 DKO mice. Normalized to levels of 18S RNA. (N = 3 mice for each; 2 retinas per RNA sample). * indicates P<0.05 by one-way ANOVA with Tukey post-hoc analysis. Error bars represent s.e.m.

that reached maximum levels several seconds following light onset. After light offset, ipRGCs continued to spike for as long as 20 seconds (Figure 36A, C, D). These slow dynamics are consistent with previous descriptions of melanopsin-dependent light responses (Berson et al., 2002; Dacey et al., 2005; Schmidt et al., 2008; Tu et al., 2005). These data show that despite the fact that *Gna11* and *Gna14* were the only $G_{q/11}$ genes expressed in ipRGCs, they are not required for melanopsin phototransduction.

Other $G_{q/11}$ genes are up-regulated in single and double $G_{q/11}$ knockouts

Since *Gna11* and *Gna14* were the only $G_{q/11}$ genes detected in ipRGCs, we were surprised that *Gna11; Gna14* DKO mice did not recapitulate any of the phenotypes observed in melanopsin knockout animals. To test whether removal of one or two $G_{q/11}$ genes results in upregulation of other $G_{q/11}$ family members, we performed quantitative RT-PCR on RNA extracted from the retinas of mutant mice (Figure 37). We measured the mRNA levels of *Gnaq*, *Gna11*, *Gna14*, and *Gna15* in WT, *Gna14* KO, *Gna15* KO, *Gnaq; Gna11* DKO, and *Gna11; Gna14* DKO mice. We found that all animals had levels of *Gnaq* mRNA that were indistinguishable from WT (Figure 37A). It is important to note that in *Gnaq; Gna11* DKOs, *Gnaq* is conditionally knocked-out in ipRGCs ($Gnaq^{flx/flx}$; $Gna11^{-/-}$; $Opn4^{Cre/+}$); therefore, we did not expect a significant reduction in whole retinal *Gnaq* mRNA in these mutants. *Gna14* KOs and *Gna15* KOs exhibited normal levels of *Gna11* mRNA, while, *Gnaq; Gna11* DKOs, and *Gna11; Gna14* DKOs had undetectable levels (Figure 37B). Levels of *Gna14* mRNA were reduced in *Gna14* KOs and *Gna11; Gna14* DKOs, but increased in *Gnaq; Gna11* DKOs (Figure 37C). *Gna14* mRNA levels are not abolished in *Gna14* KOs and *Gna11; Gna14* DKOs because in the *Gna14* KO line was created by knocking a neo cassette into exon 3 of the gene. This

removes part of exon 3 and results in a frameshift. Thus, while, mRNA is still produced from the *Gna14* locus in *Gna14* KOs, it encodes a nonsense protein. Additionally, as indicated by the reduced mRNA levels, the mutant transcript is degraded. *Gna15* mRNA was undetectable in *Gna15* KOs, but increased in *Gna14* KOs, *Gnaq; Gna11* DKOs, and *Gna11; Gna14* DKOs (Figure 37D). These data indicate there is upregulation of other $G_{q/11}$ genes in some $G_{q/11}$ knockout lines; however, it remains unknown whether the upregulation occurs in ipRGCs and if such upregulation would be sufficient to drive melanopsin phototransduction.

DISCUSSION

In this study, we provide the first investigation of the melanopsin phototransduction pathway *in vivo*. We determined that genetic inactivation of the $G_{q/11}$ proteins that are normally expressed in ipRGCs does not abolish melanopsin–dependent behaviors or electrophysiological responses. Specifically, we found that no tested $G_{q/11}$ knockout line exhibited the behavioral deficits observed in melanopsin knockout mice. All tested $G_{q/11}$ mutant lines exhibited circadian behaviors and pupillary light reflexes that were indistinguishable from WT mice. Additionally, using single-cell RT-PCR for $G_{q/11}$ genes in ipRGCs, we found only expression of *Gna11* and *Gna14*, often expressed together. However, using multielectrode array we detected no changes in intrinsic light responses of ipRGCs in *Gna11; Gna14* DKO compared to WT controls.

Previous reports have shown expression of $G_{q/11}$ genes in ipRGCs although there were inconsistencies as to which $G_{q/11}$ genes were detected (Graham et al., 2008; Siegert et al., 2012). Specifically, in Graham et al. the authors used single cell RT-PCR and determined that expression of all four $G_{q/11}$ genes can be detected in ipRGCs, although expression was heterogeneous among the cells sampled and *Gna14* was detected in the majority of cells(Graham

et al., 2008). Siegert et al. examined ipRGCs as a population and reported expression of *Gna11* and *Gna14* (Siegert et al., 2012), which is consistent with our findings here. However, neither of these studies investigated the function of ipRGCs in the absence of any of these specific genes and in fact Siegert et al. observed the expression of other heterotrimeric G proteins (Siegert et al., 2012).

Electrophysiological investigations of ipRGC phototransduction have supported the involvement of the $G_{q/11}$ pathway. Specifically, Xue et al. showed that melanopsin phototransduction is substantially reduced in the absence of *Plc-β4* (Xue et al.). In agreement with work from Perez-Leighton et al., Xue and co workers additionally showed that loss of both *Trpc6* and *7* virtually abolished the melanopsin-dependent photoresponse suggesting that *Trpc6* and *7* function in a combinatorial fashion (Perez-Leighton et al., 2011; Xue et al.). Since $G_{q/11}$ family members are defined based on their ability to activate PLC, it is reasonable to predict that if *Plc-β* is a critical component of melanopsin phototransduction then there must also be a member of $G_{q/11}$ family involved. This prediction was supported with the use of pharmacological inhibitors of the $G_{q/11}$ family on dissociated ipRGCs (Graham et al., 2008). However, here, we show that *in vivo* mice mutant for $G_{q/11}$ family members do not exhibit the behavioral deficits indicative of a loss of melanopsin-dependent light responses.

Several possibilities exist to explain these discrepancies. One is that $G_{q/11}$ signaling is not required for melanopsin phototransduction. Siegert et al. observed expression of other heterotrimeric G proteins(Siegert et al., 2012) and thus melanopsin could activate a G_i or G_o protein, as has been observed *in vitro* (Bailes and Lucas, 2013), the dissociation of which could result in the beta/gamma subunit activating PLC-β4 as has been observed with PLC-β1 and 3 (Park et al., 1993). Another possibility is that there is compensatory upregulation from other

remaining $G_{q/11}$ family members in the tested mutant lines. Our data supports this possibility since *Gna14* and *Gna15* were upregulated in *Gnaq; Gna11* DKOs. Also, *Gna15* was upregulated in *Gna14* knockouts; although, the increase in *Gna15* expression was not significant in *Gna11; Gna14* DKOs. However, our qRT-PCR experiments were performed on whole retinal RNA, and expression of *Gna15* has not consistently been reported in ipRGCs. Thus, it is unknown whether there is ectopic expression of *Gna15* in ipRGCs in $G_{q/11}$ knockout lines. Whether other $G_{q/11}$ family members are upregulated in the conventional G_q knockout lines could be investigated by creating a mouse line that has all four $G_{q/11}$ genes knocked-out in ipRGCs. Due the fact that $G_{q/11}$ genes exist as two closely linked pairs on two single chromosomes, this quadruple knockout will require creation of a new mutant line in which the linked genes are knockout together. This mouse line would definitively reveal the contribution of the $G_{q/11}$ class alpha subunits to the melanopsin phototransduction cascade.

Additionally, it remains possible that *Gna11* and *Gna14* are required for the activation PLC-β4 and TRPC6/7, but this pathway is not required for normal ipRGC-mediated behavior. In support of this idea, a small residual light-activated current exist in *Plc-β4$^{-/-}$* and *Trpc6/7$^{-/-}$* ipRGCs (Xue et al., 2011). Importantly, voltage recordings were not performed in these mutants. Therefore, it remains possible that this small residual current is sufficient to drive spiking in ipRGCs, which then drives normal non-image-forming visual behaviors. To test this, behavioral assays need to be performed on *Plc-β4$^{-/-}$* and *Trpc6/7$^{-/-}$* mice.

It is important to note that ipRGCs are not a homogeneous population and ipRGC subtypes (termed M1–M5) have stereotyped yet distinct electrophysiological light responses. Thus, it is possible there is variability in the components of the melanopsin phototransduction cascade among ipRGC subtypes. The study showing that ipRGCs have a severe reduction in

their intrinsic light responses in mouse lines mutant for *Trpc6* and *-7* channel genes and *Plc-β4* (Xue et al.) only examined the M1 ipRGC subtype, and in *Trpc6* mutant mice, both M1 and M2 ipRGCs show some deficits in melanopsin-dependent light responses (Perez-Leighton et al., 2011). While M1 ipRGCs are the predominant subtype mediating circadian behaviors, non-M1 ipRGCs may contribute to the PLR (Ecker et al., 2010). It remains unknown whether the intrinsic responses of other ipRGC subtypes are affected in *Trpc6* and *Trpc7* double knockouts or in *Plc-β4* knockouts. Because we picked single cells for RT-PCR at a developmental time, we could not be certain whether we were picking M1 or non-M1 ipRGCs. A careful analysis of the phototransduction in M1 versus non-M1 ipRGCs has interesting functional and evolutionary implications.

ACKNOWLEDGEMENTS

METHODS

Ethics Statement

All protocols, animal housing, and treatment conditions were approved by the Johns Hopkins University Animal Care and Use Committee (IACUC).

Animal Models

All mice were of a mixed background (C57BL/6;129SvJ). Melvin Simon at University of California San Diego generously provided $Gnaq^{flx/flx}$; $Gna11^{-/-}$ animals and $Gna14^{-/-}$ animals (Offermanns, 1999, 2003; Wettschureck et al., 2001), and Thomas Wilkie at University of Texas Southwestern generously provided $Gna15^{-/-}$ animals (Davignon et al., 2000). $Gnaq^{flx/flx}$; $Gna11^{-/-}$ animals were crossed into our $Opn4^{Cre/+}$ line to produce $Opn4^{Cre/+}$; $Gnaq^{flx/flx}$; $Gna11^{-/-}$ mice. $Gnaq^{flx/flx}$; $Gna11^{-/-}$ mice were also crossed with $Gna14^{-/-}$ mice to produce $Gna11^{-/-}$; $Gna14^{-/-}$ animals.

Single Cell RT-PCR

Single ipRGCs were isolated from $Opn4^{Cre/+}$; Z/EG mice following the protocol described in (Goetz and Trimarchi, 2012). Reverse transcription of the RNA from single cells from P1 and P4 retinas, and amplification of the cDNA was performed as described in (Goetz and Trimarchi, 2012). The following primers were designed to amplify from the 3' end of the transcript and used to detect phototransduction components in the resulting amplified cDNA obtained from single ipRGCs: Melanopsin (F: CTTTGCTGGATACTCGCACA; R: CAGGCACCTTGGGAGTCTTA), $Gnaq$ (F: GTTCGAGTCCCCACTACAGG; R: GGTTCAGGTCCACGAACATT), $Gna11$ (F: GTACCCGTTTGACCTGGAGA; R: AGGATGGTGTCCTTCACAGC), $Gna14$ (F: CCATTCGACCTGGAAAACAT; R:

CAGCAAACACAAAGCGGATA), *Gna15* (F: TGAGCGAGTATGACCAGTGC, R: CAGGTTGATCTCGTCCAGGT).

Pupillometry

Pupil experiments were performed on unanesthetized mice that were restrained by hand. WT (16 animals), MKO (7 animals), *Gna11* KO (4 animals), *Gna14* KO (5 animals), *Gna15* KO (7 animals), *Gnaq; Gna11* DKO (9 animals), and *Gna11; Gna14* DKO (7 animals) were kept on a 12 hour:12 hour light:dark cycle and given at least 30 minutes to dark-adapt between stimulations. All experiments were performed during the animals' day (ZT2-10). The contralateral eye was stimulated with 474-nm LED light for 30-60s. Neutral density filters were interposed in the light path to modulate light intensity and light intensity was measured using a photometer (Solar Light). High light indicates 1.4×10^{16} photons/cm^2/sec, and low light indicates 7.3×10^{13} photons/cm^2/sec.

Wheel Running Behavior

Mice were placed in cages with a 4.5-inch running wheel, and their activity was monitored with VitalView software (Mini Mitter), and cages were changed at least every 2 weeks.

WT (14 animals), MKO (9 animals), *Gna15* KO (7 animals), *Gnaq; Gna11* DKO (8 animals), and *Gna11; Gna14* DKO (7 animals) mice were placed in 12:12 LD for 17 days followed by constant darkness for 26 days. For phase-shifting experiments, each animal was exposed to a light pulse (500 lux; CT15) for 15 min, after being in constant dark for 18 days. Following constant darkness, all mice were also placed in constant light (500 lux) for 18 days.

Quantification of circadian behavior

All free-running periods were calculated with ClockLab (Actimetrics) using the onsets of activity on days 10-17 of constant darkness similar to (Güler et al., 2008). Phase shifts were calculated similar to (Güler et al., 2008) and described as follows: an onset for the day after the light pulse was predicted based on the onsets of the previous 7 days. Phase shifts were then determined based on the difference between the predicted onset and the shifted onset on the day after the light pulse. For all animals, the free-running period in constant light was measured with ClockLab (Actimetrics) using the onsets of activity on days 3-10 of constant light. Some animals (2 WT, 1 *Gna15* KO, 2 *Gnaq; Gna11* DKOs, 1 *Gna11; Gna14* DKO, and 1 MKO) reduced their activity so much that an accurate period could not be measured and they were thus excluded.

Multielectrode Array Recordings

Multielectrode array recordings, light stimulation, and data analysis were performed as described in (Perez-Leighton et al., 2011). Briefly, retinas were dissected from P3 pups from WT and *Gna11*; *Gna14* DKO animals and mounted ganglion cell side down on the array. Retinas were superfused with Ames' Medium (Sigma) and synaptic blocker cocktail oxygenated with 95%/5% Oxygen/CO2. Synaptic blocker cocktail consisted of: 250 µM DL-2-amino-4-phosphonobutyrate ; 10 µM 6,7-dinitroquinoxaline (DNQX, α-amino-3-hydroxy-5-methyl-4-isoxazolepropionic acid); 0.3 µM strychnine, 50 µM picrotoxin, and 10 nM (±)-epibatidine dihydrochloride. All reagents were purchased from Tocris (Ellesville, MO, USA). Spike sorting was performed using MCRack v 4.0.0 software (Multi Channel Systems)and analyzed offline with Offline Sorter v 2.8.6 software (Plexon Inc, Dallas, TX, USA).

Q-RT-PCR

Retinas were dissected from WT, *Gna14* KO, *Gna15* KO, *Gnaq; Gna11* DKO, and *Gna11; Gna14* DKO (N = 3 mice for each; 2 retinas per RNA sample). RNA was extracted from the retinas using an RNeasy mini kit (Qiagen; cat# 74106), and reverse transcription was performed using a RETROscript kit (Life Technology; cat # AM1710) and random hexamer primers. Quantitative PCR on the resulting cDNA was performed with SYBR Green PCR Master Mix (Fermentas, cat# K0221), samples were analyzed in duplicate, and the levels were normalized to 18S RNA. The following primers were used: *Gnaq* (F: AATCATGTATTCCCACCTAGTCG; R: GGTTCAGGTCCACGAACATT), *Gna11* (F: TCCTGCACTCACACTTGGTC; R: GGGTTCAGGTCCACAAACAT), *Gna14* (F: TCACCTACCCCTGGTTTCTG; R: CCGCTTTGACATCTTGCTTT), *Gna15* (F: ACCTCGGTCATCCTCTTCCT, R: CGCATACATGTCCAAGATGAA), and 18S RNA (F: CGCCGCTAGAGGTGAAATTC; R: TTGGCAAATGCTTTCGCTC).

CHAPTER 5: FINAL REMARKS

In this body of work, previously unappreciated mechanisms underlying developmental neural circuit formation were identified. ipRGCs form ordered arrays by proximity-dependent Bax-mediated apoptosis, and such order is necessary for ipRGCs to integrate into retinal circuitry and receive light information from rods and cones. However, several questions remain. How do nearby ipRGCs recognize each other to initiate the apoptosis cascade? What are the molecular signals that confine ipRGC dendrites to a specific layer in the retina? And why does disruption of the retinal mosaic of ipRGCs cause disruptions in those signals? Does Bax have a role in ipRGCs beyond apoptosis such as in synaptic function? and Must other retinal neurons form an ordered array in order to be incorporated into the retinal network?

Here it was also revealed that ipRGCs have a critical developmental role in circadian regulation and the functional formation of retinotopic circuitry. Several questions remain following this body of work too. How does light information via ipRGCs set the period of the circadian? Specifically, what molecular changes in the circadian clock occur when the period is set? How does a single light pulse induce a permanent change in the circadian clock? What is the extent of ipRGC modulation of retinal wave dynamics? and How do ipRGCs accomplish modulation of retinal wave dynamics, and if this occurs through intraretinal axonal collateral axons, what are the synaptic partners of these processes?

In the final portion of this thesis, the phototransduction cascade utilized by ipRGCs *in vivo* was investigated. This work may have succeeded in raising more questions than it addressed. Are $G_{q/11}$ proteins necessary for melanopsin-based phototransduction *in vivo*? If a $G_{q/11}$ protein is not required, what G-protein does melanopsin utilize? Are Plc-b4 or Trpc6 and 7 required for melanopsin phototransduction *in vivo*? Do different subtypes of ipRGCs utilize different

phototransduction cascades, and if so how do such difference relate to the previously observed

subtype-specific differences in melanopsin-dependent light responses?

REFERENCES:

Ackman, J.B., Burbridge, T.J., and Crair, M.C. (2012). Retinal waves coordinate patterned activity throughout the developing visual system. Nature *490*, 219-225.

Allen, A.E., Cameron, M.A., Brown, T.M., Vugler, A.A., and Lucas, R.J. (2010). Visual responses in mice lacking critical components of all known retinal phototransduction cascades. PLoS ONE *5*, e15063.

Autret, A., and Martin, S.J. (2009). Emerging role for members of the Bcl-2 family in mitochondrial morphogenesis. Mol Cell *36*, 355-363.

Bailes, H.J., and Lucas, R.J. (2013). Human melanopsin forms a pigment maximally sensitive to blue light (lambdamax approximately 479 nm) supporting activation of G(q/11) and G(i/o) signalling cascades. Proceedings Biological sciences / The Royal Society *280*, 20122987.

Baver, S.B., Pickard, G.E., Sollars, P.J., and Pickard, G.E. (2008). Two types of melanopsin retinal ganglion cell differentially innervate the hypothalamic suprachiasmatic nucleus and the olivary pretectal nucleus. Eur J Neurosci *27*, 1763-1770.

Berson, D.M. (2003). Strange vision: ganglion cells as circadian photoreceptors. Trends Neurosci *26*, 314-320.

Berson, D.M. (2007). Phototransduction in ganglion-cell photoreceptors. Pflugers Arch *454*, 849-855.

Berson, D.M., Castrucci, A.M., and Provencio, I. (2010). Morphology and mosaics of melanopsin-expressing retinal ganglion cell types in mice. J Comp Neurol *518*, 2405-2422.

Berson, D.M., Dunn, F.A., and Takao, M. (2002). Phototransduction by retinal ganglion cells that set the circadian clock. Science *295*, 1070-1073.

Brown, T.M., Gias, C., Hatori, M., Keding, S.R., Semo, M., Coffey, P.J., Gigg, J., Piggins, H.D., Panda, S., and Lucas, R.J. (2010). Melanopsin contributions to irradiance coding in the thalamo-cortical visual system. PLoS Biol *8*, e1000558.

Bunting, M., Bernstein, K.E., Greer, J.M., Capecchi, M.R., and Thomas, K.R. (1999). Targeting genes for self-excision in the germ line. Genes Dev *13*, 1524-1528.

Burns, C.J., Zhang, J., Brown, E.C., Van Bibber, A.M., Van Es, J., Clevers, H., Ishikawa, T.O., Taketo, M.M., Vetter, M.L., and Fuhrmann, S. (2008). Investigation of Frizzled-5 during embryonic neural development in mouse. Dev Dyn *237*, 1614-1626.

Cellerino, A., Galli-Resta, L., and Colombaioni, L. (2000). The dynamics of neuronal death: a time-lapse study in the retina. J Neurosci *20*, RC92.

Chandrasekaran, A.R., Plas, D.T., Gonzalez, E., and Crair, M.C. (2005). Evidence for an instructive role of retinal activity in retinotopic map refinement in the superior colliculus of the mouse. J Neurosci *25*, 6929-6938.

Chen, S.K., Badea, T.C., and Hattar, S. (2011). Photoentrainment and pupillary light reflex are mediated by distinct populations of ipRGCs. Nature *476*, 92-95.

Cheng, H.J., Nakamoto, M., Bergemann, A.D., and Flanagan, J.G. (1995). Complementary gradients in expression and binding of ELF-1 and Mek4 in development of the topographic retinotectal projection map. Cell *82*, 371-381.

Contini, M., and Raviola, E. (2003). GABAergic synapses made by a retinal dopaminergic neuron. Proc Natl Acad Sci U S A *100*, 1358-1363.

Cook, J.E., and Chalupa, L.M. (2000). Retinal mosaics: new insights into an old concept. Trends Neurosci *23*, 26-34.

Cook, J.E., and Noden, A.J. (1998). Somatic and dendritic mosaics formed by large ganglion cells in the retina of the common house gecko (Hemidactylus frenatus). Brain Behav Evol *51*, 263-283.

Coombs, J., van der List, D., Wang, G.Y., and Chalupa, L.M. (2006). Morphological properties of mouse retinal ganglion cells. Neuroscience *140*, 123-136.

Czeisler, C.A., Shanahan, T.L., Klerman, E.B., Martens, H., Brotman, D.J., Emens, J.S., Klein, T., and Rizzo, J.F., 3rd (1995). Suppression of melatonin secretion in some blind patients by exposure to bright light. N Engl J Med *332*, 6-11.

Dacey, D.M., Liao, H.-W., Peterson, B.B., Robinson, F.R., Smith, V.C., Pokorny, J., Yau, K.-W., and Gamlin, P.D. (2005). Melanopsin-expressing ganglion cells in primate retina signal colour and irradiance and project to the LGN. Nature *433*, 749-754.

Davignon, I., Barnard, M., Gavrilova, O., Sweet, K., and Wilkie, T.M. (1996). Gene structure of murine Gna11 and Gna15: tandemly duplicated Gq class G protein alpha subunit genes. Genomics *31*, 359-366.

Davignon, I., Catalina, M.D., Smith, D., Montgomery, J., Swantek, J., Croy, J., Siegelman, M., and Wilkie, T.M. (2000). Normal hematopoiesis and inflammatory responses despite discrete signaling defects in Galpha15 knockout mice. Mol Cell Biol *20*, 797-804.

Davis, F., and Menaker, M. (1981). Development of the mouse circadian pacemaker: independence from environmental cycles. Journal of Comparative Physiology.

Davis, F.C., and Gorski, R.A. (1985). Development of hamster circadian rhythms: prenatal entrainment of the pacemaker. Journal of Biological Rhythms *1*, 77-89.

Demas, J., Sagdullaev, B.T., Green, E., Jaubert-Miazza, L., McCall, M.A., Gregg, R.G., Wong, R.O., and Guido, W. (2006). Failure to maintain eye-specific segregation in nob, a mutant with abnormally patterned retinal activity. Neuron *50*, 247-259.

Dennis, E.A., and Bradshaw, R.A. (2011). Intercellular signaling in development and disease (Amsterdam ; Boston: Academic Press).

Do, M.T., Kang, S.H., Xue, T., Zhong, H., Liao, H.W., Bergles, D.E., and Yau, K.W. (2009). Photon capture and signalling by melanopsin retinal ganglion cells. Nature *457*, 281-287.

Douglas, R.M., Alam, N.M., Silver, B.D., McGill, T.J., Tschetter, W.W., and Prusky, G.T. (2005). Independent visual threshold measurements in the two eyes of freely moving rats and mice using a virtual-reality optokinetic system. Vis Neurosci *22*, 677-684.

Dreher, B., Potts, R.A., and Bennett, M.R. (1983). Evidence that the early postnatal reduction in the number of rat retinal ganglion cells is due to a wave of ganglion cell death. Neurosci Lett *36*, 255-260.

Dreher, B., and Robinson, S.R. (1991). Neuroanatomy of the visual pathways and their development (Boca Raton: CRC Press).

Drescher, U., Kremoser, C., Handwerker, C., Loschinger, J., Noda, M., and Bonhoeffer, F. (1995). In vitro guidance of retinal ganglion cell axons by RAGS, a 25 kDa tectal protein related to ligands for Eph receptor tyrosine kinases. Cell *82*, 359-370.

Dumitrescu, O.N., Pucci, F.G., Wong, K.Y., and Berson, D.M. (2009). Ectopic retinal ON bipolar cell synapses in the OFF inner plexiform layer: contacts with dopaminergic amacrine cells and melanopsin ganglion cells. J Comp Neurol *517*, 226-244.

Ecker, J.L., Dumitrescu, O.N., Wong, K.Y., Alam, N.M., Chen, S.-K., LeGates, T., Renna, J.M., Prusky, G.T., Berson, D.M., and Hattar, S. (2010). Melanopsin-expressing retinal ganglion-cell photoreceptors: cellular diversity and role in pattern vision. Neuron *67*, 49-60.

Estevez, M.E., Fogerson, P.M., Ilardi, M.C., Borghuis, B.G., Chan, E., Weng, S., Auferkorte, O.N., Demb, J.B., and Berson, D.M. (2012). Form and function of the M4 cell, an intrinsically photosensitive retinal ganglion cell type contributing to geniculocortical vision. J Neurosci *32*, 13608-13620.

Farah, M.H., and Easter, S.S., Jr. (2005). Cell birth and death in the mouse retinal ganglion cell layer. J Comp Neurol *489*, 120-134.

Feller, M.B. (2002). The role of nAChR-mediated spontaneous retinal activity in visual system development. J Neurobiol *53*, 556-567.

Feller, M.B. (2009). Retinal waves are likely to instruct the formation of eye-specific retinogeniculate projections. Neural development *4*, 24.

Fernandez, D.C., Pasquini, L.A., Dorfman, D., Aldana Marcos, H.J., and Rosenstein, R.E. (2012). Ischemic conditioning protects from axoglial alterations of the optic pathway induced by experimental diabetes in rats. PLoS ONE *7*, e51966.

Firth, S.I., Wang, C.T., and Feller, M.B. (2005). Retinal waves: mechanisms and function in visual system development. Cell Calcium *37*, 425-432.

Fischer, K.F., Lukasiewicz, P.D., and Wong, R.O. (1998). Age-dependent and cell class-specific modulation of retinal ganglion cell bursting activity by GABA. J Neurosci *18*, 3767-3778.

Foster, R.G., and Hankins, M.W. (2002). Non-rod, non-cone photoreception in the vertebrates. Prog Retin Eye Res *21*, 507-527.

Foster, R.G., Provencio, I., Hudson, D., Fiske, S., De Grip, W., and Menaker, M. (1991). Circadian photoreception in the retinally degenerate mouse (rd/rd). J Comp Physiol A *169*, 39-50.

Freedman, M.S., Lucas, R.J., Soni, B., von Schantz, M., Munoz, M., David-Gray, Z., and Foster, R. (1999). Regulation of mammalian circadian behavior by non-rod, non-cone, ocular photoreceptors. Science *284*, 502-504.

Fuerst, P.G., Bruce, F., Tian, M., Wei, W., Elstrott, J., Feller, M.B., Erskine, L., Singer, J.H., and Burgess, R.W. (2009). DSCAM and DSCAML1 function in self-avoidance in multiple cell types in the developing mouse retina. Neuron *64*, 484-497.

Fuerst, P.G., Koizumi, A., Masland, R.H., and Burgess, R.W. (2008). Neurite arborization and mosaic spacing in the mouse retina require DSCAM. Nature *451*, 470-474.

Galli-Resta, L. (2002). Putting neurons in the right places: local interactions in the genesis of retinal architecture. Trends Neurosci *25*, 638-643.

Goetz, J.J., and Trimarchi, J.M. (2012). Single-cell profiling of developing and mature retinal neurons. J Vis Exp.

Graham, D.M., Wong, K.Y., Shapiro, P., Frederick, C., Pattabiraman, K., and Berson, D.M. (2008). Melanopsin ganglion cells use a membrane-associated rhabdomeric phototransduction cascade. Journal of Neurophysiology *99*, 2522-2532.

Gray, P.A., Fu, H., Luo, P., Zhao, Q., Yu, J., Ferrari, A., Tenzen, T., Yuk, D.I., Tsung, E.F., Cai, Z.*, et al.* (2004). Mouse brain organization revealed through direct genome-scale TF expression analysis. Science *306*, 2255-2257.

Güler, A.D., Ecker, J.L., Lall, G.S., Haq, S., Altimus, C.M., Liao, H.-W., Barnard, A.R., Cahill, H., Badea, T.C., Zhao, H.*, et al.* (2008). Melanopsin cells are the principal conduits for rod-cone input to non-image-forming vision. Nature *453*, 102-105.

Hankins, M.W., and Lucas, R.J. (2002). The primary visual pathway in humans is regulated according to long-term light exposure through the action of a nonclassical photopigment. Curr Biol *12*, 191-198.

Hardie, R.C. (2001). Phototransduction in Drosophila melanogaster. J Exp Biol *204*, 3403-3409.

Harmer, S.L., Panda, S., and Kay, S.A. (2001). Molecular bases of circadian rhythms. Annu Rev Cell Dev Biol *17*, 215-253.

Hattar, S., Kumar, M., Park, A., Tong, P., Tung, J., Yau, K.-W., and Berson, D.M. (2006). Central projections of melanopsin-expressing retinal ganglion cells in the mouse. J Comp Neurol *497*, 326-349.

Hattar, S., Liao, H.W., Takao, M., Berson, D.M., and Yau, K.W. (2002). Melanopsin-containing retinal ganglion cells: architecture, projections, and intrinsic photosensitivity. Science *295*, 1065-1070.

Hattar, S., Lucas, R.J., Mrosovsky, N., Thompson, S., Douglas, R.H., Hankins, M.W., Lem, J., Biel, M., Hofmann, F., Foster, R.G.*, et al.* (2003). Melanopsin and rod-cone photoreceptive systems account for all major accessory visual functions in mice. Nature *424*, 76-81.

Hirasawa, H., Puopolo, M., and Raviola, E. (2009). Extrasynaptic release of GABA by retinal dopaminergic neurons. J Neurophysiol *102*, 146-158.

Hoshi, H., Liu, W.L., Massey, S.C., and Mills, S.L. (2009). ON inputs to the OFF layer: bipolar cells that break the stratification rules of the retina. J Neurosci *29*, 8875-8883.

Huang, J., Liu, C.H., Hughes, S.A., Postma, M., Schwiening, C.J., and Hardie, R.C. (2010). Activation of TRP channels by protons and phosphoinositide depletion in Drosophila photoreceptors. Curr Biol *20*, 189-197.

Jain, V., Ravindran, E., and Dhingra, N.K. (2012). Differential expression of Brn3 transcription factors in intrinsically photosensitive retinal ganglion cells in mouse. J Comp Neurol *520*, 742-755.

Jiao, S., and Li, Z. (2011). Nonapoptotic function of BAD and BAX in long-term depression of synaptic transmission. Neuron *70*, 758-772.

Jonas, E.A., Hardwick, J.M., and Kaczmarek, L.K. (2005). Actions of BAX on mitochondrial channel activity and on synaptic transmission. Antioxid Redox Signal *7*, 1092-1100.

Joo, H.R., Peterson, B.B., Dacey, D.M., Hattar, S., and Chen, S.K. (2013). Recurrent axon collaterals of intrinsically photosensitive retinal ganglion cells. Vis Neurosci *30*, 175-182.

Jud, C., and Albrecht, U. (2006). Circadian rhythms in murine pups develop in absence of a functional maternal circadian clock. J Biol Rhythms *21*, 149-154.

Kampf-Lassin, A., Wei, J., Galang, J., and Prendergast, B.J. (2011). Experience-independent development of the hamster circadian visual system. PLoS ONE *6*, e16048.

Keeley, P.W., and Reese, B.E. (2010). Role of afferents in the differentiation of bipolar cells in the mouse retina. J Neurosci *30*, 1677-1685.

Keeley, P.W., Sliff, B.J., Lee, S.C., Fuerst, P.G., Burgess, R.W., Eglen, S.J., and Reese, B.E. (2012). Neuronal clustering and fasciculation phenotype in Dscam- and Bax-deficient mouse retinas. J Comp Neurol *520*, 1349-1364.

Kirkby, L.A., A., A.D., and Feller, M.B. (2012). Influence of cholinergic retinal waves on the development of ipRGC light-response properties. Program No 32603 Neuroscience Meeting Planner New Orleans, LA: Society for Neuroscience *Online*.

Klerman, E.B., Shanahan, T.L., Brotman, D.J., Rimmer, D.W., Emens, J.S., Rizzo, J.F., 3rd, and Czeisler, C.A. (2002). Photic resetting of the human circadian pacemaker in the absence of conscious vision. J Biol Rhythms *17*, 548-555.

Laemle, L.K., and Ottenweller, J.E. (1998). Daily patterns of running wheel activity in male anophthalmic mice. Physiol Behav *64*, 165-171.

Lin, B., Wang, S.W., and Masland, R.H. (2004). Retinal ganglion cell type, size, and spacing can be specified independent of homotypic dendritic contacts. Neuron *43*, 475-485.

Lobe, C.G., Koop, K.E., Kreppner, W., Lomeli, H., Gertsenstein, M., and Nagy, A. (1999). Z/AP, a double reporter for cre-mediated recombination. Dev Biol *208*, 281-292.

Lucas, R.J., Douglas, R.H., and Foster, R.G. (2001). Characterization of an ocular photopigment capable of driving pupillary constriction in mice. Nat Neurosci *4*, 621-626.

Lucas, R.J., Freedman, M.S., Munoz, M., Garcia-Fernandez, J.M., and Foster, R.G. (1999). Regulation of the mammalian pineal by non-rod, non-cone, ocular photoreceptors. Science *284*, 505-507.

Lucas, R.J., Hattar, S., Takao, M., Berson, D.M., Foster, R.G., and Yau, K.W. (2003). Diminished pupillary light reflex at high irradiances in melanopsin-knockout mice. Science *299*, 245-247.

Matsuoka, R.L., Jiang, Z., Samuels, I.S., Nguyen-Ba-Charvet, K.T., Sun, L.O., Peachey, N.S., Chedotal, A., Yau, K.W., and Kolodkin, A.L. (2012). Guidance-cue control of horizontal cell

morphology, lamination, and synapse formation in the mammalian outer retina. J Neurosci *32*, 6859-6868.

McLaughlin, T., Torborg, C.L., Feller, M.B., and O'Leary, D.D. (2003a). Retinotopic map refinement requires spontaneous retinal waves during a brief critical period of development. Neuron *40*, 1147-1160.

McLaughlin, T., Torborg, C.L., Feller, M.B., and O'Leary, D.D.M. (2003b). Retinotopic map refinement requires spontaneous retinal waves during a brief critical period of development. Neuron *40*, 1147-1160.

McNeill, D.S., Sheely, C.J., Ecker, J.L., Badea, T.C., Morhardt, D., Guido, W., and Hattar, S. (2011). Development of melanopsin-based irradiance detecting circuitry. Neural development *6*, 8.

Meister, M., Wong, R.O., Baylor, D.A., and Shatz, C.J. (1991). Synchronous bursts of action potentials in ganglion cells of the developing mammalian retina. Science *252*, 939-943.

Menaker, M., Takahashi, J.S., and Eskin, A. (1978). The physiology of circadian pacemakers. Annu Rev Physiol *40*, 501-526.

Miyagishima, K.J., Cornwall, M.C., and Sampath, A.P. (2009). Metabolic constraints on the recovery of sensitivity after visual pigment bleaching in retinal rods. J Gen Physiol *134*, 165-175.

Moore, R.Y. (1997). Circadian rhythms: basic neurobiology and clinical applications. Annu Rev Med *48*, 253-266.

Mosinger Ogilvie, J., Deckwerth, T.L., Knudson, C.M., and Korsmeyer, S.J. (1998). Suppression of developmental retinal cell death but not of photoreceptor degeneration in Bax-deficient mice. Invest Ophthalmol Vis Sci *39*, 1713-1720.

Mrosovsky, N., and Hattar, S. (2003). Impaired masking responses to light in melanopsin-knockout mice. Chronobiol Int *20*, 989-999.

Mrsic-Flogel, T.D., Hofer, S.B., Creutzfeldt, C., Cloez-Tayarani, I., Changeux, J.P., Bonhoeffer, T., and Hubener, M. (2005). Altered map of visual space in the superior colliculus of mice lacking early retinal waves. J Neurosci *25*, 6921-6928.

Mu, X., Fu, X., Sun, H., Liang, S., Maeda, H., Frishman, L.J., and Klein, W.H. (2005). Ganglion cells are required for normal progenitor- cell proliferation but not cell-fate determination or patterning in the developing mouse retina. Curr Biol *15*, 525-530.

Muir-Robinson, G., Hwang, B.J., and Feller, M.B. (2002). Retinogeniculate axons undergo eye-specific segregation in the absence of eye-specific layers. J Neurosci *22*, 5259-5264.

Novak, A., Guo, C., Yang, W., Nagy, A., and Lobe, C.G. (2000). Z/EG, a double reporter mouse line that expresses enhanced green fluorescent protein upon Cre-mediated excision. Genesis *28*, 147-155.

Offermanns, S. (1999). New insights into the in vivo function of heterotrimeric G-proteins through gene deletion studies. Naunyn Schmiedebergs Arch Pharmacol *360*, 5-13.

Offermanns, S. (2003). G-proteins as transducers in transmembrane signalling. Prog Biophys Mol Biol *83*, 101-130.

Offermanns, S., Zhao, L.P., Gohla, A., Sarosi, I., Simon, M.I., and Wilkie, T.M. (1998). Embryonic cardiomyocyte hypoplasia and craniofacial defects in G alpha q/G alpha 11-mutant mice. EMBO J *17*, 4304-4312.

Panda, S., Provencio, I., Tu, D.C., Pires, S.S., Rollag, M.D., Castrucci, A.M., Pletcher, M.T., Sato, T.K., Wiltshire, T., Andahazy, M.*, et al.* (2003). Melanopsin is required for non-image-forming photic responses in blind mice. Science *301*, 525-527.

Panda, S., Sato, T.K., Castrucci, A.M., Rollag, M.D., DeGrip, W.J., Hogenesch, J.B., Provencio, I., and Kay, S.A. (2002). Melanopsin (Opn4) requirement for normal light-induced circadian phase shifting. Science *298*, 2213-2216.

Park, D., Jhon, D.Y., Lee, C.W., Lee, K.H., and Rhee, S.G. (1993). Activation of phospholipase C isozymes by G protein beta gamma subunits. J Biol Chem *268*, 4573-4576.

Perez-Leighton, C.E., Schmidt, T.M., Abramowitz, J., Birnbaumer, L., and Kofuji, P. (2011). Intrinsic phototransduction persists in melanopsin-expressing ganglion cells lacking diacylglycerol-sensitive TRPC subunits. Eur J Neurosci *33*, 856-867.

Perry, V.H., Henderson, Z., and Linden, R. (1983). Postnatal changes in retinal ganglion cell and optic axon populations in the pigmented rat. J Comp Neurol *219*, 356-368.

Pfeiffenberger, C., Cutforth, T., Woods, G., Yamada, J., Renteria, R.C., Copenhagen, D.R., Flanagan, J.G., and Feldheim, D.A. (2005). Ephrin-As and neural activity are required for eye-specific patterning during retinogeniculate mapping. Nat Neurosci *8*, 1022-1027.

Pittendrigh, C.S. (1954). On Temperature Independence in the Clock System Controlling Emergence Time in Drosophila. Proc Natl Acad Sci U S A *40*, 1018-1029.

Prichard, J.R., Fahy, J.L., Obermeyer, W.H., Behan, M., and Benca, R.M. (2004). Sleep responses to light and dark are shaped by early experience. Behav Neurosci *118*, 1262-1273.

Provencio, I., Jiang, G., De Grip, W.J., Hayes, W.P., and Rollag, M.D. (1998). Melanopsin: An opsin in melanophores, brain, and eye. Proc Natl Acad Sci USA *95*, 340-345.

Provencio, I., Rodriguez, I.R., Jiang, G., Hayes, W.P., Moreira, E.F., and Rollag, M.D. (2000). A novel human opsin in the inner retina. J Neurosci *20*, 600-605.

Provencio, I., Rollag, M.D., and Castrucci, A.M. (2002). Photoreceptive net in the mammalian retina. This mesh of cells may explain how some blind mice can still tell day from night. Nature *415*, 493.

Prusky, G.T., West, P.W., and Douglas, R.M. (2000). Behavioral assessment of visual acuity in mice and rats. Vision Res *40*, 2201-2209.

Quina, L.A., Pak, W., Lanier, J., Banwait, P., Gratwick, K., Liu, Y., Velasquez, T., O'Leary, D.D.M., Goulding, M., and Turner, E.E. (2005). Brn3a-expressing retinal ganglion cells project specifically to thalamocortical and collicular visual pathways. J Neurosci *25*, 11595-11604.

Raven, M.A., Eglen, S.J., Ohab, J.J., and Reese, B.E. (2003). Determinants of the exclusion zone in dopaminergic amacrine cell mosaics. J Comp Neurol *461*, 123-136.

Reese, B. (2008). Mosaics, tiling and coverage by retinal neurons. The Senses: A Comprehensive Reference   Elsevier, Oxford *Vol. 1: Vision*, 439-456,.

Renna, J.M., Weng, S., and Berson, D.M. (2011). Light acts through melanopsin to alter retinal waves and segregation of retinogeniculate afferents. Nat Neurosci *14*, 827-829.

Richter, C.P. (1971). Inborn nature of the rat's 24-hour clock. J Comp Physiol Psychol *75*, 1-4.

Ruby, N.F., Brennan, T.J., Xie, X., Cao, V., Franken, P., Heller, H.C., and O'Hara, B.F. (2002). Role of melanopsin in circadian responses to light. Science *298*, 2211-2213.

Schmidt, T.M., Chen, S.K., and Hattar, S. (2011). Intrinsically photosensitive retinal ganglion cells: many subtypes, diverse functions. Trends Neurosci *34*, 572-580.

Schmidt, T.M., and Kofuji, P. (2009). Functional and morphological differences among intrinsically photosensitive retinal ganglion cells. J Neurosci *29*, 476-482.

Schmidt, T.M., Taniguchi, K., and Kofuji, P. (2008). Intrinsic and extrinsic light responses in melanopsin-expressing ganglion cells during mouse development. Journal of Neurophysiology *100*, 371-384.

Sekaran, S., Lupi, D., Jones, S.L., Sheely, C.J., Hattar, S., Yau, K.-W., Lucas, R.J., Foster, R.G., and Hankins, M.W. (2005). Melanopsin-dependent photoreception provides earliest light detection in the mammalian retina. Curr Biol *15*, 1099-1107.

Sernagor, E., Eglen, S.J., and Wong, R.O. (2001). Development of retinal ganglion cell structure and function. Prog Retin Eye Res *20*, 139-174.

Sernagor, E., Young, C., and Eglen, S.J. (2003). Developmental modulation of retinal wave dynamics: shedding light on the GABA saga. J Neurosci *23*, 7621-7629.

Shah, R.D., and Crair, M.C. (2008). Retinocollicular synapse maturation and plasticity are regulated by correlated retinal waves. J Neurosci *28*, 292-303.

Shatz, C.J., and Stryker, M.P. (1988). Prenatal tetrodotoxin infusion blocks segregation of retinogeniculate afferents. Science *242*, 87-89.

Shoham, S., Fellows, M.R., and Normann, R.A. (2003). Robust, automatic spike sorting using mixtures of multivariate t-distributions. J Neurosci Methods *127*, 111-122.

Siegert, S., Cabuy, E., Scherf, B.G., Kohler, H., Panda, S., Le, Y.Z., Fehling, H.J., Gaidatzis, D., Stadler, M.B., and Roska, B. (2012). Transcriptional code and disease map for adult retinal cell types. Nat Neurosci *15*, 487-495, S481-482.

Sollars, P.J., Smeraski, C.A., Kaufman, J.D., Ogilvie, M.D., Provencio, I., and Pickard, G.E. (2003). Melanopsin and non-melanopsin expressing retinal ganglion cells innervate the hypothalamic suprachiasmatic nucleus. Vis Neurosci *20*, 601-610.

Speer, C.M., Mikula, S., Huberman, A.D., and Chapman, B. (2010). The developmental remodeling of eye-specific afferents in the ferret dorsal lateral geniculate nucleus. Anat Rec (Hoboken) *293*, 1-24.

Sperry, R.W. (1943). Effect of 180 degree rotation of the retinal field on visuomotor coordination. Journal of Experimental Zoology *92*, 263-279.

Stellwagen, D., and Shatz, C.J. (2002). An instructive role for retinal waves in the development of retinogeniculate connectivity. Neuron *33*, 357-367.

Sun, C., Speer, C.M., Wang, G.Y., Chapman, B., and Chalupa, L.M. (2008). Epibatidine application in vitro blocks retinal waves without silencing all retinal ganglion cell action potentials in developing retina of the mouse and ferret. J Neurophysiol *100*, 3253-3263.

Takeuchi, O., Fisher, J., Suh, H., Harada, H., Malynn, B.A., and Korsmeyer, S.J. (2005). Essential role of BAX,BAK in B cell homeostasis and prevention of autoimmune disease. Proc Natl Acad Sci U S A *102*, 11272-11277.

Torborg, C.L., and Feller, M.B. (2004). Unbiased analysis of bulk axonal segregation patterns. J Neurosci Methods *135*, 17-26.

Triplett, J.W., and Feldheim, D.A. (2012). Eph and ephrin signaling in the formation of topographic maps. Semin Cell Dev Biol *23*, 7-15.

Tu, D.C., Zhang, D., Demas, J., Slutsky, E.B., Provencio, I., Holy, T.E., and Van Gelder, R.N. (2005). Physiologic diversity and development of intrinsically photosensitive retinal ganglion cells. Neuron *48*, 987-999.

Vallone, D., Lahiri, K., Dickmeis, T., and Foulkes, N.S. (2007). Start the clock! Circadian rhythms and development. Dev Dyn *236*, 142-155.

VanDunk, C., Hunter, L.A., and Gray, P.A. (2011). Development, maturation, and necessity of transcription factors in the mouse suprachiasmatic nucleus. J Neurosci *31*, 6457-6467.

Viney, T.J., Balint, K., Hillier, D., Siegert, S., Boldogkoi, Z., Enquist, L.W., Meister, M., Cepko, C.L., and Roska, B. (2007). Local retinal circuits of melanopsin-containing ganglion cells identified by transsynaptic viral tracing. Curr Biol *17*, 981-988.

Wang, L., Rangarajan, K.V., Lawhn-Heath, C.A., Sarnaik, R., Wang, B.S., Liu, X., and Cang, J. (2009). Direction-specific disruption of subcortical visual behavior and receptive fields in mice lacking the beta2 subunit of nicotinic acetylcholine receptor. J Neurosci *29*, 12909-12918.

Wässle, H. (2004). Parallel processing in the mammalian retina. Nat Rev Neurosci *5*, 747-757.

Wassle, H., Puller, C., Muller, F., and Haverkamp, S. (2009). Cone contacts, mosaics, and territories of bipolar cells in the mouse retina. J Neurosci *29*, 106-117.

Wee, R., Castrucci, A.M., Provencio, I., Gan, L., and Van Gelder, R.N. (2002). Loss of photic entrainment and altered free-running circadian rhythms in math5-/- mice. J Neurosci *22*, 10427-10433.

Wettschureck, N., Rutten, H., Zywietz, A., Gehring, D., Wilkie, T.M., Chen, J., Chien, K.R., and Offermanns, S. (2001). Absence of pressure overload induced myocardial hypertrophy after conditional inactivation of Galphaq/Galpha11 in cardiomyocytes. Nat Med *7*, 1236-1240.

White, F.A., Keller-Peck, C.R., Knudson, C.M., Korsmeyer, S.J., and Snider, W.D. (1998). Widespread elimination of naturally occurring neuronal death in Bax-deficient mice. J Neurosci *18*, 1428-1439.

Wilkie, T.M., Scherle, P.A., Strathmann, M.P., Slepak, V.Z., and Simon, M.I. (1991). Characterization of G-protein alpha subunits in the Gq class: expression in murine tissues and in stromal and hematopoietic cell lines. Proc Natl Acad Sci U S A *88*, 10049-10053.

Wong, R.O. (1999). Retinal waves and visual system development. Annu Rev Neurosci *22*, 29-47.

Wong, W.T., Sanes, J.R., and Wong, R.O. (1998). Developmentally regulated spontaneous activity in the embryonic chick retina. J Neurosci *18*, 8839-8852.

Xu, H.P., Furman, M., Mineur, Y.S., Chen, H., King, S.L., Zenisek, D., Zhou, Z.J., Butts, D.A., Tian, N., Picciotto, M.R.*, et al.* (2011). An instructive role for patterned spontaneous retinal activity in mouse visual map development. Neuron *70*, 1115-1127.

Xue, T., Do, M.T., Riccio, A., Jiang, Z., Hsieh, J., Wang, H.C., Merbs, S.L., Welsbie, D.S., Yoshioka, T., Weissgerber, P.*, et al.* (2011). Melanopsin signalling in mammalian iris and retina. Nature *479*, 67-73.

Yamazaki, S., Alones, V., and Menaker, M. (2002). Interaction of the retina with suprachiasmatic pacemakers in the control of circadian behavior. J Biol Rhythms *17*, 315-329.

Yang, Z., Ding, K., Pan, L., Deng, M., and Gan, L. (2003). Math5 determines the competence state of retinal ganglion cell progenitors. Dev Biol *264*, 240-254.

Young, M.J., and Lund, R.D. (1994). The anatomical substrates subserving the pupillary light reflex in rats: origin of the consensual pupillary response. Neuroscience *62*, 481-496.

Zaidi, F.H., Hull, J.T., Peirson, S.N., Wulff, K., Aeschbach, D., Gooley, J.J., Brainard, G.C., Gregory-Evans, K., Rizzo, J.F., 3rd, Czeisler, C.A.*, et al.* (2007). Short-wavelength light

sensitivity of circadian, pupillary, and visual awareness in humans lacking an outer retina. Curr Biol *17*, 2122-2128.

Zhang, D.Q., Belenky, M.A., Sollars, P.J., Pickard, G.E., and McMahon, D.G. (2012). Melanopsin mediates retrograde visual signaling in the retina. PLoS ONE *7*, e42647.

Zhang, D.Q., Wong, K.Y., Sollars, P.J., Berson, D.M., Pickard, G.E., and McMahon, D.G. (2008a). Intraretinal signaling by ganglion cell photoreceptors to dopaminergic amacrine neurons. Proc Natl Acad Sci U S A *105*, 14181-14186.

Zhang, J., Ackman, J.B., Xu, H.P., and Crair, M.C. (2011). Visual map development depends on the temporal pattern of binocular activity in mice. Nat Neurosci *15*, 298-307.

Zhang, J., Fuhrmann, S., and Vetter, M.L. (2008b). A nonautonomous role for retinal frizzled-5 in regulating hyaloid vitreous vasculature development. Invest Ophthalmol Vis Sci *49*, 5561-5567.

Kylie Shannon Chew

Born: Mammoth Lakes, CA. October 12th 1989

EDUCATION AND TRAINING:

THE JOHNS HOPKINS UNIVERSITY, Baltimore, MD
Doctoral research, August 2008- current
- Department of Biology: CMDB graduate program
- Thesis advisor: Dr. Samer Hattar
- Research focuses: neuroscience, genetics, behavioral neuroscience, developmental biology, circadian biology.

MARY BALDWIN COLLEGE, Staunton, VA
Bachelor of Science in Biology, May 2008
- Biology Thesis title: Mapping the Innexin Gap Junction Network in the Developing Nervous System of the Nematode *C. elegans*
- Honors Thesis title: *Artificium in Scientiam*: The Patterns of Elegance in Nature
- Minors in: Mathematics, Chemistry, and Philosophy
- Overall GPA: ~3.7/4.0

HONORS AND AWARDS:

2012:   J. Brien Key Travel Grant (JHU)
2011:   First prize in the Best Poster Competition at the Biology Department Annual Retreat (JHU)
2009:   Dupont Teaching Award (JHU)
2008 - 2011: George Owen Fellowship, given to competitive applicants for graduate school (JHU)
2008:   Graduated with Distinction in the Major, (MBC)
2008:   Honors Degree (MBC)
2008:   Member, Phi Beta Kappa
2008:   Biology Student of the Year (MBC)
2007 - 2008 Math-Science Leadership Scholarship, nominated by a faculty member (MBC)
2007 - 2008 Navas Family Scholarship for students with promise and seriousness of purpose in the sciences (MBC)
2007   Member, Iota Sigma Pi, National Honor Society for Women in Chemistry
2006   Member, Beta Beta Beta, National Biological Honor Society
2005 - 2008 Honors Scholar (MBC)

TEACHING EXPERIENCE:
2014:   Instructor for Introduction to Lab Research (JHU, Discover Hopkins)
2013:   Teaching Assistant for undergraduate course in Genetics (JHU)
2012:   Teaching Assistant for undergraduate course in Human Genetics (JHU)
2012, 2013, 2014 : Teaching Assistant for undergraduate course in Human Brain (JHU)
2012:   Tutor for graduate course in Developmental Biology (JHU)
2011:   Teaching Assistant for undergraduate course in Evolution (JHU)
2011:   Teaching Assistant for undergraduate course in Emerging Strategies and

Applications in Biomedical Research (JHU)
2010:	Teaching Assistant for undergraduate lab in Developmental Biology (JHU)
2009:	Teaching Assistant for undergraduate lab in Biochemistry (JHU)
2008:	Teaching Assistant for undergraduate lab in Cell Biology (MBC)
2007, 2008:	Teaching Assistant for undergraduate lab in Genetics (MBC)
2005, 2006:	Tutor for undergraduate course in Physics (MBC)
2005:	Teaching Assistant for undergraduate lab in General Chemistry (MBC)

PUBLICATIONS:

Chen S-K*, **Chew KS***, McNeill DS*, Keeley PW, Ecker JL, Mao BQ, Pahlberg J, Kim B, Lee SCS, Fox M, Guido W, Wong KY, Sampath AP, Reese BE, Kuruvilla R, Hattar S (2013) Apoptosis regulates ipRGC spacing necessary for rods and cones to drive circadian photoentrainment. *Neuron* 77:503-515.

Chew K.S., Schmidt T.M., Rupp A.C., Kofuji P., Trimarchi, J.M. Loss of Gq/11 genes does not abolish melanopsin phototransduction. PLoS ONE. 2014 May 28;9(5)

Chew KS*, Renna JM*, McNeill DS, Ecker J, Loevinsohn GS, Van Dunk C, Weng S, Gray P, Herzog E, Zhao H, Berson DM, Hattar S. (2014) M1 ipRGCs regulate the development of the circadian clock and vision. (Submitted to *Science*)

Schmidt TM, Rupp AC, **Chew KS**, Yungher B, Park KK, Hattar S. (2014) Ipsilateral pupil constriction requires ipRGCs. (Submitted to *Nature*)

ORAL PRESENTATIONS:
2013:	Chew KS, Renna JM, McNeill DS, Chen S-K, Zhao H, Berson DM, Hattar S. ipRGCs regulate the development of the circadian pacemaker and vision Association for Research in Vision and Ophthalmology Annual Meeting, Seattle, WA.
2012:	Chew KS, Renna JM, McNeill DS, Chen S-K, Zhao H, Berson DM, Hattar S. ipRGCs regulate the development of the circadian pacemaker and vision. Johns Hopkins Neuroscience Journal Club series
2011:	Chew KS, Renna JM, McNeill DS, Chen S-K, Zhao H, Berson DM, Hattar S. ipRGCs regulate the development of the circadian pacemaker and vision. Johns Hopkins Neuroscience Lab lunch series
2010:	Chew KS, McNeill DS, Ecker JL, Hattar S. Developmental loss of ipRGCs causes a lengthened free-running circadian period. Sleep and Circadian DataBlitz at the Society for Neuroscience 40th Annual Meeting, San Diego, CA

POSTERS:
2013:	Chew KS, Renna JM, Berson DM, Hattar S. M1 ipRGCs Regulate the Development of the Circadian Pacemaker and Vision. Cell Symposium: Genes, Circuits and Behavior, Toronto, Canada
2012:	Chew KS, Renna JM, McNeill DS, Berson DM, Hattar S. ipRGCs are critical for the proper development of the circadian clock. Society for Neuroscience 42st Annual Meeting, New Orleans, LA
2012:	Chew KS, Renna JM, McNeill DS, Chen S-K, Berson DM, Hattar S.

ipRGCs regulate the development of the circadian pacemaker and vision. FASEB meeting on Retinal Neurobiology & Visual Processing, Steamboat Springs, CO.

2011: Chew KS, McNeill DS, Ecker JL, Hattar S. Developmental loss of ipRGCs causes a lengthened free-running circadian period. Association for Research in Vision and Ophthalmology Annual Meeting, Ft. Lauderdale, FL.

2010: Chew KS, McNeill DS, Ecker JL, Hattar S. Developmental loss of ipRGCs causes a lengthened free-running circadian period. Society for Neuroscience 40th Annual Meeting, San Diego, CA

REFERENCES:

Samer Hattar (Thesis Advisor)
Associate Professor
Johns Hopkins University
Department of Biology
shattar@jhu.edu
(410) 516-4231

Haiqing Zhao
Professor
Johns Hopkins University
Department of Biology
hzhao@jhu.edu
(410) 516-7391

Chen-Ming Fan
Staff Member
Carnegie Institution for Science
Department of Embryology
fan@ciwemb.edu
(410) 246-3022